Nano-optical sensing and metrology through near- to far-field transduction

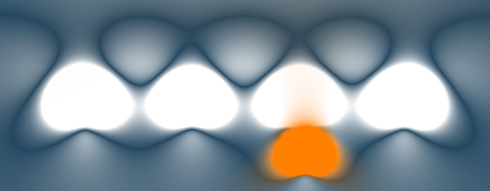

Robin D. Buijs

Nano-optical sensing and metrology through near- to far-field transduction

Robin Daniel Buijs

Cover image: a collection of scatterers transduce near-field information into the optical far field. Colours show interference between scattered fields and a driving plane wave, calculated using a discrete dipole model.

Ph. D. Thesis, Eindhoven University of Technology, July 2021
Nano-optical sensing and metrology through near- to far-field transduction
Robin Daniel Buijs
ISBN: 978-94-92323-55-2

The work described in this thesis was performed at:
AMOLF, Science Park 104, 1098 XG Amsterdam, The Netherlands.

This work is part of the research programme of the Netherlands Organisation for Scientific Research (NWO). It is part of the programme High Tech Systems and Materials (HTSM) with Project No. 14669, which is (partly) financed by NWO.

A digital version of this thesis is freely available at:
`https://ir.amolf.nl/` and `https://research.tue.nl/`.

NANO-OPTICAL SENSING AND METROLOGY THROUGH NEAR- TO FAR-FIELD TRANSDUCTION

PROEFSCHRIFT

ter verkrijging van de graad van doctor aan de
Technische Universiteit Eindhoven, op gezag van de
rector magnificus prof. dr. ir. F.P.T. Baaijens, voor een
commissie aangewezen door het College voor Promoties,
in het openbaar te verdedigen op dinsdag 6 juli 2021,
om 16:00 uur

door

Robin Daniel BUIJS

geboren te Nijmegen

Dit proefschrift is goedgekeurd door de promotoren en de samenstelling van de promotiecommissie is als volgt:

Voorzitter:	prof. dr. ir. G.M.W. Kroesen
1^{e} promotor:	prof. dr. E. Verhagen
2^{e} promotor:	prof. dr. G. Gerini
co-promotor:	prof. dr. A.F. Koenderink (Universiteit van Amsterdam)
leden:	dr. A. Sentenac (Institut Fresnel, Marseille)
	prof. dr. W.M.J.M. Coene (TU Delft)
	prof. dr. J. Gómez Rivas

Het onderzoek dat in dit proefschrift wordt beschreven is uitgevoerd in overeenstemming met de TU/e Gedragscode Wetenschapsbeoefening.

Nothing that is seen is seen all at once in its entirety.

Euclid, Optics, ca. 300 BCE

CONTENTS

1

INTRODUCTION

Optical magnification is one of the most intuitive methods of extending our senses beyond their biological limitations. Despite, or perhaps thanks to this intuitiveness, it has proven tremendously powerful. The development of compound telescopes in the early 17th century [1, 2] for the first time revealed satellites around other planets and provided the most direct evidence for the heliocentric model of the solar system to date [3], helping us place ourselves in the cosmos. The closely related microscope soon led to the revolutionary discovery of the cellular nature of life [4, 5] and direct evidence for germ theory [3, 6]. Ever since, optical measurements have played a central role in the advancement of science and technology.

For all its power, optical magnification has a prominent limitation. The wave nature of light means that light in free space cannot be focussed into a volume smaller than about one-half of its wavelength to a side. Conversely, even with ideal optics, imaging distorts the subject over length scales comparable with the wavelength of the light used. This set of closely related results is known as the diffraction limit: since visible light has a wavelength around 500 nm, traditional optical imaging cannot resolve details at nanometre scales.

Yet, whereas the early days of optical technology revealed the riches of the microscopic world, the nanoscopic world has even more to offer. Structures at the nanoscale explain the molecular mechanisms of life [7, 8] and open up the possibility of functional complex matter, with material properties tailored to specific uses [9–11]. In the modern world, analysis and characterisation of nanostructures is an urgent need in the life sciences [12–16] and semiconductor industry [17–19], both of which are increasingly focussed on objects at the nanoscale.

Diffraction has not stopped optics from progressing to nanoscopic scales. Various super-resolution techniques have been developed, enabling the study of (living) matter at the molecular level (see section 1.1.2 below). Moreover, not all optical measurement techniques are hampered by the diffraction limit in the way that imaging is. Interferometry, for instance, directly exploits the wave nature of light and has enabled some of the highest-resolution measurements to date (section 1.1.3). It is worth noting that not all nanoscale measurement and characterisation techniques depend on light. Scanning probe

techniques can provide high-resolution topographical and electronic information, as in scanning tunnelling microscopy [20, 21] and atomic force microscopy [22–24]. Electron microscopes can provide both of these functions as well as reveal crystal structures, for a myriad of applications [25–30]. Nonetheless, light is exceptional in many ways. Optical measurements tend to be non-destructive and minimally invasive (section 1.1.3). The electronic transitions of many materials, organic and inorganic, lie in the visible range, which means that optical spectroscopy can reveal a wealth of chemical information [31]. High-quality sources exist for many applications. High-power femtosecond laser systems are used to reveal and modify material properties. Widely available laser diodes are extremely bright and can have high spatial and temporal coherence. These properties make interferometry, spectroscopy and other optical measurement techniques fast and inexpensive. The high frequency of light waves, around 500 THz, combined with the wide transparency windows of many optical materials, permit transfer of optical signals at extremely high bandwidth [32]. Besides in its frequency spectrum, light also carries information in its polarisation state and spatial modes, both of which further enhance the effective bandwidth of optical signals. In a sensing context, each optical information channel can interact with samples differently and thus encode structural, chemical or electronic information. With the unlocking of the nanoscale and the many unique advantages of light, interest in optical sensing techniques is as strong as ever.

The journey of optical sensing to the nanoscale is not complete. Modern super-resolution techniques have several key weaknesses, from limited throughput to restrictions on types of samples, which we will discuss in this chapter. Yet, far-field signals may contain a tremendous amount of information across different frequency, wavevector and polarisation channels. Recently, inverse design approaches [33–35] have honed in on the challenge of nano-optical information retrieval in terms of information: how do we extract the maximum amount of information from a given set of signals? In this thesis, we explore the paradigm of **near- to far-field transduction** as an approach to nano-optical sensing. In this paradigm, we dynamically place known structures in the near-field of a sample in order to convert inaccessible near-field optical fields to readily measured far-field information. Over the course of this thesis, we investigate how nano-optical information may be extracted from such complex far-field channels, in doing so opening up a new path to super-resolution information retrieval.

In the following sections, we will briefly review how optical sensing at the nanoscale came to its current state, analysing the different approaches to super-resolution imaging as well as non-imaging optical sensing. We will elaborate on our paradigm of near- to far-field transduction and argue it may contribute to further advancement in nano-optical information retrieval and benefit science and technology.

1.1. A BRIEF HISTORY OF OPTICAL SENSING AT THE NANOSCALE

1.1.1. THE DIFFRACTION LIMIT

In the early days of optical technology, image quality was limited by lens defects. Glass-making improved by an evolutionary process of trial and error. In the late 19th century, the introduction of mathematical models to the craft brought the design of optical elements itself into the domain of science [36]. This soon led to the realisation that in conventional

microscopes, as in figure 1.1, diffraction precludes arbitrarily sharp focussing [37–39]. The original phrasing of the diffraction limit states that objects cannot be distinguished when separated by less than

$$D = \lambda / (2\,\mathrm{NA}) \tag{1.1}$$

with wavelength λ and numerical aperture $\mathrm{NA} = n \sin\theta$, in turn with n the refractive index of the surrounding medium and θ the opening half-angle of the collection path. This means that structures smaller than this length scale will not be imaged faithfully and cannot be reconstructed from the observed image without additional information. The diffraction limit as stated here is derived for a scalar field and does not account for the effects of the vectorial nature of light at high numerical apertures; we will elaborate on this in chapter 2. The equality in the diffraction limit (eqn. 1.1) can only be met with near-perfect optics. Each of the various lens aberrations will generally worsen the discrepancy between real and apparent feature size. Reducing these aberrations and optimising lens arrangements was the main source of improving microscope quality for the decades around the turn of the 20th century, as optical engineers tried to meet, but not surpass, the diffraction limit [40, 41].

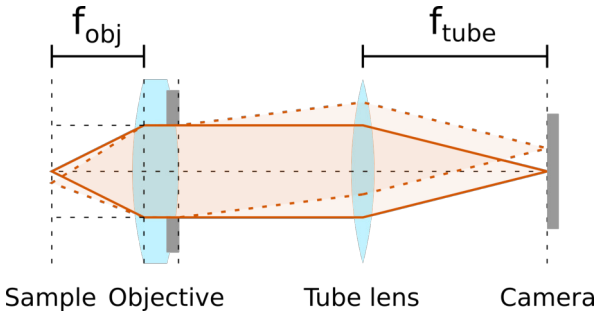

Figure 1.1: Imaging with a conventional microscope: the combination of objective and tube lens creates a magnified image, which may be recorded with a camera.

1.1.2. OPTICAL IMAGING BEYOND THE DIFFRACTION LIMIT

SUPER-RESOLUTION THROUGH NEAR-FIELD SENSING

The first feasible proposal to image beyond the diffraction limit was published in 1928, imagining a small aperture positioned within some 100 nm of a sample of interest [42, 43], which was theorised to allow highly localised sampling of the optical response of the sample. A variant on this proposal was first realised in 1984 [44], following advances in mechatronics [45] and an earlier implementation in the microwave regime [46]. The experimental platform used in the optical experiment came to be known as near-field scanning optical microscopy (NSOM) [47]. It operates by scanning a sharp probe, often a pulled fibre [48], in close proximity to a surface, typically within tens of nanometres [43, 45]; we will discuss the technical challenge of probe-sample distance control in section 2.4. NSOM is able to beat the diffraction limit by more than an order of magnitude, which it can do because the probe may interact with the near-field of the sample: that is, with

optical energy that does not propagate out to infinity. We will define the near-field more precisely in sections 2.2 and 2.3.

Depending on the NSOM configuration used, the probe may either be used as a highly localised light source [44], with photons reaching the sample only by tunnelling out from the sharp end of the probe, or to locally pick up transient or confined light [49]. Notable variants include apertureless or scattering-type NSOM (s-NSOM) (figure 1.2a), which uses a sharp probe not to illuminate or collect, but to locally scatter light into free space so that it may be detected normally [50–52]. Another technique based on the same distance control technology is the solid immersion lens. In this technique, a high-index material is placed in close proximity to a sample, such that evanescent field structures created in the high-index material are still felt by the sample [53]. Of course, solid immersion can only beat the diffraction limit by the refractive index of the solid. Techniques based on sharp near-field probes are powerful and flexible, able to attain resolution as good as 1 nm, [54] and compatible with polarisation [55, 56] and phase-resolved readout [57].

Near-field position control is technically challenging, but good solutions have been developed both for sharp probes (section 2.4) and more recently for planar structures [58]. A more fundamental limitation to the near-field techniques described is the necessity of physically scanning the probe over every point at which optical information is to be extracted. This, especially combined with the low signal levels achievable by photon tunnelling through a subwavelength optical fibre tip, makes NSOM measurements particularly slow. A number of proposals have been put forth to help speed up near-field measurements [59, 60], but the standard in NSOM technology remains a single probe scanning point by point.

SUPER-RESOLUTION THROUGH TAILORED ILLUMINATION

The diffraction limit is derived for the scenario of a point source of light propagated through circular apertures. Finer resolution can be achieved by exploiting the coherence of monochromatic light. This was likely first noted in the context of radar antenna arrays, which can be engineered to have arbitrarily narrow peaks in their radiation patterns at the expense of antenna gain [61]. This phenomenon came to be known as superoscillation [62], in which arbitrary spatial distributions of light can be created over finite domains, though at very low intensity: typically, superoscillatory peaks have intensity at least five orders of magnitude below nearby sidebands. Nonetheless, superoscillation can and has been used for extremely high-resolution optical sensing [63–66]. Less dramatic manipulations of incident wavefronts can already provide a significant improvement in resolution, especially when the polarisation degree of freedom is controlled as well [67]. Although the forward and reverse directions are described by the same wavevectors, measuring both can be beneficial. The 4π microscope in particular exploits interference between light collected through the forward and reverse paths to improve over the incoherent diffraction limit by a factor of four [68].

One class of techniques exploiting engineered illumination patterns are referred to as structured illumination microscopy (SIM) [69]. Such techniques exploit the moiré patterns that arise when a periodic illumination pattern is superimposed on the spatial frequencies of a sample structure. This moiré effect shifts high spatial frequency information into the observable region, allowing reconstruction of images with a resolution twice as high as would otherwise be possible [69–71]. Advanced implementations incorporate additional

known structures in the near-field of the sample (figure 1.2b), which permits a further improvement in resolution [72–74]. Without such structures, arbitrarily high spatial resolution may be attainable by combining SIM with non-linear photoresponse [75], though the practical constraints of measurements at a wide range of power levels may hinder implementation.

SUPER-RESOLUTION THROUGH DIRECT INVERSION

Although the diffraction limit prescribes that direct imaging will blur sample features, isolated point sources may still be localised: such sources will take on the shape of the point spread function of the microscope [76]. Given sufficient signal and knowledge of the imaging system, this function can be fitted to the image in order to retrieve the position of the sources. This is a simple example of inverse problem solving. For general distributions, inversion may be impossible: the problem is ill-posed [77] because the information that distinguishes different possible solutions is lost. Inversion may still be feasible under certain assumptions, like in the case of sparse point sources.

A series of techniques have been developed that allow the individual point sources that makes up complex fluorescent samples to be isolated, drastically simplifying the inverse problem. The oldest of these, stimulated emission depletion (STED) microscopy, achieves super-resolution by selectively suppressing fluorescence in a ring around a sub-diffractive region of interest through a carefully engineered de-excitation spot. The only fluorescent signal still captured then comes from the sub-diffractive central region [78]. Other fluorescence-based techniques, including photoactivated localisation microscopy (PALM) and stochastic optical reconstruction microscopy (STORM), exploit statistical analysis on the behaviour of dark states in fluorescent molecules to identify individual fluorophores [79, 80]. As such, they can make few-nanometre resolution images in three dimensions [81–83]. Fluorescence-based super-resolution imaging has had tremendous impact in the life sciences, where fluorophores can readily be incorporated into otherwise inscrutable biological structures [84, 85].

1.1.3. NON-IMAGING NANO-OPTICAL SENSING AND METROLOGY

Imaging is just one application of optical measurements. Of particular note for this thesis are the non-imaging optical sensing techniques classified as optical metrology, which includes precise measurements of (relative) length, distance, position and shape [86–89]. One highly successful technique for optical distance measurement is interferometry, which is widely used in (commercial) analysis and positioning systems [89–92] and in exceptional cases has been used to measure displacement with attometre resolution [93]. However, interferometers, like most of the tools in traditional metrology, are macroscopic devices [91]. Retrieving structural parameters of single nanostructures from measured signals, without super-resolution techniques, remains a challenging inverse problem.

Metrology is of particular importance in the semiconductor industry. As critical device features shrink to to just a few nanometres, so do process tolerances. Verifying whether processes and devices meet these stringent tolerances is largely up to optical metrology [94–96]. One core component of wafer metrology is overlay error: the misalignment between fabricated layers. Optical scatterometry is used commercially to retrieve overlay error with nanometre-scale precision by exploiting the modes of extended gratings [97–

99]. Another key component is critical dimension metrology, which verifies the actual fabricated dimensions of features, so that they may be compared to design values. In many applications, but critical dimension metrology in particular, optical methods compete [100] with techniques such as atomic force microscopy [101–105] and scanning electron microscopy [106, 107]. Between these, optical methods generally have the lowest resolution, but have the advantage of being fast and non-destructive. Optical metrology is generally model-based [100, 108], meaning that assumptions are made about (complex) refractive index and feature shape or size, other than the ones to be measured. This means that other sources of (traceable) information are needed to first calibrate the model. The advantage of the optical model comes in when, after this initial calibration, new measurements quickly, precise and non-destructively reveal differences with the calibration set.

Another part of wafer inspection concerns defect particle detection [109]. Various steps in wafer processing can generate or deposit particles, which are increasingly likely to disrupt device function as feature sizes shrink. Particle contaminants can be fatal to process yield and were one of the last barriers to commercialisation of EUV technology to be overcome [110]. Key to preventing particle contamination is the detection and classification of such particles, as this will provide clues to their origin. In some cases, classification may also permit salvaging of a suspect wafer by way of an appropriate cleaning step. Detection of small (20 nm or smaller), low-index particles can be done by destructive methods [111] or advanced scatterometry implementations [112, 113].

1.2. THE NEAR- TO FAR-FIELD TRANSDUCTION PARADIGM

Nano-optical sensing has transformed nanoscience. Nonetheless, the existing techniques each have their limitations: near-field scanning is a slow process and without near-field elements, techniques beat the diffraction limit only by a small factor or under specific assumptions. With the widespread interest in nanoscience, new techniques that may circumvent these limitations are being studied in various places. Some aim to perform imaging without near-field information by comparing far-field measurements with those for similar samples, solving the inverse problem, for instance, through machine learning [114, 115]. Of course, without near-field information, such approaches cannot uniquely determine nanoscale structure in general. Others aim to improve on NSOM by parallelisation, with each fibre channel or mode acting as a separate near-field probe [116–118]. This approach quickly runs into issues where spacing channels too closely leads to coupling between the channels and spacing them too far apart leads to impractically large probes. There is a possible intermediary between these approaches: to transduce near-field information from a wide range into the far-field, then take on the inverse problem of untangling the spatial structure of the near-field from the resulting complex patterns.

In this thesis, we explore the paradigm of near-field probes acting as near- to far-field transducers. We specifically embrace the coupling of near-field modes to different far-field modes, aiming to solve the inverse problem of retrieving near-field information from far-field channels by combining many such channels. In order to interact with nanoscale optical features directly, we consider introducing a known, two-dimensional nanostructure into the near-field of the sample. Such a structure, consisting of an engineered, finite pattern of sub-diffractive refractive index contrast in a plane, is known as a **metasurface patch**. Thanks to their sub-diffractive features, metasurfaces may provide modes with

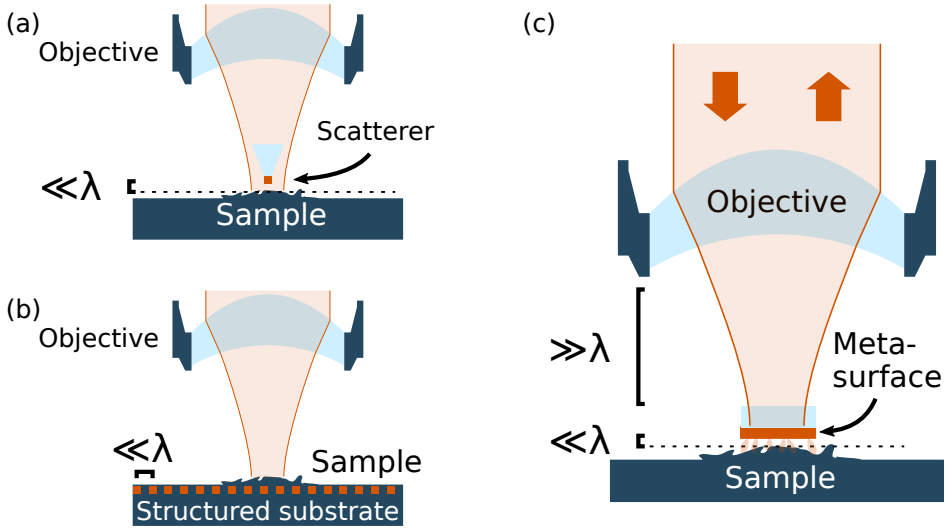

Figure 1.2: Three near-field assisted nano-optical sensing techniques. (a) Scattering-type near-field scanning optical microscopy. A scatterer is brought into the near field of a sample of interest. Interactions between the scatterer and (weakly) scattering features on the sample can be seen as a change in far-field signal. (b) Localised plasmonic structured illumination microscopy. A nanoparticle array, typically embedded in the structure, scatters high-frequency information out of the sample. (c) Optical sensing through near- to far-field transduction by a metasurface. The metasurface, which contains a range of spatial frequencies, scatters complex nano-optical information into the far field.

intricate spatial dependence of field profiles [119, 120]. We specifically aim to exploit the near-field enhancement seen around resonant plasmonic particles, where fields near metal-dielectric interfaces are strongly enhanced with respect to drive field intensity. Apart from the sharp spatial dependence resulting from such field profiles, field enhancement also makes plasmonic systems fine sensors, routinely achieving single-molecule sensitivity [121, 122]. They are particularly attractive for our purposes because of the high scattering cross-sections obtainable with plasmonic structures, including both particle and hole optical antennas. Metasurfaces composed of many such antennas will have a large number of optical modes. Since each mode may couple differently to different far-field channels, we now have a probe that transduces aspects of the near-field response of a sample into different degrees of freedom in its far-field scattering patterns.

Figure 1.2c sketches the envisioned technique: a metasurface patch is placed in the near-field of a sample. The ensemble is illuminated from afar. Multiple scattering between metasurface and sample then transduces information about nanoscale optical features of the sample into the far-field. The envisioned approach may be regarded as an advanced implementation of s-NSOM (figure 1.2a), where a probe is scanned across a sample in order to scatter light captured in its near-field out to a detector. However, the probes we envision are much more intricate ones. In that sense, our approach more resembles structured illumination, particularly the nanoparticle array-assisted variants (figure 1.2b): the probe is used to introduce engineered optical patterns into the sample near-field. In contrast

with this structured illumination technique, we intentionally introduce a wide range of spatial frequencies, such that sample information over this entire range may be scattered out. The main challenge then is solving the inverse problem, to reconstruct nanoscale optical features from far-field measurements.

Inverse problems are generally tough and ours is not an easy one. It immediately provokes a number of questions. Some relate to the fundamental possibility to extract near-field information from far-field measurements. Light that interacts with a complex transducer is drastically altered in its spatial character. Can we still deduce where the light originated from, when the light field is so perturbed? If so, does the transducer provide any benefit over direct imaging and deconvolution of a transfer function? Given the additional complexity introduced by multiple scattering, does that result extend to scattering objects? Can we use these insights to efficiently measure quantities of particular interest, like overlay error?

Other questions relate to the metasurface: what is a good transducer? We envision a transducer with a complicated mode structure that couples to a wide range of far-field modes. Different illumination conditions will lead to different near-field patterns. How flexibly may given transducers be used to generate specific near-field patterns? What resolutions in near-field patterns are achievable? Do near-field patterns engineered at some resolution allow us to sense at that same spatial resolution?

Finally, there are questions relating to information flow. The optical far field is a high-dimensional concept, with wavevectors, frequencies, polarisations and more. In our near- to far-field transduction scheme, near-field information ends up in all such degrees of freedom. It is an open question how many of, and which such degrees of freedom we need in order to retrieve any particular bit of information. Are some far-field channels more informative than others? How can we combine the information from complementary channels? Does selective read-out of particular channels lead to more efficient measurement and shorter integration times in real measurement problems?

The answers to all these questions determine how effective our proposed technique will be in different measurement contexts. We will address many such questions over the course of the following chapters.

1.3. OUTLINE OF THIS THESIS

Chapter 2 of this thesis introduces a number of theoretical and experimental methods that help us analyse and implement our near- to far-field transduction strategy. We will discuss evanescent fields, discrete dipole modelling, Fourier optics, and shear force probe-sample distance control.

In chapter 3, we address the question of whether light is transduced into the far field in a way that can be inverted to source position. We introduce a library-based method of nano-optical parameter retrieval from far-field images. Applying this method to experimental data collected using cathodoluminescence on a plasmonic structure, we retrieve the position of the induced point-like light source with a precision of $\lambda/200$.

In chapter 4, we investigate whether these results can be extended to localisation of scattering objects. We introduce a glass fibre tip into the near-field of plasmonic structures and retrieve its position from far-field data. We specifically explore how extended plasmonic structures assist in localisation.

In chapter 5, we ask whether a given transducer can be used to generate particular sets of near-field patterns. We investigate how manipulation of far-field illumination conditions can dynamically shape the near-field of metasurface patches. In calculations based on a discrete dipole model, we reproduce complete bases of exposure patterns on a rectangular grid and show that these patterns facilitate sensing of scattering objects.

In chapter 6, we study how our approach can help us measure overlay error between nanoscale objects. Exploiting moiré patterns to create a wide range of different overlay errors on a given sample, we show that overlay error is successfully retrieved, including based on calibration on separate targets.

In chapter 7, we examine how combining measurements of different far-field degrees of freedom can help in parameter retrieval. Measuring using different far-field illumination and analysis polarisations, we find more information when datasets are merged. We show that distributing a given photon budget over two polarisation channels can improve localisation performance and verify this experimentally.

REFERENCES

1. Van Helden, A. C. & van Gent, R. H. "The lens production by Christiaan and Constantijn Huygens". *Ann. Sci.* **56,** 69–79 (1999).
2. *The origins of the telescope* (eds Helden, A. V., Dupré, S., van Gent, R. & Zuidervaart, H.) (KNAW Press, 2010).
3. Drake, S. *Galileo at Work* (University of Chicago Press, Chicago, 1978).
4. Kircher, A. *Scrutinium Physico-Medicum Contagiosae Luis, Quae Pestis Dicitur* (Vitale Mascardi, Rome, 1658).
5. Gest, H. "The discovery of microorganisms by Robert Hooke and Antoni van Leeuwenhoek, Fellows of The Royal Society". *Notes Rec. R. Soc. London* **58,** 187–201 (2004).
6. Torrey, H. B. "Athanasius Kircher and the progress of medicine". *Osiris* **5,** 246–275 (1938).
7. Schrödinger, E. *What Is Life? The Physical Aspect of the Living Cell* (Cambridge University Press, Cambridge, 1944).
8. Nelson, P. *What Is Life? The Physical Aspect of the Living Cell* (W. H. Freeman, New York, 2003).
9. Drexler, K. E. *Engines of Creation: The Coming Era of Nanotechnology* (Doubleday, 1986).
10. Valdevit, L., Bertoldi, K., Guest, J. & Spadaccini, C. "Introduction". *J. Mater. Res.* **33,** 241–246 (2018).
11. Oliveri, G., Werner, D. H. & Massa, A. "Reconfigurable electromagnetics through metamaterials—A review". *Proc. IEEE* **103,** 1034–1056 (2015).
12. Nobel Institute. *The Nobel Prize in Medicine 2013* 2013.
13. Nobel Institute. *The Nobel Prize in Medicine 2017* 2017.
14. Nobel Institute. *The Nobel Prize in Chemistry 2020* 2020.

15. Tan, X., Letendre, J. H., Collins, J. J. & Wong, W. W. "Synthetic biology in the clinic: engineering vaccines, diagnostics, and therapeutics". *Cell* **184,** 881–898 (2021).
16. Kramps, T. & Elbers, K. in *RNA Vaccines* 1–11 (Springer New York, 2016).
17. *EUV Lithography* 2nd ed (ed Bakshi, V.) (ASQ Quality Press, 2018).
18. Pirati, A. *et al.* "Performance overview and outlook of EUV lithography systems". in *Extreme Ultraviolet (EUV) Lithography VI* (eds Wood, O. R. & Panning, E. M.) (SPIE, 2015).
19. Yeap, G. *et al.* "5nm CMOS Production Technology Platform featuring full-fledged EUV, and High Mobility Channel FinFETs with densest 0.021μm2 SRAM cells for Mobile SoC and High Performance Computing Applications". in *2019 IEEE International Electron Devices Meeting (IEDM)* (IEEE, 2019).
20. Binnig, G. & Rohrer, H. "Scanning tunneling microscopy". *Surf. Sci.* **126,** 236–244 (1983).
21. Nobel Institute. *The Nobel Prize in Physics 1986* 1986.
22. Binnig, G., Quate, C. F. & Gerber, C. "Atomic force microscope". *Phys. Rev. Lett.* **56,** 930–933 (1986).
23. Ohnesorge, F. & Binnig, G. "True atomic resolution by Atomic Force Microscopy through repulsive and attractive forces". *Science* **260,** 1451–1456 (1993).
24. Voigtländer, B. *Atomic Force Microscopy* (Springer International Publishing, 2019).
25. Ruska, E. *The early development of electron lenses and electron microscopy* (Hirzel Verlag, 1980).
26. *The Beginnings of Electron Microscopy* (ed Hawkes, P. W.) (Elsevier, 1985).
27. Avouris, P. & Demuth, J. "Electron energy loss spectroscopy in the study of surfaces". *Annu. Rev. Phys. Chem.* **35,** 49–73 (1984).
28. Carbone, F. "Modern electron microscopy resolved in space, energy and time". *Eur. Phys. J.: Appl. Phys.* **54,** 33503 (2011).
29. Gordon, R. E. in *Histopathology* 119–135 (Springer New York, 2014).
30. Lorusso, G. F., Horiguchi, N., Bömmels, J., Wilson, C. J., Van den Bosch, G., Kar, G. S., Ohashi, T., Sutani, T., Watanabe, R., Takemasa, Y. & Ikota, M. "Electron beam metrology for advanced technology nodes". *Jpn. J. Appl. Phys.* **58,** SD0801 (2019).
31. Skoog, D. A., Holler, F. J. & Crouch, S. R. *Principles of Instrumental Analysis 7th edition Skoog* 7th ed. (Cengage Learning, 2016).
32. Allan, W. B. *Fibre Optics: Theory and Practice* 1st ed. (Springer, Berlin, 1973).
33. Haeberlé, O., Belkebir, K., Giovaninni, H. & Sentenac, A. "Tomographic diffractive microscopy: basics, techniques and perspectives". *J. Mod. Opt.* **57,** 686–699 (2010).
34. Lin, Z., Roques-Carmes, C., Pestourie, R., Soljačić, M., Majumdar, A. & Johnson, S. G. "End-to-end nanophotonic inverse design for imaging and polarimetry". *Nanophotonics* **10,** 1177–1187 (2020).

35. Bouchet, D., Carminati, R. & Mosk, A. P. "Influence of the local scattering environment on the localization precision of single particles". *Phys. Rev. Lett.* **124,** 133903 (2020).
36. Rohr, M. V. *Ernst Abbe* (Gustav Fischer Verlag, 1940).
37. Abbe, E. "Beiträge zur Theorie des Mikroskops und der mikroskopischen Wahrnehmung". *Arch. Mikrosk. Anat.* **9,** 413–468 (1873).
38. Helmholtz & Fripp, H. "On the limits of the optical capacity of the microscope". *J. R. Microsc. Soc.* **16,** 15–39 (1876).
39. Strutt, J. W. "XXXI. Investigations in optics, with special reference to the spectroscope". *Philos. Mag.* **8,** 261–274 (1879).
40. Mappes, T., Jahr, N., Csaki, A., Vogler, N., Popp, J. & Fritzsche, W. "The invention of immersion ultramicroscopy in 1912 — the birth of nanotechnology?" *Angew. Chem., Int. Ed.* **51,** 11208–11212 (2012).
41. Douglas B. Murphy, M. W. D. *Fundamentals of Light Microscopy and Electronic Imaging* 2nd ed. (Wiley-Blackwell, 2012).
42. Synge, E. "XXXVIII.A suggested method for extending microscopic resolution into the ultra-microscopic region". *Philos. Mag.* **6,** 356–362 (1928).
43. Lereu, A., Passian, A. & Dumas, P. "Near field optical microscopy: a brief review". *Int. J. Nanotechnol.* **9,** 488 (2012).
44. Pohl, D. W., Denk, W. & Lanz, M. "Optical stethoscopy: Image recording with resolution $\lambda/20$". *Appl. Phys. Lett.* **44,** 651–653 (1984).
45. Betzig, E., Finn, P. L. & Weiner, J. S. "Combined shear force and near-field scanning optical microscopy". *Appl. Phys. Lett.* **60,** 2484–2486 (1992).
46. Ash, E. A. & Nicholls, G. "Super-resolution aperture scanning microscope". *Nature* **237,** 510–512 (1972).
47. Novotny, L. & Hecht, B. *Principles of Nano-Optics* (Cambridge University Press, 2006).
48. Betzig, E., Trautman, J. K., Harris, T. D., Weiner, J. S. & Kostelak, R. L. "Breaking the diffraction barrier: optical microscopy on a nanometric scale". *Science* **251,** 1468–1470 (1991).
49. Balistreri, M. L. M., Klunder, D. J. W., Blom, F. C., Driessen, A., Hoekstra, H. W. J. M., Korterik, J. P., Kuipers, L. & van Hulst, N. F. "Visualizing the whispering gallery modes in a cylindrical optical microcavity". *Opt. Lett.* **24,** 1829 (1999).
50. Wessel, J. "Surface-enhanced optical microscopy". *J. Opt. Soc. Am. B* **2,** 1538 (1985).
51. Zenhausern, F., O'Boyle, M. P. & Wickramasinghe, H. K. "Apertureless near-field optical microscope". *Appl. Phys. Lett.* **65,** 1623 (1994).
52. Bachelot, R., Gleyzes, P. & Boccara, A. C. "Near-field optical microscope based on local perturbation of a diffraction spot". *Opt. Lett.* **20,** 1924 (1995).
53. Mansfield, S. M. & Kino, G. S. "Solid immersion microscope". *Appl. Phys. Lett.* **57,** 2615–2616 (1990).

54. Zenhausern, F., Martin, Y. & Wickramasinghe, H. K. "Scanning interferometric apertureless microscopy: optical imaging at 10 angstrom resolution". *Science* **269,** 1083–1085 (1995).

55. Betzig, E., Trautman, J. K., Weiner, J. S., Harris, T. D. & Wolfe, R. "Polarization contrast in near-field scanning optical microscopy". *Appl. Opt.* **31,** 4563–4568 (1992).

56. McDaniel, E. B., McClain, S. C. & Hsu, J. W. P. "Nanometer scale polarimetry studies using a near-field scanning optical microscope". *Appl. Opt.* **37,** 84–92 (1998).

57. Balistreri, M. L. M., Korterik, J. P., Kuipers, L. & van Hulst, N. F. "Local observations of phase singularities in optical fields in waveguide structures". *Phys. Rev. Lett.* **85,** 294–297 (2000).

58. Ernst, S., Irber, D. M., Waeber, A. M., Braunbeck, G. & Reinhard, F. "A planar scanning probe microscope". *ACS Photonics* **6,** 327–331 (2019).

59. Wang, Y., Sun, C., Fang, N. & Zhang, X. "Towards High-Speed Near-Field Scanning Optical Microscope". in *Electronic and Photonic Packaging, Electrical Systems Design and Photonics, and Nanotechnology* (ASMEDC, 2004).

60. Seo, Y. & Jhe, W. "Fast-scanning near-field scanning optical microscopy using a high-frequency dithering probe". in *Controlling and Using Light in Nanometric Domains* (eds Lewis, A., Wickramasinghe, H. K. & Al-Shamery, K. H.) (SPIE, 2001).

61. Francia, G. T. D. "Super-gain antennas and optical resolving power". *Nuovo Cimento* **9,** 426–438 (1952).

62. Berry, M. "Faster than fourier". in *Quantum Coherence and Reality* (World Scientific, London, 1994), 55–65.

63. Huang, F. M. & Zheludev, N. I. "Super-resolution without evanescent waves". *Nano Lett.* **9,** 1249–1254 (2009).

64. Greenfield, E., Schley, R., Hurwitz, I., Nemirovsky, J., Makris, K. G. & Segev, M. "Experimental generation of arbitrarily shaped diffractionless superoscillatory optical beams". *Opt. Express* **21,** 13425 (2013).

65. Eliezer, Y. & Bahabad, A. "Super-Oscillating Airy pattern". *ACS Photonics* **3,** 1053–1059 (2016).

66. Rogers, K. S. & Rogers, E. T. F. "Realising superoscillations: A review of mathematical tools and their application". *JPhys Photonics* **2,** 042004 (2020).

67. Pereira, S. & van de Nes, A. "Superresolution by means of polarisation, phase and amplitude pupil masks". *Optics Commun.* **234,** 119–124 (2004).

68. Hell, S. & Stelzer, E. H. K. "Properties of a 4Pi confocal fluorescence microscope". *J. Opt. Soc. Am. A* **9,** 2159 (1992).

69. Gustafsson, M. G. L. "Surpassing the lateral resolution limit by a factor of two using structured illumination microscopy". *J. Microsc.* **198,** 82–87 (2000).

70. Mudry, E., Belkebir, K., Girard, J., Savatier, J., Moal, E. L., Nicoletti, C., Allain, M. & Sentenac, A. "Structured illumination microscopy using unknown speckle patterns". *Nat. Photonics* **6,** 312–315 (2012).

71. Heintzmann, R. & Huser, T. “Super-resolution structured illumination microscopy”. *Chem. Rev.* **117,** 13890–13908 (2017).
72. Liu, Z., Durant, S., Lee, H., Pikus, Y., Fang, N., Xiong, Y., Sun, C. & Zhang, X. “Far-Field optical superlens”. *Nano Lett.* **7,** 403–408 (2007).
73. Bezryadina, A., Zhao, J., Xia, Y., Zhang, X. & Liu, Z. “High spatiotemporal resolution imaging with localized plasmonic structured illumination microscopy”. *ACS Nano* **12,** 8248–8254 (2018).
74. Röhrich, R. & Koenderink, A. F. “Double moiré localized plasmon structured illumination microscopy”. *Nanophotonics* **10,** 1107–1121 (2020).
75. Heintzmann, R. & Gustafsson, M. G. L. “Subdiffraction resolution in continuous samples”. *Nat. Photonics* **3,** 362–364 (2009).
76. Born, M. & Wolf, E. *Principles of Optics* 7th (Cambridge University Press, 2019).
77. Hadamard, J. “Sur les problèmes aux dérivés partielles et leur signification physique”. *Princeton University Bulletin* **13,** 49–52 (1902).
78. Hell, S. W. & Wichmann, J. “Breaking the diffraction resolution limit by stimulated emission: stimulated-emission-depletion fluorescence microscopy”. *Opt. Lett.* **19,** 780 (1994).
79. Klar, T. A. & Hell, S. W. “Subdiffraction resolution in far-field fluorescence microscopy”. *Opt. Lett.* **24,** 954 (1999).
80. Betzig, E., Patterson, G. H., Sougrat, R., Lindwasser, O. W., Olenych, S., Bonifacino, J. S., Davidson, M. W., Lippincott-Schwartz, J. & Hess, H. F. “Imaging intracellular fluorescent proteins at nanometer resolution”. *Science* **313,** 1642–1645 (2006).
81. Huang, B., Wang, W., Bates, M. & Zhuang, X. “Three-dimensional super-resolution imaging by stochastic optical reconstruction microscopy”. *Science* **319,** 810–813 (2008).
82. Shtengel, G., Galbraith, J. A., Galbraith, C. G., Lippincott-Schwartz, J., Gillette, J. M., Manley, S., Sougrat, R., Waterman, C. M., Kanchanawong, P., Davidson, M. W., Fetter, R. D. & Hess, H. F. “Interferometric fluorescent super-resolution microscopy resolves 3D cellular ultrastructure”. *Proc. Natl. Acad. Sci.* **106,** 3125–3130 (2009).
83. Thorley, J. A., Pike, J. & Rappoport, J. Z. in *Fluorescence Microscopy* 199–212 (Elsevier, 2014).
84. “Method of the Year 2008”. *Nat. Methods* **6,** 1–1 (2008).
85. Nobel Institute. *The Nobel Prize in Chemistry 2014* 2014.
86. Bucher, J. L. *The Metrology Handbook* 2nd ed (SPIE Press, 2012).
87. Leach, R. *Optical Measurement of Surface Topography* (Springer-Verlag, 2011).
88. Harding, K. *Handbook of Optical Dimensional Metrology* (Taylor & Francis Group, 2013).
89. Berkovic, G. & Shafir, E. “Optical methods for distance and displacement measurements”. *Adv. Opt. Photonics* **4,** 441 (2012).

90. Freischlad, K., Tang, S. & Grenfell, J. "Interferometry for wafer dimensional metrology". in *Advanced Characterization Techniques for Optics, Semiconductors, and Nanotechnologies III* (eds Duparré, A., Singh, B. & Gu, Z.-H.) (SPIE, 2007).

91. Watchi, J., Cooper, S., Ding, B., Mow-Lowry, C. M. & Collette, C. "Contributed Review: A review of compact interferometers". *Rev. Sci. Instrum.* **89,** 121501 (2018).

92. Yang, S. & Zhang, G. "A review of interferometry for geometric measurement". *Meas. Sci. Technol.* **29,** 102001 (2018).

93. Et al., B. A. "Observation of gravitational waves from a binary black hole merger". *Phys. Rev. Lett.* **116** (2016).

94. Felix, N. M., Gabor, A. H., Menon, V. C., Longo, P. P., Halle, S. D., Koay, C.-s. & Colburn, M. E. "Overlay improvement roadmap: strategies for scanner control and product disposition for 5-nm overlay". in *Metrology, Inspection, and Process Control for Microlithography XXV* (ed Raymond, C. J.) (SPIE, 2011).

95. Bunday, B. D., Bello, A., Solecky, E. & Vaid, A. "7/5nm logic manufacturing capabilities and requirements of metrology". in *Metrology, Inspection, and Process Control for Microlithography XXXII* (eds Adan, O. & Ukraintsev, V. A.) (SPIE, 2018).

96. Orji, N. G., Badaroglu, M., Barnes, B. M., Beitia, C., Bunday, B. D., Celano, U., Kline, R. J., Neisser, M., Obeng, Y. & Vladar, A. E. "Metrology for the next generation of semiconductor devices". *Nat. Electron.* **1,** 532–547 (2018).

97. Bringoltz, B. *et al.* "Accuracy in optical overlay metrology". in *Metrology, Inspection, and Process Control for Microlithography XXX* (eds Sanchez, M. I. & Ukraintsev, V. A.) (SPIE, 2016).

98. Adel, M., Ghinovker, M., Golovanevsky, B., Izikson, P., Kassel, E., Yaffe, D., Bruckstein, A., Goldenberg, R., Rubner, Y. & Rudzsky, M. "Optimized overlay metrology marks: theory and experiment". *IEEE Trans. Semicond. Manuf.* **17,** 166–179 (2004).

99. Röhrich, R., Oliveri, G., Kovaios, S., Tenner, V. T., den Boef, A. J., Overvelde, J. T. B. & Koenderink, A. F. "Uncertainty estimation and design optimization of 2D diffraction-based overlay metrology targets". *ACS Photonics* **7,** 2765–2777 (2020).

100. Bunday, B., Germer, T. A., Vartanian, V., Cordes, A., Cepler, A. & Settens, C. "Gaps analysis for CD metrology beyond the 22nm node". in *Metrology, Inspection, and Process Control for Microlithography XXVII* (eds Starikov, A. & Cain, J. P.) (SPIE, 2013).

101. Griffith, J. E. & Grigg, D. A. "Dimensional metrology with scanning probe microscopes". *J. Appl. Phys.* **74,** R83–R109 (1993).

102. Liu, H.-C., Osborne, J. R., Osborn, M. & Dahlen, G. A. "Advanced CD-AFM probe tip shape characterization for metrology accuracy and throughput". in *Metrology, Inspection, and Process Control for Microlithography XXI* (ed Archie, C. N.) (SPIE, 2007).

103. Orji, N. G., Dixson, R. G., Bunday, B. D. & Allgair, J. A. "Toward accurate feature shape metrology". in *Metrology, Inspection, and Process Control for Microlithography XXII* (eds Allgair, J. A. & Raymond, C. J.) (SPIE, 2008).

104. Dixson, R. “Traceable calibration of a critical dimension atomic force microscope”. *J. Micro/Nanolithogr., MEMS, MOEMS* **11,** 011006 (2012).

105. Hussain, D., Ahmad, K., Song, J. & Xie, H. “Advances in the atomic force microscopy for critical dimension metrology”. *Meas. Sci. Technol.* **28,** 012001 (2016).

106. Vladár, A. E., Villarrubia, J. S., Chawla, J., Ming, B., Kline, J. R., List, S. & Postek, M. T. “10nm three-dimensional CD-SEM metrology”. in *Metrology, Inspection, and Process Control for Microlithography XXVIII* (eds Cain, J. P. & Sanchez, M. I.) (SPIE, 2014).

107. Levi, S., Schwarzban, I., Karvtsov, A., Tobayas, M., Stock, H.-J., Muelders, T., Hand, S. & Osborne, J. “3D optical proximity model optimization using inline 3DSEM metrology”. in *Metrology, Inspection, and Process Control for Microlithography XXXIII* (eds Adan, O. & Ukraintsev, V. A.) (SPIE, 2019).

108. Kumar, N., Petrik, P., Ramanandan, G. K. P., Gawhary, O. E., Roy, S., Pereira, S. F., Coene, W. M. J. & Urbach, H. P. “Reconstruction of sub-wavelength features and nano-positioning of gratings using coherent Fourier scatterometry”. *Opt. Express* **22,** 24678 (2014).

109. Florescu, D., Rodier, D. R. & Knollenberg, B. A. in *Handbook of Silicon Wafer Cleaning Technology* 659–699 (Elsevier, 2018).

110. Yun, H., Goodwin, F., Huh, S., Orvek, K., Cha, B., Rastegar, A. & Kearney, P. “SEMATECH EUVL mask program status”. in *Photomask and Next-Generation Lithography Mask Technology XVI* (ed Hosono, K.) (SPIE, 2009).

111. Jindal, V., John, A., Harris-Jones, J., Kearney, P., Antohe, A., Stinzianni, E., Goodwin, F. & Onoue, T. “Inspection and compositional analysis of sub-20 nm EUV mask blank defects by thin film decoration technique”. in *Extreme Ultraviolet (EUV) Lithography IV* (ed Naulleau, P. P.) (SPIE, 2013).

112. Van der Walle, P., Kramer, E., van der Donck, J. C. J., Mulckhuyse, W., Nijsten, L., Arango, F. A. B., de Jong, A., van Zeijl, E., Spruit, H. E. T., van den Berg, J. H., Nanda, G., van Langen-Suurling, A. K., Alkemade, P. F. A., Pereira, S. F. & Maas, D. J. “Deep sub-wavelength metrology for advanced defect classification”. in *Optical Measurement Systems for Industrial Inspection X* (eds Lehmann, P., Osten, W. & Gonçalves, A. A.) (SPIE, 2017).

113. Cheon, S., Lee, H., Kim, C. O. & Lee, S. H. “Convolutional neural network for wafer surface defect classification and the detection of unknown defect class”. *IEEE Trans. Semicond. Manuf.* **32,** 163–170 (2019).

114. Pu, T., Ou, J. Y., Papasimakis, N. & Zheludev, N. I. “Label-free deeply subwavelength optical microscopy”. *Appl. Phys. Lett.* **116,** 131105 (2020).

115. Ghosh, A., Roth, D. J., Nicholls, L. H., Wardley, W. P., Zayats, A. & Podolskiy, V. A. “Machine learning-based diffractive imaging with subwavelength resolution”. in *Conference on Lasers and Electro-Optics* (OSA, 2020).

116. Grosjean, T., Ibrahim, I. A. & Mivelle, M. “Multichannel probes for polarization-resolved scanning near-field optical microscopy”. *Appl. Opt.* **49,** 2617 (2010).

117. Wen, X., Datta, A., Traverso, L. M., Pan, L., Xu, X. & Moon, E. E. “High throughput optical lithography by scanning a massive array of bowtie aperture antennas at near-field”. *Sci. Rep.* **5** (2015).

118. Amitonova, L. V. & de Boer, J. F. “Endo-microscopy beyond the Abbe and Nyquist limits”. *Light Sci. Appl.* **9,** 81 (2020).

119. Gwo, S., Wang, C.-Y., Chen, H.-Y., Lin, M.-H., Sun, L., Li, X., Chen, W.-L., Chang, Y.-M. & Ahn, H. “Plasmonic metasurfaces for nonlinear optics and quantitative SERS”. *ACS Photonics* **3,** 1371–1384 (2016).

120. Gangaraj, S. A. H. & Monticone, F. “Molding light with metasurfaces: from far-field to near-field interactions”. *Nanophotonics* **7,** 1025–1040 (2018).

121. Taylor, A. B. & Zijlstra, P. “Single-molecule plasmon sensing: current status and future prospects”. *ACS Sensors* **2,** 1103–1122 (2017).

122. Mejía-Salazar, J. R. & Oliveira, O. N. “Plasmonic biosensing”. *Chemical Reviews* **118,** 10617–10625 (2018).

2

METHODS

This chapter will introduce a number of theoretical and experimental techniques that will prove valuable in the study of near- to far-field transduction. First, we discuss how light may be described in reciprocal space and deduce the nanoscopic origin of the diffraction limit. Then, we discuss scattering of light by discrete point dipoles. After this, we explore some insights the description of light in wavevector space provides for imaging. Finally, we discuss shear force feedback for near-field position control.

2.1. EVANESCENT FIELDS AND THE DIFFRACTION LIMIT

Many problems in science and engineering are more readily solved in reciprocal time or space [1, 2]. The propagation of light is an excellent example. Maxwell's equations describe the electric and magnetic field each as three-dimensional vector fields **E** and **H** that together obey certain laws in time and space [3]. We are free to use Fourier transforms [4] to convert between real space and reciprocal space for any of the dimensions:

$$\mathbf{E}(\mathbf{r}, t) = \mathbf{E}(x, y, z, t) \quad \leftrightarrow \quad \mathbf{E}(k_x, k_y, z, t) \tag{2.1}$$

and similarly for the magnetic field. Importantly, spatial frequencies in electromagnetic fields in vacuum have a special interpretation as solutions to the wave equation [5]:

$$\left(\frac{1}{\varepsilon_0 \mu_0}\nabla^2 + \frac{\delta^2}{\delta t^2}\right)\mathbf{E} = 0 \tag{2.2}$$

where ε_0 and μ_0 are the permittivity and permeability of vacuum. We will treat the problem in vacuum for brevity, though it is easily extended to homogeneous media. The wave equation, of course, permits solutions of the form $\mathbf{E}(\mathbf{r}, t) = \mathbf{E}_0\, e^{i(\omega t - \mathbf{k}\cdot\mathbf{r})}$, where (temporal) frequency ω and wavevector $\mathbf{k} = (k_x, k_y, k_z)$ are related by $|\mathbf{k}| = \sqrt{k_x^2 + k_y^2 + k_z^2} = \omega / c_0$ with $c_0 = 1/\sqrt{\varepsilon_0 \mu_0}$. Such a wave will travel at the speed of light along $\mathbf{k}$. An example of this connection is shown in figure 2.1a. This insight is known as the angular spectrum representation of electromagnetic fields [6], which maps the electric field distribution in equation 2.1 to a set of plane waves along $\mathbf{k} = (k_x, k_y, k_z)$ with $k_z = \sqrt{|\mathbf{k}|^2 - k_x^2 - k_y^2}$. The latter equation presents an interesting edge case: when $k_\parallel = \sqrt{k_x^2 + k_y^2} > |\mathbf{k}|$, k_z becomes imaginary. This wavevector still corresponds to a solution to the wave equation, but the intensity of that solution falls off exponentially in z. Such a solution is referred to as an **evanescent wave**. An example evanescent field profile is shown in figure 2.1b. The exponential drop-off means that particularly high spatial frequencies do not generally propagate out to infinity away from the $z = 0$ plane. The largest spatial frequency that will propagate corresponds to $k_\parallel = |\mathbf{k}|$, a plane wave propagating along the plane of the decomposition. A wave with $k_\parallel = \sqrt{2}|\mathbf{k}|$, on the contrary, will decay along z over a length scale of $2\pi/|\mathbf{k}| = \lambda$, where λ is the wavelength of the light used. For large spatial frequencies $k_\parallel$, the spatial extent of the exponential tail becomes approximately equal to the in-plane wavelength itself: $\lambda_\parallel = 2\pi/k_\parallel$. One definition of the **optical near field** is as the region where evanescent fields have appreciable strength. Of course, as the length scale of decay depends on spatial frequency, this does not produce a unique length scale. What it does tell us is that in order to directly sense fields structured at some small fraction of a wavelength, evanescent fields dictate that we need to probe at a comparable distance from the source.

The relation between spatial frequency and propagation also implies the existence of some sort of diffraction limit. Practically only propagating waves can be collected in the far field (as opposed to the near field, by the definition in this section). These waves correspond to spatial frequencies up to the inverse of the wavelength of the light used. If we model a point source as a delta peak in electric field in one point in a plane, its Fourier transform has infinite extent. The far field corresponds to all propagating light, so all $k_\parallel \leq |\mathbf{k}|$. In terms of numerical aperture, we consider all waves propagating in the forward

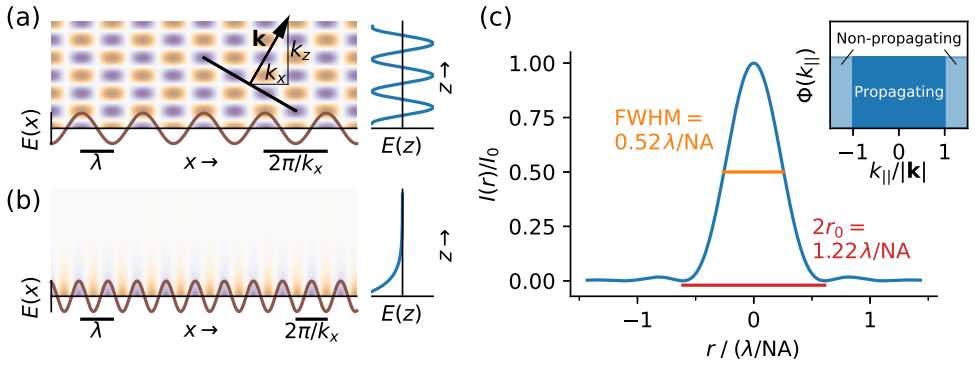

Figure 2.1: (a) A spatially modulated field oscillates and couples to propagating waves. The field shown here has $|k_x| = |\mathbf{k}|/2$. (b) A spatially modulated field oscillates, but couples only to evanescent waves. The field shown here has $|k_x| = 1.05\,|\mathbf{k}|$ and so falls off exponentially in z. (c) The Airy disc, the pattern produced by imaging a small isotropic source with only those wavevectors $k_\parallel \leq k_{\max}$. The inset shows the corresponding picture in wavevector space, identifying the propagating and non-propagating regimes in a far-field flux versus wavevector graph.

direction, so that the maximum angle from the normal $\theta_{\max} = \pi/2$ and numerical aperture $\mathrm{NA} = n \sin\theta_{\max} = n$. High-fidelity imaging can be modelled as considering exclusively that part of the Fourier transform where $k_\parallel \leq |\mathbf{k}|$ and transforming back. This process turns a point source into a broadened peak known as the Airy disc [7, 8]. This intensity peak, sketched in figure 2.1c, has a width at half-maximum of FWHM $\approx 0.52\lambda/\mathrm{NA}$ when all propagating waves are included. Around its central maximum lie alternating dark and bright rings of decreasing amplitude. The width of the first such dark ring $2r_0 \approx 1.22\lambda/\mathrm{NA}$ is often quoted as the diffraction limit, the resolution limit in optical imaging [8]. The same theory applies on both sides of an imaging set-up: a far-field image in free space cannot make use of frequencies greater than the wavevector of the light used.

Our analysis here is simplified in a number of ways. For one, the description of a point source of light as a delta peak in electric field disregards the vectorial nature of light. The electric field, magnetic field and wavevector of a propagating wave all have to be orthogonal. For this reason, a point source of light has to radiate across a range of polarisation channels. Polarisation may break the point symmetry of the problem and lead to a spot elongated along the dominant polarisation axis [6]. We also did not account for the distinction between spatial frequency content and feature size. The field of superoscillation shows that it is very well possible to create arbitrarily fine patterns with finite spatial frequency content, albeit at the expense of intensity [9, 10]. Another major simplification is that we consider only fields in a vacuum. Homogeneous media show the same behaviour, although at smaller scale, as the wavelength of light in the medium is reduced by a factor of refractive index $n = \sqrt{\varepsilon\mu}$. Structured media, in contrast, may strongly alter the patterns of electromagnetic fields. One way in which structured media alter field patterns is that an object with different refractive index than its environment will create an electromagnetic field feature, a region where field deviates from the background value, of similar size as the object, even with unstructured illumination. This field feature may involve both light scattered into the far-field and light captured in evanescent waves.

Small metallic particles, for instance, may have a plasmonic resonance. When driven on resonance, such particles will have both a strong near-field response, with a sharp position dependence of field strength in the region surrounding the particle, and also scatter light into far-field propagating waves [11, 12]. This phenomenon is exploited in both scattering-type near-field scanning optical microscopy [13, 14] and plasmon-assisted structured illumination microscopy [15, 16]. It is also how we interact with near fields in this thesis: by placing objects within the near field of a target of interest to transduce evanescent waves to propagating ones, or vice versa.

2.2. DISCRETE DIPOLE ANALYSIS

Electromagnetic waves interacting with matter cause charges to move. These moving charges have their own fields and so cause scattering of light. Such induced charge distributions may be expressed in terms of their multipole moments. A useful mathematical abstraction is the point dipole: an electric or magnetic point particle found as the limit of bringing two opposite charges arbitrarily close together while keeping dipole moment fixed [5]. Since a pair of dipoles has a quadrupole moment and more complex configurations of dipoles have higher multipoles, any net-zero charge distribution can be represented by a suitable (possibly infinite) collection of point dipoles. This approach is referred to as discrete dipole modelling and can be used to calculate both field structures and far-field radiation patterns [17, 18]. Moreover, it turns out that certain systems of small particles are modelled faithfully with a small number of such point dipoles [19]. Electromagnetic fields in finely structured matter are often modelled by numerical methods, such as finite element and finite-difference time domain methods [20, 21]. Compared with these, the discrete dipole model is a very fast way to get a qualitative sense of the behaviour of systems of interacting particles. It is a particularly good match for plasmonic particles, which thanks to their small sizes and strong interactions can often be modelled as single dipoles.

In our discrete dipole model, we consider particles i polarisable by a driving electric field at their position $\mathbf{E}_i$, through

$$\mathbf{p}_i = \overleftrightarrow{\boldsymbol{\alpha}}_i \mathbf{E}_i \tag{2.3}$$

with polarisability tensor $\overleftrightarrow{\boldsymbol{\alpha}}$. We can generally calculate the incident field strength, but the scattering system itself may add additional terms. The field of a single electric dipole at position $\mathbf{r}'$ may be expressed in terms of its (tensorial) Green's function $\overleftrightarrow{\mathbf{G}}(\mathbf{r},\mathbf{r}')$ as $\mathbf{E}(\mathbf{r}) = \mu_0\mu\,\omega^2\,\overleftrightarrow{\mathbf{G}}(\mathbf{r},\mathbf{r}')\,\mathbf{p}$. This Green's function may be found by modelling the dipole as a point-like current distribution and reads [6]

$$\overleftrightarrow{\mathbf{G}}(\mathbf{r},\mathbf{r}') = \frac{\mathrm{e}^{\pm \mathrm{i}k\Delta r}}{4\pi\Delta r}\left[\frac{k^2\Delta r^2 + \mathrm{i}k\Delta r - 1}{k^2\Delta r^2}\overleftrightarrow{\mathbf{I}} + \frac{3 - 3\mathrm{i}k\Delta r - k^2\Delta r^2}{k^2\Delta r^2}\frac{\Delta\mathbf{r}\Delta\mathbf{r}}{\Delta r^2}\right] \tag{2.4}$$

$$= \frac{\mathrm{e}^{\pm \mathrm{i}k\Delta r}}{4\pi\Delta r}\left(\underbrace{\frac{1}{k^2\Delta r^2}\left[-\overleftrightarrow{\mathbf{I}} + 3\frac{\Delta\mathbf{r}\Delta\mathbf{r}}{\Delta r^2}\right]}_{\text{Near-field}} + \underbrace{\frac{1}{k\Delta r}\left[\mathrm{i}\overleftrightarrow{\mathbf{I}} - 3\mathrm{i}\frac{\Delta\mathbf{r}\Delta\mathbf{r}}{\Delta r^2}\right]}_{\text{Intermediate field}} + \underbrace{\left[\overleftrightarrow{\mathbf{I}} - 3\frac{\Delta\mathbf{r}\Delta\mathbf{r}}{\Delta r^2}\right]}_{\text{Far-field}}\right), \tag{2.5}$$

where we make use of the unit tensor $\overleftrightarrow{\mathbf{I}}$, $k = \sqrt{\mu_0\mu\varepsilon_0\varepsilon}\,\omega$ is the spatial frequency of the driving field, $\delta\mathbf{r} = \mathbf{r}' - \mathbf{r}$ and $\delta r = |\delta\mathbf{r}|$. In the last line we have grouped terms by order in

Δr. As energy flux scales with the product of **E** and **H**, both of which scale with $\overleftrightarrow{\mathbf{G}}(\mathbf{r},\mathbf{r}')$, the rightmost term, which is of order $1/\Delta r$, is both the lowest term that contributes to net energy transport away from the dipole and the highest permitted by energy conservation. We refer to this term as the far-field term. It corresponds to the famous donut-shaped radiation pattern of a dipole antenna, with no energy radiated along the dipole axis. The other two terms fall off more quickly with distance from the dipole and are termed the near- ($1/\Delta r^3$) and intermediate-field ($1/\Delta r^2$) terms. The near-field term provides a complimentary definition of the near field to the one from section 2.1: the near field region is that region where the near-field term dominates scattering problems. We enter this regime when $k\Delta r \ll 1$, so, the near field by this definition extends for a fraction of a wavelength.

Over the rest of this section, we will discuss what the discrete dipole model can tell us about scattering by individual particles. We will then discuss how systems of scattering particles may be solved in a discrete dipole model.

2.2.1. HARMONIC OSCILLATOR MODEL OF A DIPOLE SCATTERER

We will model a dipole scatterer as a small spherical particle of radius r_{ant}. For such a particle, we can derive [22] a static polarisability of

$$\overleftrightarrow{\boldsymbol{\alpha}} = 4\pi\varepsilon_0\varepsilon_{\text{m}}\, r_{\text{ant}}^3 \frac{\varepsilon-\varepsilon_{\text{m}}}{\varepsilon+2\varepsilon_{\text{m}}} \overleftrightarrow{\mathbf{I}} \tag{2.6}$$

with a particle permittivity ε in a medium of permittivity ε_{m}. In case of highly conductive materials, such as the popular plasmonic materials of gold and aluminium, we can use a (modified) Drude model to describe the frequency dependence of this permittivity. For a free electron gas as a function of frequency, permittivity $\varepsilon = 1+\chi$ relates polarisation and electric field as $P = \varepsilon_0\chi E$. We consider the one-dimensional equation of motion for a moving electron with kinetic energy loss rate γ_0. The uniform γ_0 approximation makes this a Drude model. Subject to a Lorentz force $F = -eE$, this electron will move as

$$\ddot{r} = -\gamma_0\dot{r} - \frac{e}{m_{\text{e}}}E(t). \tag{2.7}$$

We can solve this equation in frequency space:

$$-\omega^2 r = \mathrm{i}\gamma_0\omega r - \frac{e}{m_{\text{e}}}E(\omega) \qquad \longrightarrow \qquad r(\omega) = \frac{e}{m_{\text{e}}}\frac{1}{\omega(\omega+\mathrm{i}\gamma_0)}E(\omega). \tag{2.8}$$

In a material, the charge of the electrons is balanced by the positively charged lattice ions. Displacement of the electron gas will thus polarise the material. For the polarisation density of the free electron gas we may write [23]

$$P(\omega) = n_{\text{e}}p(\omega) = -n_{\text{e}}e\,r(\omega) = -\frac{n_{\text{e}}e^2}{m_{\text{e}}}\frac{1}{\omega(\omega+\mathrm{i}\gamma_0)}E(\omega) \equiv \varepsilon_0\chi E(\omega). \tag{2.9}$$

We now define plasma frequency $\omega_{\text{p}} = \sqrt{n_{\text{e}}e^2/(m_{\text{e}}\varepsilon_0)}$ and conclude

$$\varepsilon(\omega) \equiv 1+\chi(\omega) = 1 - \frac{\omega_{\text{p}}^2}{\omega(\omega+\mathrm{i}\gamma_0)}. \tag{2.10}$$

With $\varepsilon_\mathrm{m} \approx 1$, equations 2.10 and 2.6 combine to

$$\overleftrightarrow{\boldsymbol{\alpha}} = 4\pi\varepsilon_0\varepsilon\, r_\mathrm{ant}^3 \frac{\omega_0^2}{\omega_0^2 - \omega^2 - \mathrm{i}\gamma_0\omega} \overleftrightarrow{\mathbf{I}} \qquad \text{where} \qquad \omega_0 \equiv \sqrt{\tfrac{1}{3}}\,\omega_\mathrm{p}. \tag{2.11}$$

Rewriting this equation and transforming it to the time domain gives us the equation of motion for a damped harmonic oscillator

$$\frac{\mathrm{d}^2}{\mathrm{d}t^2}\mathbf{p} + \gamma_0 \frac{\mathrm{d}}{\mathrm{d}t}\mathbf{p} + \omega_0^2\mathbf{p} = \beta\mathbf{E} \tag{2.12}$$

where we use oscillator strength $\beta = 4\pi\varepsilon_0\varepsilon r_\mathrm{ant}^3\omega_0^2$. Such a harmonic oscillator will have a natural frequency of $\omega_\mathrm{n} = \omega_0\sqrt{1-(\gamma_0/2)^2/\omega_0^2}$ and a quality factor of $Q = \omega_0/\gamma_0$. In this case, the oscillator may be driven not only by external fields, but will also cause an electric field to act on itself. This is known as the self-action of the scatterer and corresponds to its Green's function at vanishing separation [6]

$$G_\mathrm{self} = \lim_{\mathbf{r}\to 0} \frac{1}{4\pi}\left[\frac{2}{3}\mathrm{i}k + \frac{1+\cos^2\theta}{2r} + \frac{3\cos^2\theta - 1}{k^2 r^3}\right]. \tag{2.13}$$

In order to incorporate this effect, we rewrite the perceived electric field as the sum of an external drive and a self-action term $\mathbf{E} = \mathbf{E}_\mathrm{dr} + \mathbf{E}_\mathrm{self}$. This lets us rewrite the equation of motion as

$$-\omega^2\mathbf{p} - \mathrm{i}\gamma_0\omega\mathbf{p} + \omega_0^2\mathbf{p} = \beta\mathbf{E} \tag{2.14}$$

$$-(1+\mu_0\mu\,\beta\,G_\mathrm{self})\omega^2\mathbf{p} - \mathrm{i}\gamma_0\omega\mathbf{p} + \omega_0^2\mathbf{p} = \beta\mathbf{E}_\mathrm{dr}. \tag{2.15}$$

We can consider the real and imaginary parts of G_self separately. The imaginary part has the effect of an additional damping term and for that reason is generally interpreted as radiative damping: damping due to energy radiated into the far field. Its value is found from equation 2.13 as $\mathrm{Im}(G_\mathrm{self}) = k/(6\pi) = \sqrt{\mu_0\mu\varepsilon_0\varepsilon}\,\omega/(6\pi)$. The real part in essence causes a shift of the undamped resonance frequency ω_0. The peculiar fact that $\mathrm{Re}(G_\mathrm{self})$ diverges, per equation 2.13, is a consequence of abstracting a finite-sized scatterer to a point dipole. A regularisation procedure, which is beyond the scope of this work, resolves this divergence by defining an exclusion volume that restores finite polarisation density [6, 24, 25]. In practice, this captures the $\mathrm{Re}(G_\mathrm{self})$ term in a new ω_r, replacing ω_0. The full equation of motion then reads

$$\left[-\mathrm{i}\mu_0\mu\,\beta\,\frac{\sqrt{\mu_0\mu\varepsilon_0\varepsilon}}{6\pi}\,\omega^3 - \omega^2 - \mathrm{i}\gamma_0\omega + \omega_\mathrm{r}^2\right]\mathbf{p} = \beta\mathbf{E}_\mathrm{dr}. \tag{2.16}$$

We see that the imaginary part of G_self makes the equation anharmonic. It may be interpreted as modifying the damping rate of the dipole, though with a stronger frequency dependence than the intrinsic damping. In the limit of small r_ant, we have small β and we retrieve harmonic oscillator behaviour.

2.2.2. SCATTERING CROSS-SECTION AND ALBEDO

For any scattering problem we can define the scattering cross-section

$$\sigma_{\mathrm{sc}} = \frac{P_{\mathrm{rad}}}{\langle S_{\mathrm{dr}} \rangle} \tag{2.17}$$

with total reradiated power P_{rad} and cycle-averaged incoming energy flux $\langle S_{\mathrm{dr}} \rangle$. For a propagating wave, we have $\langle S_{\mathrm{dr}} \rangle = \sqrt{(\varepsilon_0 \varepsilon)/(\mu_0 \mu)} |\mathbf{E}|^2/2$. Time-averaged radiated power is found from the Larmor formula $P_{\mathrm{rad}} = \mu_0 \mu \sqrt{\mu_0 \mu \varepsilon_0 \varepsilon}\, \omega^4 |\mathbf{p}|^2/(12\pi)$ [26], such that for a single particle

$$\sigma_{\mathrm{sc}} = \frac{(\mu_0 \mu)^2}{6\pi} \omega^4 |\alpha|^2 \tag{2.18}$$

with single-particle polarisability along the driven axis α. With the fourth-order dependence on ω and $|\alpha| \propto r_{\mathrm{ant}}^3$, this equation shows the scaling as $\sigma_{\mathrm{sc}} \propto r^6/\lambda^4$ of scattering by small, off-resonant particles that Rayleigh found by dimensional analysis [27]. For large particles, the third-order term in equation 2.16 dominates and we can insert this into 2.18 to find

$$\sigma_{\mathrm{sc,unit}} = \frac{(\mu_0 \mu)^2}{6\pi} \omega^4 \frac{36\pi^2}{(\mu_0 \mu)^2 \varepsilon_0 \varepsilon \omega} = \frac{6\pi}{\mu_0 \mu \varepsilon_0 \varepsilon} \frac{1}{\omega^2} = \frac{3}{2\pi} \lambda^2. \tag{2.19}$$

This limit is known as the unitary limit as it represents full reemission of captured energy. We can confirm these trends by numerically integrating calculated far-field energy flux for various particle radii, as seen in figure 2.2. Albedo for a nanoparticle is the ratio of radiated power to total captured power $P_{\mathrm{tot}} = P_{\mathrm{rad}} + P_{\mathrm{abs}}$, i.e. radiated power plus absorbed power. From our results here, we see that small particles have near-zero albedo, as they absorb nearly all of the energy they interact with. Large particles have near-unity albedo, re-emitting almost all the energy they capture.

2.2.3. SETS OF INTERACTING DIPOLES

We wish to find the field distribution from a set of dipoles $\mathbf{p} = \{\mathbf{p}_j\} = \{p_{jn}\}$ with positions $\mathbf{r}' = \{\mathbf{r}_j\} = \{[x_j, y_j, z_j]\}$ and natural frequencies $\{\omega_{1,j}\}$ in an external driving field. For any particular dipole $\mathbf{p}_i$ we have

$$\mathbf{E}_{\mathbf{p}_i}(\mathbf{r}) = \mu_0 \mu \omega^2 \overleftrightarrow{\mathbf{G}}(\mathbf{r}, \mathbf{r}_i) \mathbf{p}_i. \tag{2.20}$$

Dipole moments $\mathbf{p}_i$ must be found by solving the self-action corrected equation of motion from section 2.2.1 with an additional interaction term. Rederiving equation 2.16 with an additional field term we find

$$\left[-\mathrm{i}\mu_0 \mu\, \beta \frac{\sqrt{\mu_0 \mu \varepsilon_0 \varepsilon}}{6\pi} \omega^3 - \omega^2 - \mathrm{i}\gamma_{0,i}\omega + \omega_{\mathrm{r},i}^2 \right] \mathbf{p}_i \tag{2.21}$$

$$= \beta_i \mathbf{E}_{\mathrm{dr}} + \beta_i \sum_{j \neq i} \mathbf{E}_{\mathbf{p}_j}(\mathbf{r}_i) \tag{2.22}$$

$$= \beta_i \mathbf{E}_{\mathrm{dr}} + \beta_i \sum_{j \neq i} \mu_0 \mu \omega^2 \overleftrightarrow{\mathbf{G}}(\mathbf{r}_i, \mathbf{r}_j) \mathbf{p}_j. \tag{2.23}$$

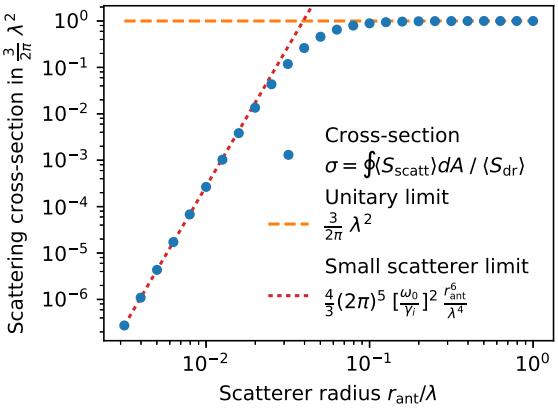

Figure 2.2: Scattering cross-section for particles of various sizes. Calculated values are shown compared to the small-particle and large-particle limits.

We can gather up the interdependence into a matrix $\overleftrightarrow{\boldsymbol{\alpha}}^{-1}$ relating $\mathbf{p} = \{p_{jn}\}$ to $\mathbf{E}_{\mathrm{dr}} = \{E_{\mathrm{dr},n}(\mathbf{r}_j)\}$ as

$$\overleftrightarrow{\boldsymbol{\alpha}}^{-1}\mathbf{p} = \mathbf{E}_{\mathrm{dr}}. \tag{2.24}$$

The tensor $\overleftrightarrow{\boldsymbol{\alpha}}^{-1}$ (like $\overleftrightarrow{\boldsymbol{\alpha}}$) will now have dimensions $3n_j \times 3n_j$, forming an inverse polarisability tensor relating external fields to dipole moments. In order to facilitate further analysis, we introduce the dimensionless variables

$$\hat{\omega} = \frac{\omega}{\omega_{\mathrm{c}}} \tag{2.25}$$

$$\hat{\gamma} = \frac{\gamma}{\omega_{\mathrm{c}}} \tag{2.26}$$

$$\hat{r}_{ij} = \frac{r_{ij}}{\lambda_{\mathrm{c}}} = \frac{\sqrt{\mu_0\mu\varepsilon_0\varepsilon}}{2\pi}\omega_{\mathrm{c}} r_{ij} \tag{2.27}$$

$$\hat{\beta} = \frac{\mu_0\mu}{2}\frac{\beta}{\lambda_{\mathrm{c}}} = \frac{\mu_0\mu\sqrt{\mu_0\mu\varepsilon_0\varepsilon}}{4\pi}\omega_{\mathrm{c}}\beta = (k_{\mathrm{c}} r_{\mathrm{ant}})^3 \tag{2.28}$$

and write the entries of $\overleftrightarrow{\boldsymbol{\alpha}}^{-1}$ as

$$\alpha^{-1}_{in,jm} = \frac{\mu_0\mu}{2}\frac{\omega_{\mathrm{c}}^2}{\lambda_c}\begin{cases} -\mathrm{i}\frac{2}{3}\hat{\omega}^3 - \frac{1}{\hat{\beta}_i}\hat{\omega}^2 - \mathrm{i}\frac{\hat{\gamma}_{0,i}}{\hat{\beta}_i}\hat{\omega} + \frac{\hat{\omega}^2_{\mathrm{r},i}}{\hat{\beta}_i} & i = j,\ n = m \\ 0 & i = j,\ n \neq m \\ -\frac{\mathrm{e}^{\mathrm{i}2\pi\hat{\omega}\hat{r}_{ij}}}{2\pi\hat{r}_{ij}}\left[\left(1 + \frac{\mathrm{i}2\pi\hat{\omega}\hat{r}_{ij} - 1}{4\pi^2\hat{\omega}^2\hat{r}_{ij}^2}\right) + \left(\frac{3 - 3\mathrm{i}2\pi\hat{\omega}\hat{r}_{ij}}{4\pi^2\hat{\omega}^2\hat{r}_{ij}^2} - 1\right)\frac{\hat{n}\hat{m}}{\hat{r}_{ij}^2}\right] & i \neq j,\ n = m \\ -\frac{\mathrm{e}^{\mathrm{i}2\pi\hat{\omega}\hat{r}_{ij}}}{2\pi\hat{r}_{ij}}\left(\frac{3 - 3\mathrm{i}2\pi\hat{\omega}\hat{r}_{ij}}{4\pi^2\hat{\omega}^2\hat{r}_{ij}^2} - 1\right)\frac{\hat{n}\hat{m}}{\hat{r}_{ij}^2} & i \neq j,\ n \neq m \end{cases} \tag{2.29}$$

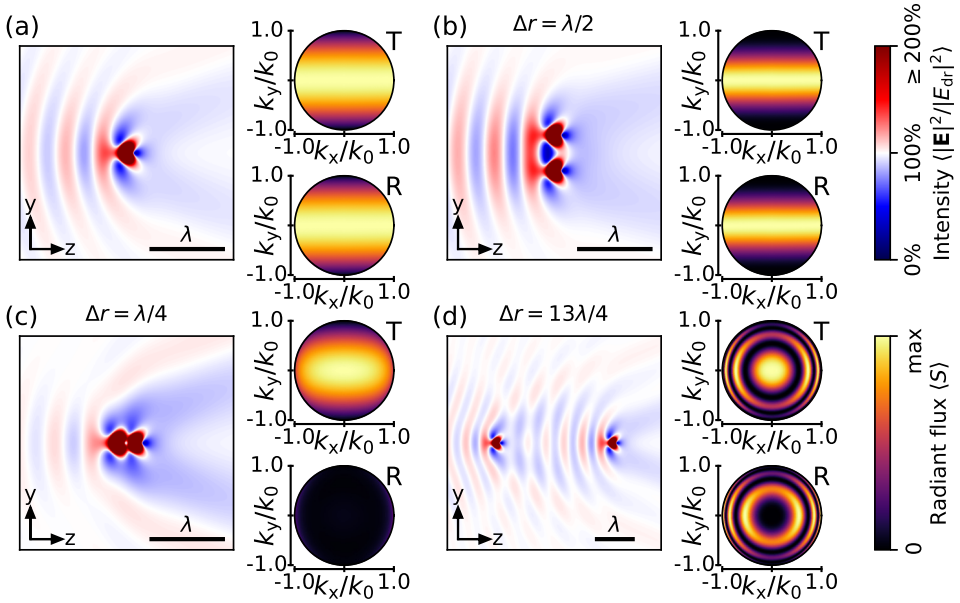

Figure 2.3: Field intensity distribution (square panels) and far-field energy flux (circular panels) for small systems of point scatterers. The scatterers are driven by a plane wave propagating along z and polarised along y. Field intensity is normalised to driving field intensity and clipped to 200% for visibility. The far-field maps are shown versus parallel wavevector $k_\parallel$, where T indicates the forward ($+z$) direction and R the reverse ($-z$) direction. Energy flux is corrected for the apodisation factor and normalised to its maximum for each system individually. (a) A single point scatterer. (b) Two point scatterers, separated along y by $\Delta r = \lambda/2$. (c) Two point scatterers, separated along z by $\Delta r = \lambda/4$. (d) Two point scatterers, separated along z by $\Delta r = 13\lambda/4$.

The inverse polarisability matrix can be inverted numerically for specific systems. Together with the Green's functions of the individual scatterers, this allows calculation of the fields both at specific positions and in the far-field limit. Several examples of such calculations for different systems are shown in figure 2.3. Here we consider particles illuminated from the left along the z-axis with light polarised top-bottom along the y-axis. Shown are two-dimensional cross-sections of local field intensity and far-field energy flux versus parallel wavevector $k_\parallel$ in both forward and reverse directions. Local field intensity is expressed in terms of the intensity of the incident plane wave. In figure 2.3a we see the field around a single dipole scatterer with scattering strength appropriate for an $r_{\text{ant}} = \lambda/12$ particle with $Q = \gamma_0/\omega_r = 10$. Field intensity diverges near the point dipole and we have clipped the colour scale to avoid this. We observe the near-field lobes around the dipole, extended somewhat along the polarisation axis. We also see an interference pattern where backscattering into the incident beam creates a standing wave. The figure also shows far-field images, as might be captured in a high-NA Fourier microscope, as we will discuss in section 2.3. These images have been corrected for the apodisation factor (section 2.3). We recognise the donut profile of dipole radiation, with no radiation towards the poles and uniform intensity along the equator. Due to symmetry the forward and reverse scattering pictures are identical. With two scatterers, the relative configuration affects scattering

patterns. The fields of two scatterers driven in phase, but separated by half a wavelength, will destructively interfere along their separation axis. In figure 2.3b, this leads to further suppression of radiation along $\pm y$. Figure 2.3c, conversely, has drive phase and retardation combine to cancel out back-scattering in the $-z$ direction. With greater separation, we start to see diffraction orders, where certain angles correspond to constructive interference. This is seen in figure 2.3d, though the precise distance still leads to the same cancelling of back-scattering seen in figure 2.3c.

We can further demonstrate the physical use of the model by reproducing a number of results from coupled mode theory. Consider two identical point dipoles separated by $\mathbf{r}$ and driven along that same axis. The inverse polarisability matrix for this system reads

$$\overleftrightarrow{\boldsymbol{\alpha}}^{-1} = \frac{\mu_0\mu}{2}\frac{\omega_c^2}{\lambda_c}\begin{bmatrix} -\mathrm{i}\frac{2}{3}\hat{\omega}^3 - \frac{1}{\hat{\beta}}\hat{\omega}^2 - \mathrm{i}\frac{\hat{\gamma}_0}{\hat{\beta}}\hat{\omega} + \frac{\hat{\omega}_r^2}{\hat{\beta}} & -\frac{\mathrm{e}^{\mathrm{i}2\pi\hat{\omega}\hat{r}}}{2\pi\hat{r}}\frac{2-\mathrm{i}4\pi\hat{\omega}\hat{r}}{4\pi^2\hat{\omega}^2\hat{r}^2} \\ -\frac{\mathrm{e}^{\mathrm{i}2\pi\hat{\omega}\hat{r}}}{2\pi\hat{r}}\frac{2-\mathrm{i}4\pi\hat{\omega}\hat{r}}{4\pi^2\hat{\omega}^2\hat{r}^2} & -\mathrm{i}\frac{2}{3}\hat{\omega}^3 - \frac{1}{\hat{\beta}}\hat{\omega}^2 - \mathrm{i}\frac{\hat{\gamma}_0}{\hat{\beta}}\hat{\omega} + \frac{\hat{\omega}_r^2}{\hat{\beta}} \end{bmatrix}. \tag{2.30}$$

It has eigenvectors $\mathbf{v}_\pm = [1, \pm 1]$, implying one in-phase and one antiphase mode. On resonance the matrix should be singular, so that for the two eigenmodes we require

$$-\mathrm{i}\frac{2}{3}\hat{\omega}^3 - \frac{1}{\hat{\beta}}\hat{\omega}^2 - \mathrm{i}\frac{\hat{\gamma}_0}{\hat{\beta}}\hat{\omega} + \frac{1}{\hat{\beta}} = \pm\frac{\mathrm{e}^{\mathrm{i}2\pi\hat{\omega}\hat{r}}}{2\pi\hat{r}}\frac{2-\mathrm{i}4\pi\hat{\omega}\hat{r}}{4\pi^2\hat{r}^2}. \tag{2.31}$$

This equation is not analytically solvable without further assumptions. In the small-particle limit we can drop the third-order term, but not the coupling term, which may be arbitrarily large. Close to $\hat{\omega} \approx 1$ we can simplify further using $\hat{\omega}\hat{r} \approx \hat{r}$. Considering only positive frequencies the resonance condition is now satisfied at

$$\mathbf{v}_+ = \begin{bmatrix} 1 \\ 1 \end{bmatrix} \qquad \longrightarrow \qquad \hat{\omega}_+ = \mathrm{Re}\left[\sqrt{1 - \left(\frac{\hat{\gamma}_0}{2}\right)^2 - \hat{\beta}\frac{\mathrm{e}^{\mathrm{i}2\pi\hat{r}}}{2\pi\hat{r}}\frac{1-\mathrm{i}2\pi\hat{r}}{4\pi^2\hat{r}^2}}\right] \tag{2.32}$$

$$\mathbf{v}_- = \begin{bmatrix} 1 \\ -1 \end{bmatrix} \qquad \longrightarrow \qquad \hat{\omega}_- = \mathrm{Re}\left[\sqrt{1 - \left(\frac{\hat{\gamma}_0}{2}\right)^2 + \hat{\beta}\frac{\mathrm{e}^{\mathrm{i}2\pi\hat{r}}}{2\pi\hat{r}}\frac{1-\mathrm{i}2\pi\hat{r}}{4\pi^2\hat{r}^2}}\right] \tag{2.33}$$

Increasingly strong coupling shifts the even mode $\mathbf{v}_+$ down in frequency while the odd mode $\mathbf{v}_-$ goes up. For sufficiently small separation the even mode stops oscillating altogether. Through $\mathrm{Re}\left(\sqrt{x}\right) = 0 \rightarrow \mathrm{Re}\,(x) < 0$ we can find a lower bound r_{min} on this separation: for two small, low-loss, spherical particles

$$\hat{r}_{\mathrm{min}} = \frac{1}{2\pi}\sqrt[3]{\hat{\beta}} \qquad \text{or} \qquad r_{\mathrm{min}} = r_{\mathrm{ant}}. \tag{2.34}$$

The frequency of the odd mode meanwhile increases boundlessly. This analysis is the electrodynamic equivalent of a seminal quasi-static analysis of plasmonic hybridisation, in which the normal modes are interpreted as 'bright' and 'dark' modes [28].

Which modes a given field will drive depends on the phase relation between the drive terms at the two positions. We expect the even mode to appear for two particles driven in phase by a field polarised along their axis of separation. An in-phase field polarised perpendicular to the separation will produce coupling with the opposite sign compared to

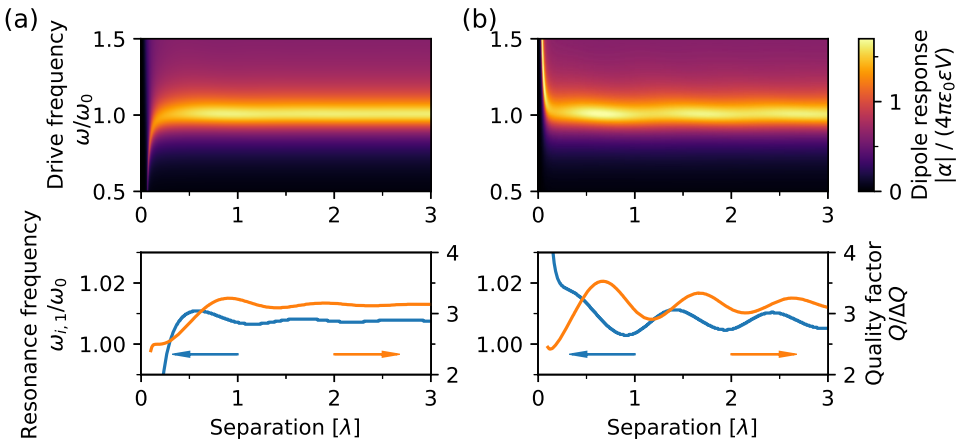

Figure 2.4: Two modes for a pair of identical scatterers, shown by their reponse in dipole moment versus separation and drive frequency. The scatterers have scattering strength as for particles with $r_{\text{ant}} = \lambda/15$ and $Q = \gamma_0/\omega_r = 10$. Top panels show the full spectrogram. Bottom panels show the resonance frequency, found as the frequency of maximum dipole moment, and the quality factor, found as the FWHM linewidth of the response. (a) A positive-coupling mode, found by driving the scatterers with a plane wave polarised along their separation axis. (b) A negative-coupling mode, found by driving the scatterers with a plane wave propagating orthogonal to and also polarised orthogonal to their separation axis.

the previously analysed case, as per equation 2.4. As such, it will couple to a (bright) mode with the opposite trend in frequency. Numeric inversion of the polarisability matrix allows us to calculate the response of such a pair of dipoles versus drive frequency and separation. The results of such calculations, driving positive-coupling and negative-coupling modes separately, are shown in figure 2.4. We recognise the resonance as the frequency where response is largest. With smaller separation, coupling strength increases and resonance frequency shifts in the predicted direction. If we trace the resonance frequency precisely, we also see the effect of retardation in the coupling between the scatterers as an oscillation with a periodicity of λ. A similar effect is seen in the linewidth of the modes. More complicated systems of dipoles can be analysed similarly: by constructing and inverting their coupling matrix, then calculating the near- and far-field distributions resulting from their dipole moments given a drive field.

2.3. FOURIER OPTICS

The angular spectrum representation shows that there is a direct relationship between spatial frequencies and propagation direction. This has a number of consequences for imaging, besides predicting the existence of a diffraction limit. We will evaluate some consequences relevant for the design of imaging systems and discuss the value of imaging in frequency space. In this analysis, we use a simplified ray optics picture, where light is taken to propagate along straight lines (in homogeneous media) and to only change direction by refraction or reflection at interfaces. This approximation is valid in the limit of systems much larger than the wavelength of light [29]. In figure 2.5a we sketch image form-

ation in a standard microscope. We see that for a source in focus on the optical axis, there is a maximum ray angle $\theta_{\max} = \sin^{-1}\left(k_{\parallel}/|\mathbf{k}|\right)$ that still propagates unobstructed through the system. This maximum angle determines the numerical aperture $\mathrm{NA} = n\,\sin\theta_{\max}$ of the optical system. Larger angles may still correspond to propagating waves, but no longer contribute to image formation. In wavevectors terms, we now consider parallel wavevectors with a lower maximum than before: $k_{\parallel} \leq k_{\max} < |\mathbf{k}|$. Since this is still a circular domain in wavevector space, the shape of the imaged spot is the same as for the Airy disc, but wider by a factor $|\mathbf{k}|/k_{\max}$. Numerical aperture thus features in most measures of resolution, including the aforementioned Airy disc zero ring diameter $2r_0 \approx 1.22\lambda/\mathrm{NA}$. In-focus but off-axis sources correspond to rays that after the objective propagate along $k_{x,\mathrm{r}} = |\mathbf{k}|\frac{x}{f_{\mathrm{obj}}}$, and likewise for y. This brings us to another important feature of objectives: their back focal plane. In this back focal plane, the principal rays from all object positions meet. The objective maps rays from all positions $(x_{\mathrm{o}}, y_{\mathrm{o}})$ in the (front) focal plane to rays with $(k_{x,\mathrm{r}}, k_{y,\mathrm{r}})$. Conversely, rays leaving the object position along wavevector $(k_{x,\mathrm{o}}, k_{y,\mathrm{o}})$ pass through positions $(x_{\mathrm{r}}, y_{\mathrm{r}})$ in the back focal plane. The objective is thus seen to perform a two-dimensional spatial Fourier transform between the object in its (front) focal plane and the image in its back focal plane. If the (optically) smallest aperture in the objective is circular and lies in the back focal plane, our analysis on numerical aperture and resolution applies over a range of object positions. The associated parameter, complementary to numerical aperture, is the field of view $\mathrm{FOV} = 2\,r_{\max}$, with $r_{\max}$ the largest distance from the optical axis from which rays may originate and still be mapped to the corresponding positions and wavevectors in the back focal plane. Like the sample plane, the Fourier plane may be imaged on a camera, revealing directly the spatial frequencies that make up a sample. Exploiting the relationships between patterns in real and reciprocal space is the domain of Fourier optics [30].

The same approach can help us answer questions about the design of imaging systems. Specifically, we consider the properties an imaging system must have in order to perform faithful magnification, such that $I\left(x_{\mathrm{i}}, y_{\mathrm{i}}\right) = I\left(M\,x_{\mathrm{o}}, M\,y_{\mathrm{o}}\right)$, where index o represents the object to be magnified and i the resulting image, magnified by M in a ray optics picture. For this simple relation to link the real-space images, their frequency components must be linked by $I\left(k_{x,\mathrm{i}}, k_{y,\mathrm{i}}\right) = I\left(\frac{1}{M}\,k_{x,\mathrm{o}}, \frac{1}{M}\,k_{y,\mathrm{o}}\right)$. Since we have $k_{\parallel} = |\mathbf{k}|\sin\theta$, we require

$$n_{\mathrm{o}}\sin\theta_{\mathrm{o}} = n_{\mathrm{i}}\frac{\sin\theta_{\mathrm{i}}}{M} \tag{2.35}$$

This rule is known as the Abbe sine condition and sets an important requirement on objective design. Since wavevectors are mapped to the back focal plane at different densities, an isotropic source will produce a back focal plane intensity pattern that scales as $I(k_{\parallel}) \propto 1/\cos\theta$. This factor applies to all transformations between front and back focal plane and is known as the apodisation factor. It is often divided out of measured Fourier images to provide a better sense of relative intensities. The sine rule also predicts that well-designed objectives produce a beam width of $d = 2n_{\mathrm{o}}\sin\theta_{\max}\,f_{\mathrm{obj}} = 2\,\mathrm{NA}\,f_{\mathrm{tube,nom}}/M_{\mathrm{nom}}$, with $f_{\mathrm{obj}} = f_{\mathrm{tube,nom}}/M_{\mathrm{nom}}$ the objective focal length, which may be derived from the nominal magnification of the objective M_{nom} at the nominal tube lens focal length $f_{\mathrm{tube,nom}}$ [29, 31]. It is often convenient to approximate lenses as planar devices that refract light as per the thin lens equation, which relates the position of the image of an object s_{i} to the

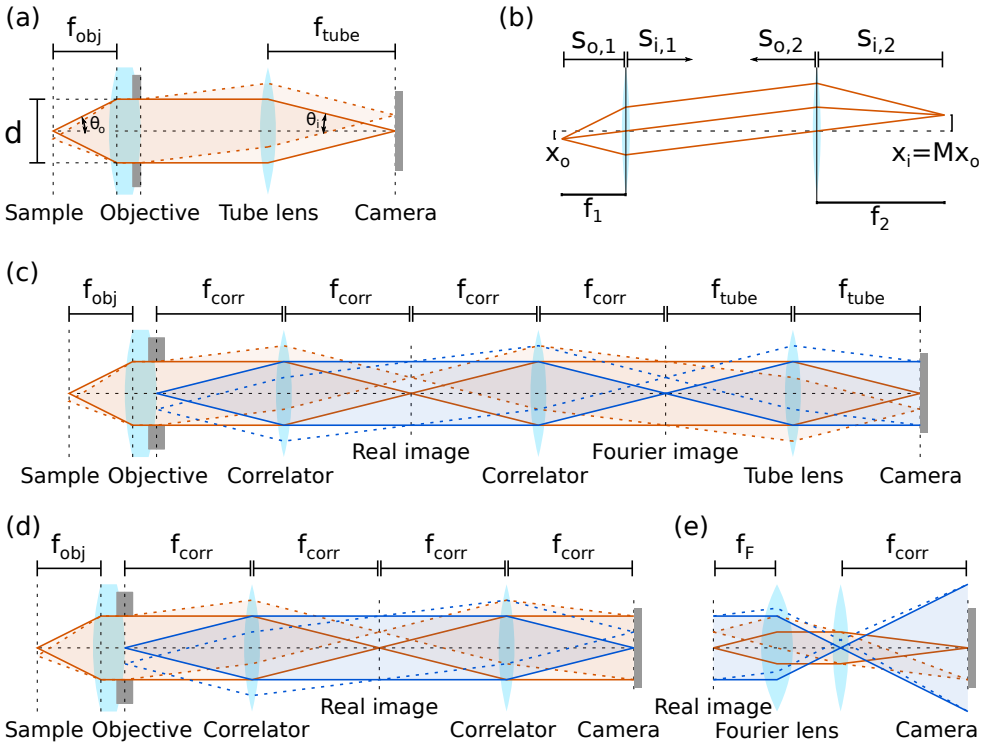

Figure 2.5: (a) Schematic diagram of a conventional microscope, showing finite aperture, ray angles and beam width. (b) Geometrical optics with thin lenses showing an object, an intermediate image at infinity and a magnified final image. (c) An advanced microscope that permits filtering in real and reciprocal space. (d) A Fourier microscope, capable of measuring angle-resolved radiation patterns directly. A real-space image plane can be used for spatial filtering. (e) The Fourier microscope from (d) converted to a real-space microscope by insertion of an additional Fourier lens.

position of that object s_o through its focal length (figure 2.5b) as

$$\frac{1}{s_i} = \frac{1}{s_o} + \frac{1}{f} \tag{2.36}$$

in the convention where all distances are measured with respect to the lens and along positive z (left-to-right). Trigonometry as in figure 2.5b makes clear that ray angles in this approximation are related by $n_o \tan\theta_o = n_i \frac{\tan\theta_i}{M}$. This means that lenses not specifically designed to obey the sine condition can only perform distortion-free imaging in the paraxial limit of long focal lengths compared to beam width, where angles θ are small.

Optical fields may be modified in various ways between the objective and the tube lens. Some such modifications are parasitic and lead to degradation of image quality. For instance, an object that clips part of the beam will distort the final image by removing rays corresponding to spatial features. Deliberate modifications come in two types. There are spatially uniform modifications, like colour filtering, which are best performed in sections of the beam path where propagation is collimated. Normal incidence means

optical distances are as intended, which avoids shifting of interference fringes, and the presence of the material conveniently does not move the effective focal point of the beam. Otherwise, there are spatial modifications. These are normally meant to be made either in real space or in reciprocal space. Real space filtering can be done in the sample plane, but for non-contact methods may be done in any image plane, possibly facilitated by large magnification. Such a real-space filtering set-up is shown in figure 2.5c. Filtering in reciprocal space can be done in the objective back focal plane, thanks to the Fourier action of the objective. As this plane is generally located inside microscope objectives, it is convenient to image the back focal plane and filter in such a Fourier plane. The typical way to do this is through a 4f correlator, a one-to-one telescope that images a plane without modification apart from possible filtering in its Fourier plane. This is also shown in figure 2.5c.

Filtering in Fourier space has a wide range of applications [30]. Perhaps most importantly, direct transmission or specular reflection of an illuminating beam may be blocked. This means that only scattered light is collected and the resulting real-space distribution will be a type of dark-field image. It is important to be aware that filtering in real or reciprocal space, by its very nature, affects the complementary channel. In particular, just as small structures must have broad features in frequency space, observing structures through a narrow spatial filter blurs their Fourier image. Likewise, filtering down to a narrow range of wavevectors blurs spatial images. Real and reciprocal space filtering may still be combined, for instance to limit the collection area and subsequently make dark-field images. Figure 2.5d shows a Fourier microscope, designed to image not the sample plane, but its Fourier transform in the objective back focal plane. Such a microscope may be used in conjunction with real-space filtering, in order to limit the area from which light is collected, by installing spatial filters in any real-space image planes in the microscope. It is often convenient to align Fourier microscopes by first aligning a real-space image. Microscopes can be designed such that a single lens can be added or removed to switch from Fourier imaging to real-space imaging. This is illustrated in figure 2.5e, which shows that adding a single lens to the Fourier microscope from 2.5d will (temporarily) convert it to a real-space microscope. The ability to measure angle-resolved radiation patterns directly makes Fourier optics a powerful tool in the study of nanoscale scattering systems.

2.4. SHEAR-FORCE NEAR-FIELD MICROSCOPY

In order to interact with the near field of a structure, we wish to probe it with a physical object. Since by any definition, the near field does not extend more than a fraction of a wavelength from the sample, this is a significant technical challenge. For dynamical positioning of a probe in the near field of a sample, a distance feedback mechanism is needed. One such method is shear force feedback [32–34]. This technique exploits the additional damping force a laterally vibrating probe experiences when it is brought close to a surface. The nature of this force is a topic of debate and varies between experimental configurations, with adsorbed water, dielectric interactions and nanoscale fluid dynamics all being feasible candidates. For probes brought close to hydrophilic substrates, like glass or the native oxide on silicon, it is likely that the adsorbed water layer is responsible, as evidenced by the strong influence of humidity [34]. We will discuss how this mechanism may be used for near-field probe positioning.

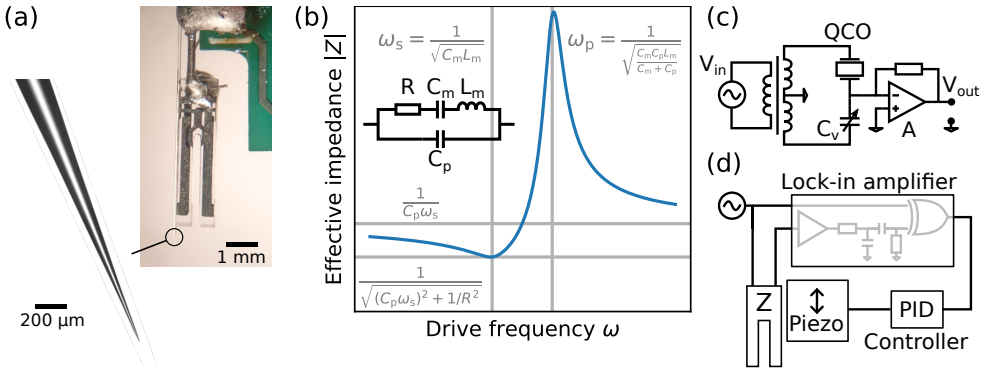

Figure 2.6: Shear force feedback with a quartz crystal oscillator. (a) A pulled fibre end for use as a near field probe, shown mounted on a quartz crystal oscillator and in a magnified image of the tip. (b) The Butterworth-van Dyke equivalent circuit of the quartz crystal oscillator and the main features in its frequency response. During shear-force probe usage, we use the electromechanical series resonance ω_s. (c) Pre-amplifier circuit for measurement of the series resonance circuit impedance. (d) The full shear force control loop, with the tuning fork Z representing the pre-amplifier circuit including the quartz crystal oscillator.

Shear force feedback systems are typically used in conjuction with pulled glass fibres. Such probes are fabricated by laser-induced heating and pulling, which leads to very sharp tips, with radii of curvature as small as 30 nm. In order to induce a mechanical vibration, such fibres are mounted on the side of a quartz crystal oscillator (figure 2.6a). The crystal oscillators used in this work (Premier Farnell X32K768L104) are marketed as tuning fork frequency references and have a nominal resonance frequency of $2^{15} = 32\,768$ Hz. Their frequency response can be modelled by the Butterworth-Van Dyke circuit, which uses a complex impedance (R, C_m, L_m) to encode the electro-mechanical response and a separate electrical capacitance (C_p) between the electrodes (figure 2.6b) [1, 35, 36]. This circuit sustains both a series resonance $\omega_S = 1/\sqrt{C_m L_m}$ and a parallel resonance $\omega_P = 1/\sqrt{C_m C_p L_m/(C_m + C_p)}$. We will use the series resonance. When a fibre tip is mounted, the resonance frequency shifts up by around 1 kHz and quality factor goes down dramatically, from $Q > 10^4$ to $Q \approx 10^3$. These effects are attributed to the combination of stiffening of the arm with the fibre, damping action in the glue, and energy losses to the mount point because the extra mass unbalances the oscillator prongs. In shear force contact, the additional damping force causes the fibre end to lag behind the oscillator prong, exerting a force that acts against the motion and raising the effective spring constant of the oscillator prong [33]. This causes a shift in resonance frequency, as per the circuit model.

For feedback, we first bring the quartz crystal oscillator into resonance by experimentally finding its frequency of minimum impedance. We then activate the control loop and approach a substrate until a phase shift is detected, which indicates a shear force interaction. We measure this frequency shift by way of a pre-amplifier circuit (figure 2.6c) that eliminates the parallel resonance by compensating the C_p capacitance with a small subcircuit that behaves as an adjustable capacitor (C_v). This adjustable capacitor is driven out of phase with the quartz crystal oscillator (QCO) to give it an effective impedance of $C_v = -C_p$. The virtual ground between the crystal oscillator and the variable capacitor

thus only receives signal through the impedance of the series arm of the crystal oscillator equivalent circuit. This signal is amplified (A) to produce the output signal V_{out}. We wish to compare the output signal to the drive signal V_{in} to find the phase shift across the oscillator $\angle Z$ at constant frequency near the series resonance. The resonance shift also causes a change in signal amplitude $|Z|$, but it is understood [33] and has been confirmed experimentally that phase readout is the faster and more reliable way to measure shear force. We use a lock-in amplifier (Stanford Research Systems SR865A) to measure the relative phase $\angle Z$ between the signal generator reference V_{in} and the pre-amplifier output voltage V_{out}. This DC voltage signal is centred to zero voltage at $\Delta\angle Z = \pi/2$ and has amplitude $65\,\text{mV}^{\circ-1}$. This signal is referred to as the error signal. It is used as input to a controller that aims to minimise it by raising or lowering the piezo voltage that sets fork-sample distance. This system is shown schematically in figure 2.6c, where the tuning fork Z represents the full pre-amplifier circuit. During successful operation of the distance control system, the controller keeps phase shift $\angle Z$ constant. This corresponds to constant extra damping force and so, ideally, constant height over the substrate.

We demonstrate shear force distance control by scanning over a deep $50 \times 110\,\text{nm}^2$ slot milled into a layer of gold using a focussed ion beam. We typically scan at a rate of some $500\,\text{nm}\,\text{s}^{-1}$ to give the feedback loop time to adjust for height variations, as the response time of the tuning fork alone is already around 30 ms. We collect topography signal by recording the calibrated extension of the feedback piezo actuator during constant-height scanning. Because height variations may be small compared to substrate tilt over a wide scan, we subtract the plane of best fit. In figure 2.7a we show a topography map, in which we clearly recognise the slot as a depression. Several broad peaks surrounding the slot are likely to be material redeposited during focussed ion beam milling. The slot has a depth of 200 nm, but its apparent depth is under 20 nm. This may be due to the feature being narrow with respect to the radius of curvature of the tip. During scanning we also collect the error signal $\Delta\angle Z$, which tells us whether the phase shift across the oscillator is being kept constant, as intended. If the step response of the feedback loop is too slow for the local sample slope, this will be seen as a peak or dip in phase shift. Our measured error signal vaguely recalls the contours of the topography, but it is mostly dominated by apparently uncorrelated noise. This, combined with the quality of the topography map, tells us our control loop is properly tuned.

In this thesis, we aim to use shear force distance control primarily not for measuring topography, but to perform nanopositioning of optical elements. It is an attractive technique for this application because the crystal oscillator works with very small (few-nanometre) oscillation amplitude, which permits distance-controlled steady-state measurement of optical interactions in addition to lock-in style measurements as are also possible with, for instance, atomic force microscopes.

Optical interactions, of course, depend strongly on material and shape. This means that in order to exploit the capability of positioning scatterers near other objects to the fullest, we would like to be able to position other objects than glass fibre tips. Quartz crystal oscillators have been used in conjunction with a variety of probes for different applications [37, 38]. Similarly, we have developed a technique to mount AFM cantilever tips (Bruker RTESPA-300, Bruker FIB3D2-100 and others) on quartz crystal oscillators. We demonstrate shear force topography mapping with a sharp silicon probe (Bruker

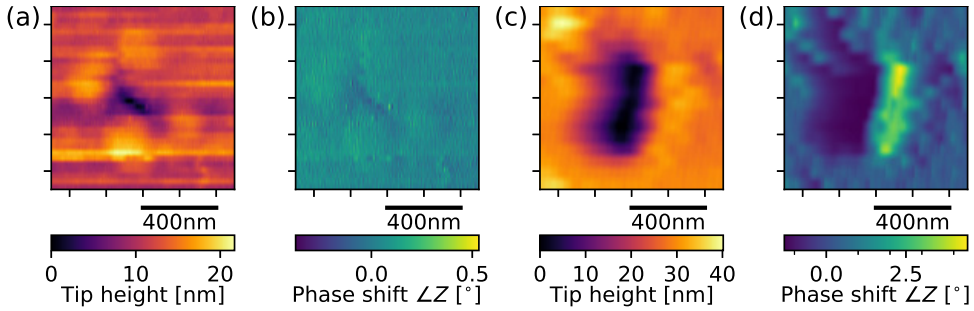

Figure 2.7: (a) Shear force topography mapping with a pulled fibre probe. Measured topography around a slot of nominal dimensions $50 \times 110\,\mathrm{nm}^2$ milled into a layer of gold. (b) Error signal over the same region as (a). (c) Shear force topography mapping with a sharp silicon probe. Measured topography around a slot of nominal dimensions $110 \times 550\,\mathrm{nm}^2$ milled into a layer of gold. (d) Error signal over the same region as (c).

FIB3D2-100) by scanning over a deep $110 \times 550\,\mathrm{nm}^2$ slot milled into gold. The topography measurement again shows a clear and sharp dip (figure 2.7c), demonstrating that distance control works with the composite probe. The corresponding error map (figure 2.7d) is not as smooth as for the fibre probe measurement seen before. This is likely related to the higher scan speed used in this measurement and possibly magnified by the greater depth reached by the probe on its transit across the wider slot. Additionally, the parameters on the PID controller were tuned for minimum error signal with the fibre probes. Different types of probe may require re-tuning. Nonetheless, topography is reproduced faithfully and this method is expected to lead to reliable positioning of nanoscale objects in the optical near-field of a substrate.

2.5. AN INTEGRATED FAR-FIELD OPTICAL AND SHEAR-FORCE NEAR-FIELD MICROSCOPE

We are interested to see how interactions in the optical near field affect a wide variety of far-field optical degrees of freedom. Shear-force feedback provides the means to dynamically position objects over nanometre scales. We additionally want to be able to manipulate various far-field optical degrees of freedom both in illumination and detection. To this end, we develop an integrated real-space, Fourier, spectrometric, polarimetric shear-force microscope with real- and Fourier space filtering capabilities. A schematic overview of this set-up is shown in figure 2.8. The centrepiece is a shear force feedback system. Since we intend to use the shear force probes as scatterers and only illuminate and collect light from free space, this limits us to reflection measurements. Illumination is provided by a supercontinuum laser source (NKT Whitelase Micro) with appreciable intensity from around $\lambda = 500\,\mathrm{nm}$ through to infrared telecom wavelengths. This beam is collimated and may be attenuated by neutral density filters or filtered spectrally by bandpass filters of window 10 nm or 40 nm. A Fourier plane at this point permits filtering in reciprocal space, but wider spots can be achieved more efficiently with a beam expander. This plane is projected onto the back focal plane of the microscope objective (Nikon CFI Plan Apochromat Lambda 60XC, NA = 0.95, air, with cover glass correction) through a 4f-correlator. The

centre plane of this correlator may be used for spatial filtering of the incident beam and typically contains a 200 µm pinhole, which maps to an illumination spot of up to 2.2 µm on the sample. In most measurements, a focussed spot is used instead, diffraction-limited by the objective NA = 0.95. Illumination may be assisted by a white LED used for Koehler (defocussed) illumination of the sample plane.

Collection is done through the same objective, with the input and output paths split by a 50/50 beam splitter. Sample observation may be performed through a CMOS camera (Basler acA1920-uc) in a real-space image plane on the low-light side of a 90/10 beam splitter in the output path. The remainder of the light is imaged through a 4f-correlator on the entrance slit of a spectrometer (Andor Shamrock 303i with iVac 316 CCD camera). The full image camera permits the spectrometer to be used for direct band structure imaging, with wavelength on one axis and k_y in a narrow range of k_x, as selected by the spectrometer entrance slit, on the other. The centre plane of the correlator is used for spatial filtering, often with a 500 µm pinhole, which maps to 5.5 µm on the sample. The correlator also permits insertion of a polariser or wave plate as well as colour and neutral density filters. The correlator may be modified with an optional Fourier lens to project a real-space image on the spectrometer slit, which typically helps with signal level. An optional beam splitter can direct the part of most of the light onto a separate detection path. This path permits Fourier filtering and Fourier- or real-space imaging on another CMOS camera (Basler acA1920-um), with filtering capabilities in both real and reciprocal space. Insertion of a beam splitter also permits simultaneous use of the spectrometer and separate camera. We are thus able to measure position-, wavevector-, colour-, and polarisation-resolved far-field data.

The objective is used in conjuction with samples fabricated on 170 µm glass cover slips. A correction ring allows aberration-free imaging through such cover slips. The sample stage has a three-dimensional piezo actuator (PI Nanocube P-616.3C) for nanometre-precision scans and is motorised for coarse motion (Thorlabs k-cube system on Ultralign 562 stage). Shear force probes are positioned on the sample surface by way of piezo actuators (Piezo Jena PXY80D12 en PZ20D12), with one axis controlled by the analog feedback loop and the other two used for scanning and positioning.

To illustrate the potential this set-up has for testing optical sensing schemes, we collect light scattered off the 50×110 nm^2 slot mapped in figure 2.7a, from the reverse side. Due to its plasmonic resonance the slot works as an optical antenna. Its field profile may be perturbed by the presence of objects in the near field. This experiment thus simulates a set-up for detection of nanoscopic particles or defects, in which the objective and slot antenna together take the role of a near-field scanning head and a probe positioned on the flip side represents a defect on an otherwise homogeneous sample.

When we collect (cross-polarised) scattered light from the slot antenna whilst scanning the probe, we see (figure 2.9a) that integrated intensity falls some 5% when the probe is located right over the antenna. This feature has a width (FWHM) of only 200 nm and is thus sub-diffractive. This is made possible by the close proximity of the slot antenna to the sample, as simulated by the probe. We thus see that shear force feedback can be used to position scatterers in the near field of another object. We will use this ability to explore optical interactions in the near field. We can similarly use the silicon AFM probe from figure 2.7c to study optical interactions. With that probe too, the optical signal shows a dip

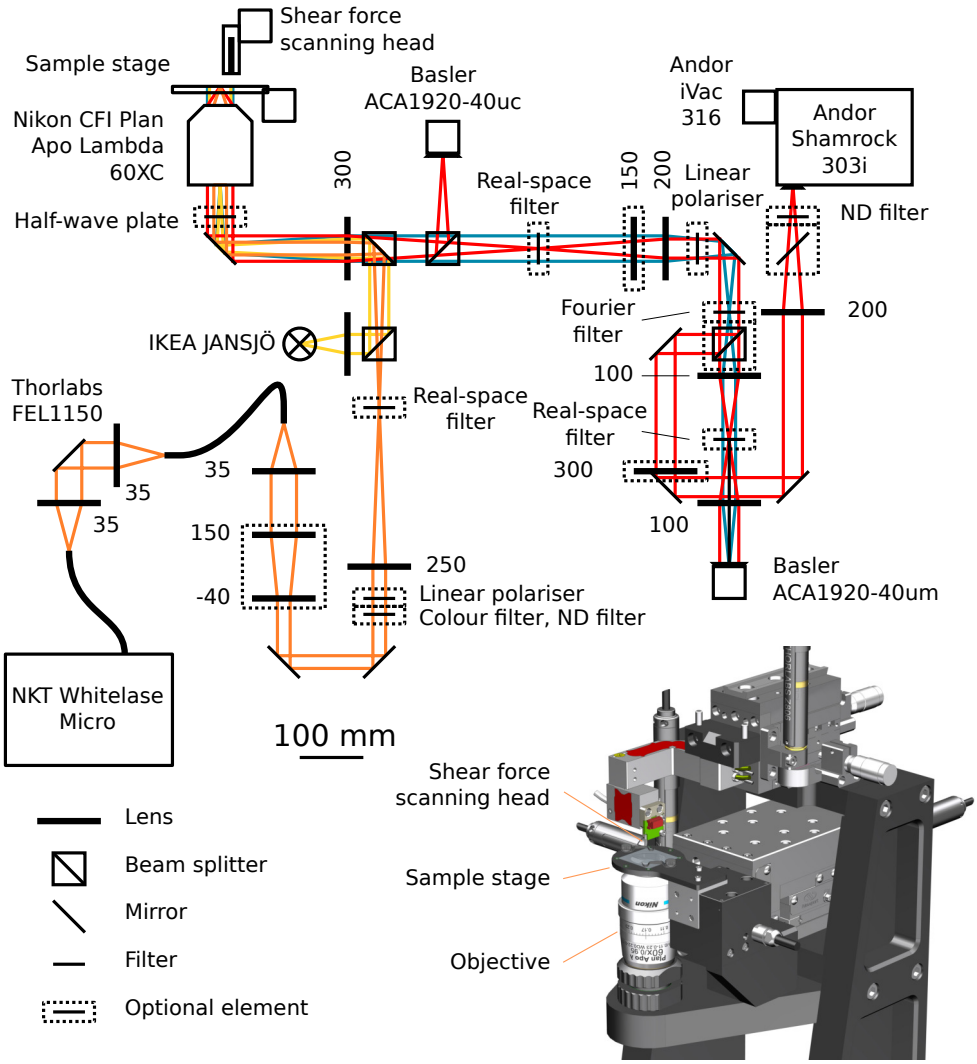

Figure 2.8: Layout of the integrated far-field and shear-force near-field optical microscope used in several chapters of this thesis. Optical beam paths are shown in relation to one another, including convenient filter locations. Distances along the optical axis are shown to scale, component dimensions and beam widths are adjusted for clarity. Relative orientations are accurate up to mirror symmetries, with the objective in reality pointing up and all other optical elements at constant beam height. Various elements are installed on magnetic mounts and can be removed or inserted depending on experimental needs. Beam paths are shown for a configuration permitting simultaneous recording of Fourier images (blue lines) and spatially filtered spectra (red) under small-NA illumination (orange). The beam path for Köhler illumination is also shown (yellow). Inset: CAD drawings of the microscope tower, showing the sample stage, shear force scanning head and objective.

in the same place as the topography signal. This suggests that we are able to detect optical interactions between a silicon tip and the near-field of a slot antenna. The ability to use commercial AFM probes as freely positionable scatterers opens up a world of possibilities,

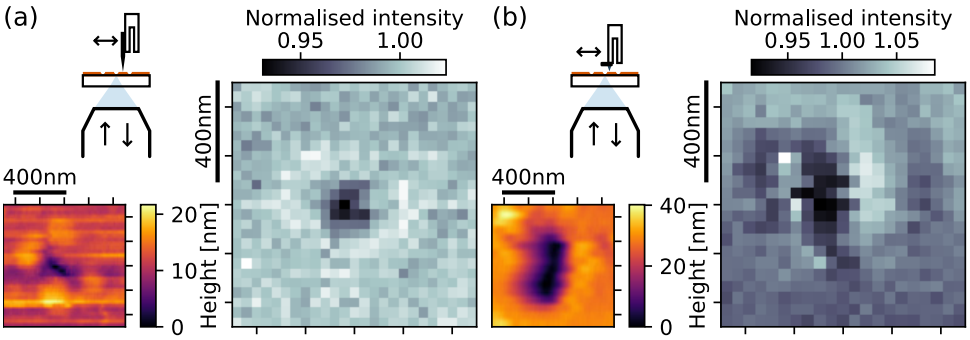

Figure 2.9: (a) Optical interactions between a shear force probe and a plasmonic slot antenna, as per the cartoon drawing. Intensity is integrated over the full collection aperture over a 50 nm band around resonance at 700 nm. The inset shows the corresponding topography map, the same as in figure 2.7a. (b) Studying optical interactions with a composite probe using a sharp silicon tip (Bruker FIB3D2-100). Intensity is integrated over the full collection aperture over a 10 nm band around resonance at 620 nm. The inset shows the corresponding topography map, the same as in figure 2.7b.

from strongly scattering tips coated with any of a number of metals to ultra-sharp carbon nanotubes probes. The insensitivity of the positioning system to the type of probe may also allow scanning with more complex probes with multiple tips or a flat end. These might more accurately simulate the properties of targets of interest or, eventually, allow the experiment to be inverted to actually make the scanning head the moving part. All these developments may help explore the physics of such near-field interactions as well as contribute to a range of possible applications in defect and particle detection.

In this demonstration, we have not yet made use of the Fourier, spectrometric or polarimetric capabilities of the microscope. These will come into play in the following chapters. In chapter 3, we will first develop a general method of retrieving optical parameters from measured data. We will perform such nano-optical information retrieval based on different far-field degrees of freedom in chapters 4, 6 and 7, using experimental data collected in the microscope discussed here.

REFERENCES

1. Horowitz, P. & Hill, W. *The Art of Electronics* 3rd (Cambridge University Press, USA, 2015).
2. Hammond, C. *The Basics of Crystallography and Diffraction* (Oxford University Press, 2015).
3. Maxwell, J. C. “A dynamical theory of the electromagnetic field”. *Philosophical Transactions of the Royal Society of London* **155,** 459–512 (1865).
4. Stein, E. M. & Shakarchi, R. *Fourier analysis: an introduction* 1st (Princeton University Press, 2003).
5. Jackson, J. D. *Classical Electrodynamics* 3rd (John Wiley & Sons, 1999).
6. Novotny, L. & Hecht, B. *Principles of Nano-Optics* (Cambridge University Press, 2006).

7. Airy, G. B. “On the diffraction of an object-glass with circular aperture”. *Transactions of the Cambridge Philosophical Society* **5,** 283 (1835).
8. Strutt, J. W. “XXXI. Investigations in optics, with special reference to the spectroscope”. *Philos. Mag.* **8,** 261–274 (1879).
9. Francia, G. T. D. “Super-gain antennas and optical resolving power”. *Nuovo Cimento* **9,** 426–438 (1952).
10. Berry, M. “Faster than fourier”. in *Quantum Coherence and Reality* (World Scientific, London, 1994), 55–65.
11. Wessel, J. “Surface-enhanced optical microscopy”. *J. Opt. Soc. Am. B* **2,** 1538 (1985).
12. Grober, R. D., Schoelkopf, R. J. & Prober, D. E. “Optical antenna: Towards a unity efficiency near-field optical probe”. *Appl. Phys. Lett.* **70,** 1354–1356 (1997).
13. Zenhausern, F., O’Boyle, M. P. & Wickramasinghe, H. K. “Apertureless near-field optical microscope”. *Appl. Phys. Lett.* **65,** 1623 (1994).
14. Bachelot, R., Gleyzes, P. & Boccara, A. C. “Near-field optical microscope based on local perturbation of a diffraction spot”. *Opt. Lett.* **20,** 1924 (1995).
15. Liu, Z., Durant, S., Lee, H., Pikus, Y., Fang, N., Xiong, Y., Sun, C. & Zhang, X. “Far-Field optical superlens”. *Nano Lett.* **7,** 403–408 (2007).
16. Röhrich, R. & Koenderink, A. F. “Double moiré localized plasmon structured illumination microscopy”. *Nanophotonics* **10,** 1107–1121 (2020).
17. Singham, S. B. & Salzman, G. C. “Evaluation of the scattering matrix of an arbitrary particle using the coupled dipole approximation”. *The Journal of Chemical Physics* **84,** 2658–2667 (1986).
18. Yurkin, M. & Hoekstra, A. “The discrete dipole approximation: An overview and recent developments”. *J. Quant. Spectrosc. Radiat. Transfer* **106,** 558–589 (2007).
19. Weber, W. H. & Ford, G. W. “Propagation of optical excitations by dipolar interactions in metal nanoparticle chains”. *Phys. Rev. B* **70,** 125429 (2004).
20. Niziolek, M. “Review of methods used for computational electromagnetics”. in *2009 2nd International Students Conference on Electrodynamic and Mechatronics* (IEEE, 2009).
21. Sumithra, P. & Thiripurasundari, D. “A review on Computational Electromagnetics Methods”. *Advanced electromagnetics* **6,** 43–55 (2017).
22. Bohren, C. F. & Huffman, D. R. *Absorption and Scattering of Light by Small Particles* (Wiley, 1998).
23. Ashcroft, N. & Mermin, N. *Solid State Physics* (Saunders College Publishing, Philadephia, 1976).
24. Bladel, J. V. “Some remarks on Green’s dyadic for infinite space”. *IRE Transactions on Antennas and Propagation* **9,** 563–566 (1961).
25. Yaghjian, A. “Electric dyadic Green’s functions in the source region”. *Proc. IEEE* **68,** 248–263 (1980).

26. Larmor, J. “LXIII. On the theory of the magnetic influence on spectra; and on the radiation from moving ions”. *Philos. Mag.* **44,** 503–512 (1897).

27. Rayleigh, L. “X. On the electromagnetic theory of light”. *Philos. Mag.* **12,** 81–101 (1881).

28. Prodan, E. “A hybridization model for the plasmon response of complex nanostructures”. *Science* **302,** 419–422 (2003).

29. Born, M. & Wolf, E. *Principles of Optics* 7th (Cambridge University Press, 2019).

30. Goodman, J. *Introduction to Fourier Optics* 3rd (Roberts & Company Publishers, 2005).

31. Abbe, E. “VII.-On the estimation of aperture in the microscope.” *Journal of the Royal Microscopical Society* **1,** 388–423 (1881).

32. Betzig, E., Finn, P. L. & Weiner, J. S. “Combined shear force and near-field scanning optical microscopy”. *Appl. Phys. Lett.* **60,** 2484–2486 (1992).

33. Ruiter, A., van der Werf, K., Veerman, J., Garcia-Parajo, M., Rensen, W. & van Hulst, N. “Tuning fork shear-force feedback”. *Ultramicroscopy* **71,** 149–157 (1998).

34. Rensen, W. *Tuning fork tunes: exploring new scanning probe techniques* (University of Twente, 2002).

35. Butterworth, S. “On electrically-maintained vibrations”. *Proc. Phys. Soc. London* **27,** 410–424 (1914).

36. Dyke, K. V. “The piezo-electric resonator and its equivalent network”. *Proc. IRE* **16,** 742–764 (1928).

37. Göttlich, H., Stark, R. W., Pedarnig, J. D. & Heckl, W. M. “Noncontact scanning force microscopy based on a modified tuning fork sensor”. *Rev. Sci. Instrum.* **71,** 3104–3107 (2000).

38. Taguchi, A., Yu, J. & Saitoh, K. in *Comprehensive Nanoscience and Nanotechnology* 13–32 (Elsevier, 2019).

3

SUPER-RESOLUTION WITHOUT IMAGING: LIBRARY-BASED APPROACHES BASED ON NEAR-TO-FAR-FIELD TRANSDUCTION BY A NANOPHOTONIC STRUCTURE

Super-resolution imaging is often viewed in terms of engineering narrow point spread functions, but nanoscale optical metrology can be performed without real-space imaging altogether. In this chapter, we investigate how partial knowledge of scattering nanostructures enables extraction of nanoscale spatial information from far-field radiation patterns. We use principal component analysis to find patterns in calibration data and use these patterns to retrieve the position of a point source of light. In an experimental realisation using angle-resolved cathodoluminescence, we retrieve light source position with average error below $\lambda/100$. *The patterns found by principal component analysis reflect the underlying scattering physics and reveal the role the scattering nanostructure plays in localisation success. The technique described here is highly general and can be applied to gain insight into and perform sub-diffractive parameter retrieval in various applications.*

The work described in this chapter has been published separately as *ACS Photonics* **7**, 3246-3256 (2020)

3.1. INTRODUCTION

Advances in semiconductor technology and the biological sciences generate great interest in optical characterisation at nanometre scales. Because wide-field microscopy is fundamentally unable to reproduce nanometre-scale details, due to the diffraction limit [1], a wide range of super-resolution techniques, which work around this diffraction limit, have been developed and deployed [2, 3]. These techniques are used in direct imaging as well as in precision metrology, which relies on many of the same phenomena [4, 5]. Many super-resolution techniques rely on exploitation of a carefully engineered point spread function (PSF) that describes the transformation from a point on the sample to the image plane. In the case of fluorescent super-resolution techniques, like photo-activated localisation microscopy (PALM) [6–8], an image is built up by individually identifying and localising optically active sites by fitting their PSF, which requires precise knowledge of the PSF and invokes the assumption that the active sites are sparse point emitters. In contrast, near-field scanning optical microscopy (NSOM) [9–11] achieves high-fidelity images by constructing a maximally sharp PSF, at the cost of a complicated measurement apparatus. Techniques using a PSF either require explicit inversion through computational elimination of the PSF from image features, or produce an image that is smoothed out by convolution with the PSF. In both cases, spatial resolution scales with PSF width and a good PSF model is crucial to the success of the technique.

Looking beyond the paradigms of real space imaging, it is very well possible to circumvent the need for a PSF model and retrieve spatial information from radiation patterns directly. The scattering properties of nanophotonic structures depend strongly on their nanoscale features, with parameters such as relative position, size and permittivity of features all affecting far-field information channels such as radiation pattern, scattering spectrum and total radiative rate. Such changes in scattered signals may be observed regardless of the details of the imaging system. Figure 3.1 sketches the particular case where a light source moves in the vicinity of an optical antenna. This displacement leads to clear changes in the radiation pattern (scattered intensity versus direction) as a function of displacement, illustrating the principle that the structure factor of a scattering system provides information about its internal configuration. This insight has already enabled nanoscale information retrieval in particle detection [12, 13], position sensing [14–16] and even imaging [17–19]. Propagation of spatial information through strongly scattering systems has also been studied in the context of imaging through complex media [20–23]. However, the general challenge of imaging-free retrieval of nanoscopic information remains largely unexplored.

In this chapter, we study how a scattering structure in the near field of a sample embeds nanoscopic information into far-field radiation patterns, enabling the experimental retrieval of the position of a point-like source of light with deeply sub-wavelength precision. In doing so, we introduce a general-purpose localisation technique based on principal component analysis, which provides understanding of which features in radiation patterns contribute to localisation precision. We verify that this precision is indeed caused by the scattering structure through comparison with dummy measurements. More generally, we discuss how information about specific features of partially known systems may be extracted from alternative far-field channels such as radiation patterns, rather than from real-space imaging of parts of a sample.

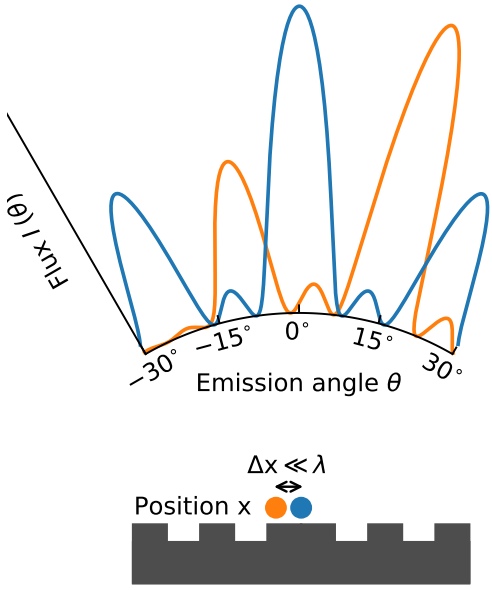

Figure 3.1: Nanoscale changes in system parameters can strongly modify far-field scattering behaviour. Here, a shift in scattering patterns reveals the small displacement of a light source with respect to a scattering structure.

3.2. PARAMETER RETRIEVAL METHOD

To demonstrate our parameter retrieval procedure, we first discuss a synthetic experiment on basis of a theoretical toy model. This model consists of a point source of light located in a plane that lies a fraction of a wavelength below a sub-diffractive linear array of four scattering sites, as shown schematically in figure 3.2a. We consider strong scatterers with parameters such as we might find for the plasmonic resonance of silver nanoparticles 100 nm in diameter [24]. Our objective is to retrieve the position of the light source with respect to the array, just from far-field scattering patterns. We describe this system with a discrete dipole model. As discussed in section 2.2, this powerful tool to study the qualitative behaviour of collections of scattering sites [25–28] natively includes multiple scattering, self-action and propagation delay [29, 30]. Multiple scattering leads to induced dipole moments for each of the array antennas, depending on light source position. Variations in the far-field scattering patterns then result from interference between the different scattering pathways. Fig 3.2b and 3.2c show calculated scattering patterns for two positions of the light source, plotted as radiant flux as function of parallel momentum into the upper half-space above the structure and source. The parallel momentum $k_x = k_0 \cos\phi \sin\theta$ and $k_y = k_0 \sin\phi \sin\theta$ is equivalent to a reporting of azimuthal angle ϕ and polar angle θ (angle relative to the normal to the scattering target), and this type of scattering pattern is readily measured in nanophotonics, for instance through back-focal plane detection [31–33]. In the present example, the radiation pattern has only a comparatively broad feature due to the small spatial extent of the target (figure 3.2b). The pattern shifts and changes upon a change of source position (compare figures 3.2c and 3.2b). A set of such

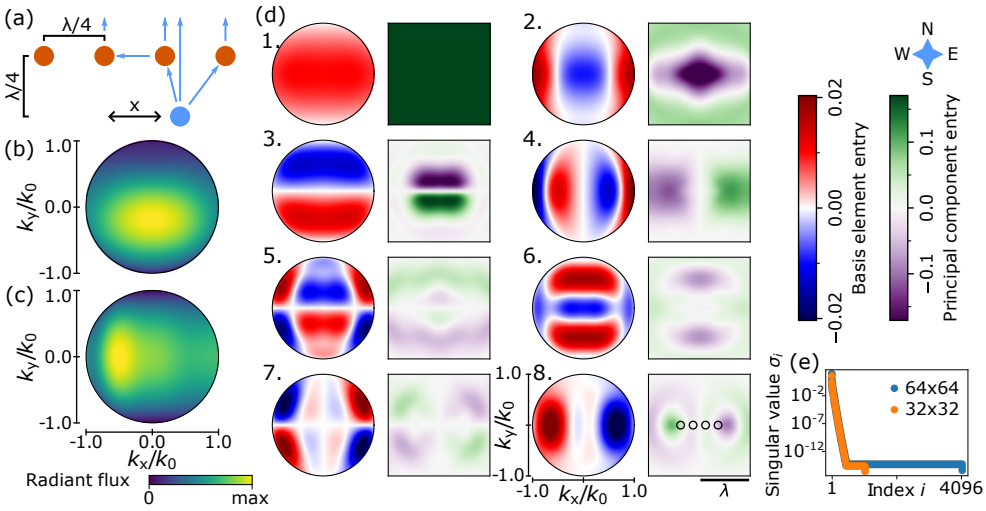

Figure 3.2: Library-based parameter retrieval from synthetic far-field scattering patterns. (a) Layout of the scattering problem: a light source moves with respect to a four-element chain of scatterers. (b) Calculated scattering pattern for the light source 0.25λ south of the centre of the array. (c) Scattering pattern for a light source 0.90λ east of centre. (d) Singular value decomposition of a set of reference radiation patterns. Round panels show radiation pattern basis elements versus wavevector and square panels show principal components versus reference position. Numbers indicate the index of the element, as ordered by singular value. Black circles indicate the position of the array elements. (e) Singular values for the decomposition in (d) and for the same problem at half the spatial resolution.

scattering patterns for light source positions spaced $\lambda/32$ apart, in a 64×64 grid, constitutes a library of synthetic reference data.

In order to systematically identify patterns in the library, we employ the technique of principal component analysis (PCA), which is used in a variety of fields to help detect patterns in complicated datasets [34–36]. Specifically, we construct a matrix A whose rows contain the pixel intensities for each of the normalised reference images A_i. Reference images are Euclidian normalised to $\|A_i\| = 1$ to help us study patterns without strong effects from intensity variations. Singular value decomposition (SVD) allows any matrix A to be rewritten as $A = U\Sigma V^*$, where the asterisk represents conjugate transposition, with U and V unitary matrices and Σ diagonal [37]. For mathematical convenience, we will work only with libraries that have more pixels per image than images in the library, so that Σ has one entry per reference image. The entries of Σ are the singular values σ_i of the set of images A and represent the weight that each basis element has in the original dataset. For every singular value, the corresponding column of V forms an optimal basis vector, or basis element, and the corresponding column of U presents its overlap with each of the reference images in the dataset A. It is instructive to consider $U\Sigma$ as a single unit, known as the principal components of the dataset A. The basis elements are defined in the same coordinate space as the reference images, meaning that they cover a circular domain in (k_x,k_y)-space. The principal components form maps on the same spatial coordinate grid as the reference positions. Together, they describe the basis that most efficiently reproduce the reference dataset. In particular, when ranked by singular value, the first basis element

has the largest possible overlap with all reference images. Every next basis element has the largest possible overlap with the part of the reference images that is orthogonal to all previous basis elements. PCA thus provides a highly efficient way to encode arbitrary datasets in terms of shared features in their entries.

We now take the SVD of our synthetic reference library in order to investigate what shared features the decomposition identifies. Part of this SVD is shown in figure 3.2d. For each component, we show the basis element of the angle-dependent scattered far-field (left, circular maps, red-white-blue colour scale) and the corresponding principal components as a function of light source position in a plane (right, square maps, green-purple scale). Each set of principal components shows the degree to which the corresponding basis element contributes to the total scattering signal at each position. The complete basis has $64^2 = 4096$ such pairs, one per image in the reference library, of which we show only those few with the largest principal components. The first basis element has large positive value for all wave vectors and its corresponding principal component map show that it is almost uniformly high at all reference positions. This element thus corresponds to the common features shared by all radiation patterns. Further elements have more intricate structure, and moreover present principal components that are position dependent. In other words, these higher order elements quantify the degrees of freedom in the radiation patterns in the library that form the main variation, and the principal components quantify how strongly these elements admix into the response as function of the source position. In linear algebra terms, each given reference image in the library can be decomposed in the basis elements, with expansion coefficients varying exactly as the principal components with source position. The principal component maps thus provide direct information on the position at which any given reference image was taken. Focusing on a salient feature as example, basis elements such as the third show beaming by the array, where moving the light source along the north-south axis (as per the compass in figure 3.2) concentrates light emission in that direction, in line with the literature on plasmonic phased arrays [38–40]. This is also seen in the radiation pattern in figure 3.2b, which corresponds to a position near the maximum of the third set of principal components. As another example, the left and right endpoints of the array (along the east-west axis in the principal component images) appear as special points, at which the sets of principal components vary sharply, particularly visible in the fourth and eighth sets of principal components. We see the westward band of the fourth set of principal components in the radiation pattern in figure 3.2c, corresponding to a position near the eastern edge of the principal component maps. These examples show that PCA can provide an effective summary of the physical response of a complex scattering problem, decomposed into a small set of physically intuitive contributors.

Basis elements and their principal components are seen to have the broadest features for the largest principal components. This matches the interpretation that the largest principal components correspond to the dominant, most general features in radiation patterns. In contrast, the lowest-weight elements (not shown) largely encode numerical details and noise that is orthogonal between reference images. The smooth features of the basis elements show us that the fine angular resolution used in these calculation is not required to recognise the important features. The fact that some, like the seventh and eighth basis elements, rely on specific features at large angles suggests that the large

numerical aperture used is of particular value. As a rule of thumb, the physical size of a transducer ultimately determines the multipole moments that it supports and that radiate into the far field, which in turn determines the angular span over which radiation pattern variations occur. The information relevant for position retrieval is contained in the few basis elements with the largest singular values. Indeed, we see in figure 3.2d that the later pairs are characterised by much finer structure in both the basis element and principal components. PCA of calibration data reveals that only a few features in radiation patterns carry a lot of weight in explaining the full dataset. This indicates that most of the basis can be discarded with little loss of information, allowing efficient storage of the library and affirming that the SVD has identified a small number of important radiation pattern features. An excellent question is how many basis elements (and corresponding principal components) are required to encode the variability in radiation patterns. While mathematically the dimensionality increases with spatial sampling density, in reality the basis elements and their weight in the decomposition are set by the scattering physics. Indeed, simulations with lower sampling density yield the same dominant basis elements and a similar drop off of the magnitude of the singular value with index, as seen in figure 3.2e. Basis functions lose physical significance once their singular value hits a noise floor set by numerical or experimental noise, around index 400 in this example. For a given numerical, synthetic or experimental noise level, the number of relevant basis elements is given by the rate of the singular value drop-off versus index.

In order to use the library for parameter retrieval, we take a radiation pattern for any light source position within the sampled domain and project it onto the optimal basis in the library. The coefficients of this projection are to be compared to the principal components for each reference image. In case the sample radiation pattern is identical to one of the library radiation patterns, there will be a perfect match with the principal components at the corresponding position. More generally, the projection coefficients for any sample radiation pattern form a coordinate vector in a higher dimensional space, in which each of the reference images also has a coordinate, given by their principal components. The best match between sample image and library image can then be obtained by finding the library coordinates that have minimum Euclidean distance to the sample coordinate. This best matching image would then pinpoint the sample image source positions. Quantitatively, in order to produce a match in the range $[0,1]$, matches between a set of principal components $(U\Sigma)_j$ and a sample image S_i normalised to $\|S_i\| = 1$ are calculated as

$$M_{ij} = 1 - \frac{1}{\sqrt{2}} \left\| (U\Sigma)_j - S_i V \right\|. \tag{3.1}$$

Such an analysis can be seen in figure 3.3a, where projection match with each reference position is shown for three sample positions (indicated by circles). For now we do not consider distortions or noise, so the radiation patterns used here are identical to reference data at the same positions. Matches at the correct positions are perfect and there is no ambiguity in the choice of best estimate. Overall, positions closer to the correct position are more similar to the sample data than those farther away, while the precise contours echo the principal components of the reference dataset. The first panel of figure 3.3a, in a corner of the calibrated region, is a fairly good match with most positions far away from the array, due to principal components that peak sharply around the array. Conversely,

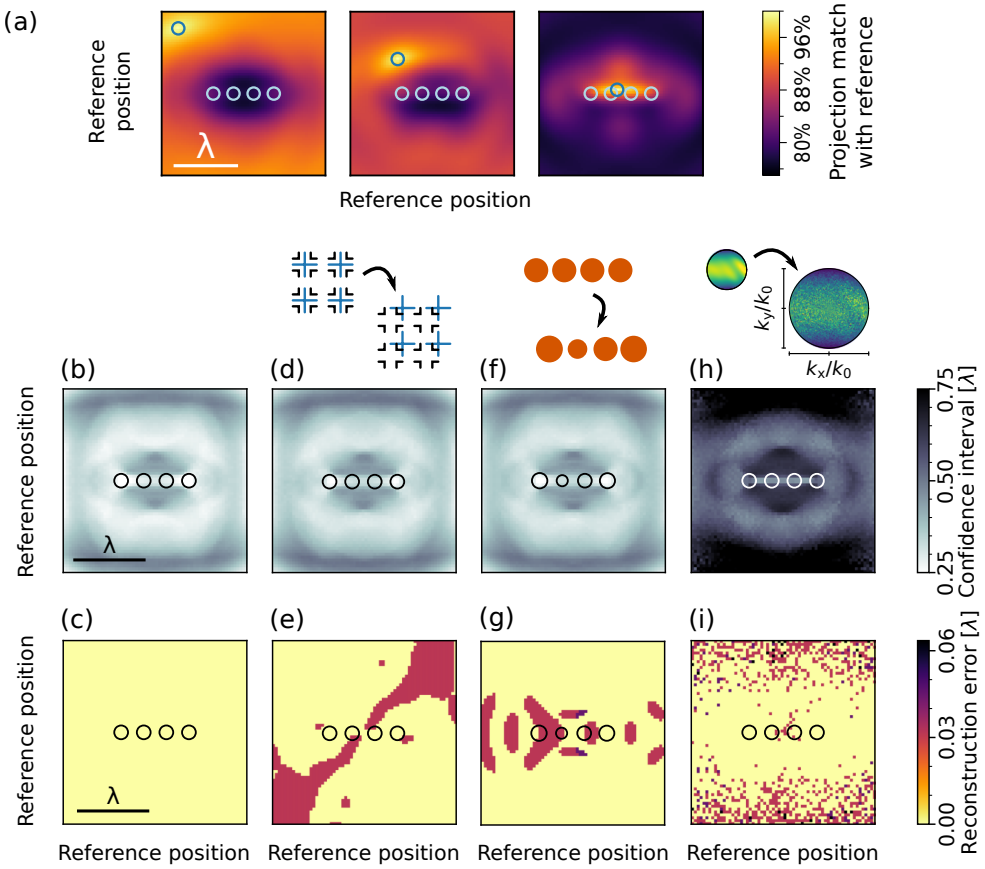

Figure 3.3: Position retrieval using a library. (a) Match between library and ideal data versus reference position for three different light source positions, marked with blue circles. White circles indicate array element positions. (b – i) Localisation confidence interval and sample position reconstruction error versus reference position for four types of data. (b, c) Ideal data. (d, e) Sample positions displaced 30% of a library step to the north and east with respect to library positions. (f, g) Sample data taken with array elements randomly changed in diameter by up to 5%. Circles sized proportionally to element scattering strength. (h, i) Sample data degraded by shot noise as for a signal with an average 3 counts per pixel, as shown to left of (h).

the third panel matches fairly well only with positions close to the array. In all three cases, the specific structure of principal components around the sampled positions allows unambiguous position retrieval.

To maximise robustness to noise, projection match should peak as sharply as possible. Peak sharpness can thus be taken as a measure of *localisation confidence* in noisy systems. We quantify this confidence by defining a viability threshold Θ: points significantly above the median match in the projection maps are considered viable solutions, by $\Theta = \eta \max(M) + (1-\eta)\,\mathrm{median}(M)$, where M are the match values between a given scattering pattern and each library entry. Practically, we use a viability criterion $\eta = 1 - 1/\mathrm{e} \approx 63\%$, in line with common definitions of linewidth. With this threshold, we find the number of

points larger than the threshold N_v and define the confidence interval W as the full-width of a symmetric peak of equal area,

$$W = \sqrt{\frac{4}{\pi}}\,\Delta r\,\sqrt{N_v} \tag{3.2}$$

where Δr is library sampling step size. This measure of confidence, shown in figure 3.3b, generally behaves as we would expect: it is maximal at the ends of the array and low far away from it. The finest confidence intervals are found where the library's principal components (figure 3.2d) have the largest gradients, like in the position indicated in the middle panel of figure 3.3a, where both the second and third sets of principal components are strongly position dependent; conversely, no principal components vary strongly just north and south of the array, leading to low confidence in those regions. Confidence also peaks in the corners of the reference region, as an artefact resulting from the relative rarity of neighbours. Features seen in the confidence map are robust to the precise value of η, remaining similar all the way from $\eta = 50\%$ to $\eta = 80\%$. This allows the confidence intervals to be used to evaluate how sensitively a given transducer lets us retrieve position, or parameters more broadly, in different regions.

In our demonstration so far, we have used the same synthetic data for calibration and testing. This leads to correct retrieval of all positions, as seen in figure 3.3c, where the distance between known sample position and best estimate based on library comparison is shown versus reference position. In practical use, we expect various non-idealities. Sample data may be taken at slightly different positions than reference data, the transducer may be different between reference and sample measurements and signals may be noisy. We will study the effects of each of these distortions in our theoretical model. First, we consider position retrieval with sample data taken on a grid of positions displaced by 30% of the step size ($\lambda/32$) to the north and east with respect to the reference grid and project these onto the original library. Projection matches are visually indistinguishable from the data in figure 3.3a, as they should be: the projection matches are smooth and the confidence map shows a feature size of roughly $\lambda/2$, so a step of under $\lambda/32$ should not make much of a difference. Localisation confidence itself is affected slightly, as seen in figure 3.3d, which we attribute to the shift in position causing a slight broadening of the projection match peaks. Though each sample position still has a clear nearest reference position, the best estimate does not always find this position, as seen in figure 3.3e. As the principal component landscape is not flat, one of the three other surrounding reference positions may indeed provide a better match than the nearest reference position. Where the nearest position is not the best match, the best match is found either one step east or one step north in every case, supporting this interpretation. In experiment, noise may make it more likely that a further-off point provides the best match. In the low-noise regime, symmetry may still be broken by numeric artefacts in the low-weight basis elements. We also note that much larger sample positioning errors would bring the new sample positions closer to other reference positions, which would lead to reliable localisation with a fixed offset, so that the current scenario should be considered the worst case for this type of error. The second type of non-ideality concerns our assumption that the transducer does not change. In practice, it may be desirable to use calibration for one device to perform parameter retrieval with another, despite minor fabrication imperfections. Any single transducer

may also degrade over time. To judge the effect of such changes, we calculate sample data using the original reference positions, but changing the effective diameter of each array element by a random amount up to 5%, as might occur in a lithography process. We apply our parameter retrieval procedure, again using the original library. As for the shifted sampling grid, projection matches are visually indistinguishable from those figure 3.3a, but localisation confidence intervals (figure 3.3d) broaden slightly, similar to the shifted case. Best match positions are off in a number of places, but errors are under two steps ($\lambda/16$) everywhere. Finally, we explore the effect of noise. We calculate radiation patterns affected by shot noise as for an average signal level of 3 counts per pixel over our 181×91 pixel detector. We attempt position retrieval using the original library. Confidence intervals (figure 3.3h) are much more broad than for the other cases as the noise makes library match worse for all positions. Despite the high noise level, the vast majority of positions are retrieved correctly and errors of two steps or more are rare. Most errors occur near the north and south ends of the reference area, far from the array, where confidence intervals are broadest. The scenarios explored here represent a wide range of experimental imperfections. Each shows limited impact on localisation success. This makes us confident that the parameter retrieval technique will prove robust to the differences between different experimental realisations.

The success of this theoretical demonstration allows us to reflect on the main merits of our approach, as opposed to other possible approaches that retrieve position information from far field scattering patterns. In particular, our proposed method envisions a library-based retrieval that applies PCA to *real-world* calibration data, in other words proposing a matching of measured data to a previously *measured* library. This should be juxtaposed to model-based/model assisted approaches. Scattering properties of complex nanophotonic structures can be predicted through a number of theoretical and numerical methods, ranging from quasi-exact discrete dipole models to full-field simulation with finite element or finite-difference time-domain methods. While these techniques can solve many scattering problems to arbitrary accuracy, they require fine knowledge of the structure of interest for their results to be applicable. The most ambitious model-based parameter retrieval would be to attempt inversion of the scattering problem. While in the simplest of cases, it may be possible to invert scattering problems analytically by working out the parameter dependence of certain far-field information channels, this route of direct inversion is generally infeasible to retrieve arbitrary parameters for realistic systems. The difficulty stems from the non-separable dependence of observables on various parameters, including possible quantities of interest, caused by two aspects of the physics at play. In the dipole scatterer at hand, coupling between different induced dipoles depends non-linearly on relative positions and drive frequency. Moreover, optical experiments have much more convenient access to field intensity than to the full complex field, which precludes direct numerical back-propagation of the far-field data to reconstruct the light source.

Without a direct inversion approach, parameter retrieval would have to be performed through some combination of tabulating forward modeling results and matching to measured data. This approach would be tantamount to building a library of model results instead of measured reference data. In large-scale applications, like CMOS manufacturing fabrication processes, that are very well characterised, such a priori predictive approaches may prove valuable. Unfortunately, for most other branches of nanofabrication to realise

scattering structures, the predictions of models are generally not robust to the fabrication imperfections that occur in actual devices. We argue, based on the present work, to instead make use of real-world calibration of scattering patterns without any assistance from modeling. This has the benefit that it only requires experimental conditions and device properties to be unchanged between the moment of building up the library for a structure, and use of the structure for metrology. Indeed, as our experimental realisation (reported below) shows it is entirely possible to build up a library of scattering patterns versus some known parameter for a single device without knowing or modeling the precise device geometry, and without needing to account for any distortions of the far field patterns downstream in the optical measurement system. Given sufficiently low noise and an appropriate comparison algorithm, the library entry with the same parameter values will provide an excellent match to the experimental result without recourse to modeling.

Finally, we note that the concept of a library, and subsequent retrieval of parameters allows for other solutions than PCA-based techniques. Recently, several groups have addressed related challenges through machine learning, successfully retrieving parameters with sub-diffractive precision as good as $\lambda/25$ for optical wavelength λ [41, 42]. For such demonstrations, the number of distinguishable parameter values is typically orders of magnitude smaller than the size of the 'training set', i.e. the size of the calibration library that is required. In an additional drawback, it is often difficult to interpret how the neural network performs its function and whether it is robust to minor changes in parameters, regularisation being one of the oldest [43] and toughest [44] problems in machine learning. Instead, using a calibration-based, transparent method, we precisely retrieve parameter values with small reference libraries and additionally gain insight into the structure of the reference data.

3.3. EXPERIMENTAL REALISATION

We demonstrate the proposed imaging-free super-resolution technique experimentally, by retrieving the position of a point-like source of light with respect to a known scattering nanostructure. We induce point-like light emission by focusing a high-energy electron beam (30 keV) on a substrate in a scanning electron microscope. Where the electrons cross the vacuum/gold interface, the rapid change in electric field dynamically polarises the material, causing light emission through cathodoluminescence [45, 46]. For optical purposes, this light source can be modelled as a radiating out-of-plane point dipole at the interface, its apparent size being set by the focal spot of the electron beam [47, 48]. We collect the light emitted in this process using a parabolic mirror of acceptance angle 1.47 sr and project it onto a camera, revealing the radiation pattern as radiated intensity versus emission angle [49, 50]. We filter the light down to a band around $\lambda = 500$ nm to avoid washing out of features in radiation patterns. Figure 3.4a schematically shows the key parts of our angle-resolved cathodoluminescence setup. As scattering nanostructure we use a bullseye antenna, a type of structure well-known for its strong beaming [51] and widely used to control light emission from nanoscale sources [33, 52–56]. The antenna, shown in figure 3.4b, is fabricated by FIB milling of monocrystalline gold and consists of a 1.2 µm plateau surrounded by 8 concentric grooves, 600 nm in width and around 100 nm in depth, separated by ridges 600 nm in width. With a point-like light source on the symmetry axis of the bullseye, the radiation pattern will likewise be cylindrically symmetric. As the light

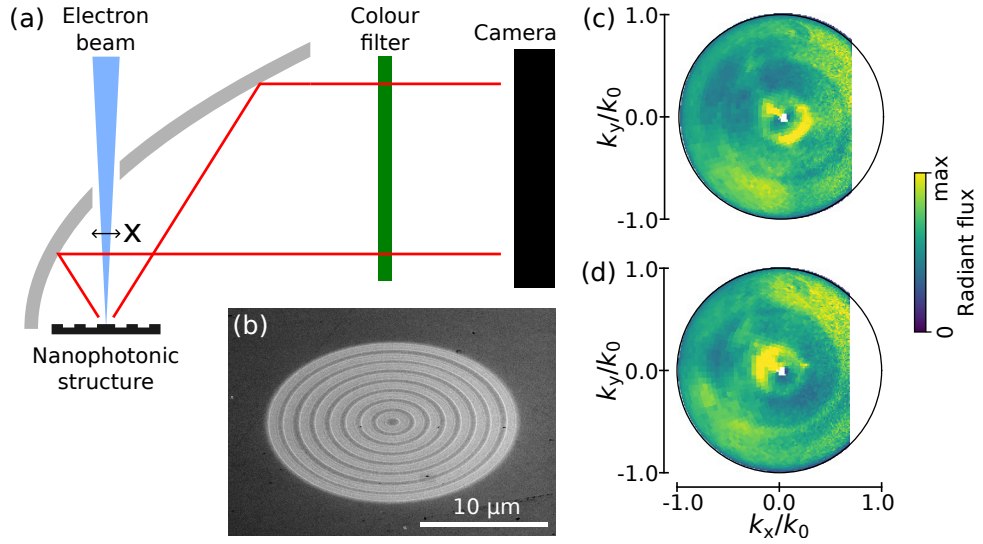

Figure 3.4: Experimental realisation of a light source moving with respect to a nanophotonic structure. (a) Layout of the main parts of the cathodoluminescence setup used in these experiments. An electron beam is focussed onto a bullseye antenna and induces light emission. A parabolic mirror, with its focal point on the antenna, captures this light and directs it through a colour filter to a camera. (b) The bullseye antenna used in the measurements presented here. (c) Radiation pattern constructed from camera image with light source 500 nm ($=\lambda$) north-west of centre on the central plateau of the bullseye antenna. Wavevectors not captured by the mirror are masked in white. (d) Like (c), but with light source 500 nm south-east of centre.

source moves away from the symmetry axis, the radiation pattern shifts as propagation delay changes the relative phase between scattering sites.

We capture such radiation patterns and transform them to momentum space [49], leading to images of radiant flux versus emission direction like those shown in figures 3.4c and 3.4d, taken at positions 500 nm north-west (3.4c) and south-east (3.4d) of the bullseye antenna centre. The main feature in both patterns is a ring-like structure around the centre that shifts its intensity maximum to different angles as electron beam position changes. This feature is attributed to beaming and matches literature reports on similar structures [50]. Blind spots caused by the finite extent of the mirror and a hole through which the electron beam reaches the sample do not hinder observation of the position-dependent features.

We now compose a reference dataset for 8×8 electron beam positions in a grid with 100 nm ($\lambda/5$) steps. This grid is situated around the centre of the central plateau of the bullseye antenna and covers most of it; figures 3.4c and 3.4d correspond to the radiation patterns at two opposite corners. We normalise the dataset as before and take its SVD in order to apply our localisation algorithm. Figure 3.5a shows part of the SVD constructed for this dataset. Like for the synthetic data, the first basis element is a largely position independent background. Subsequent elements again show smooth features both in basis elements and in position dependence. For instance, one may recognise beaming along both diagonals in the third and fourth elements, which occurs for light source positions

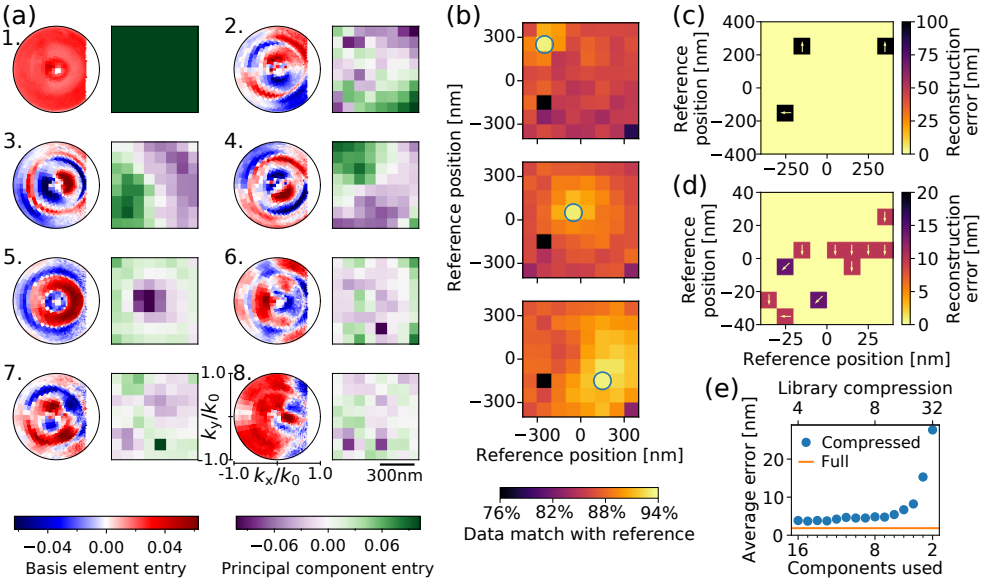

Figure 3.5: Parameter retrieval with an experimental reference library. (a) SVD for an experimental reference dataset, shown as in figure 3.2d. The central plateau of the bullseye antenna is slightly wider than the diagonal of the principal component maps. (b) Comparing new data with the reference library for three positions, indicated by circles. (c) Position estimates for test data based on localisation algorithm versus actual position. Colour scale indicates error between best estimate and known position. Where estimates were incorrect, arrows indicate the direction of the error. Data shown are for a grid with 100 nm steps. (d) Like (c), but 10 nm steps.

off-centre along the appropriate diagonal.

As for the synthetic data, we can compare sample measurements with the library to find position estimates. To this end, we take sample measurements at positions identical to reference positions, within experimental accuracy. Projecting individual measurements onto the reference library reveals a projection match landscape as before. As seen in figure 3.5b, these landscapes typically peak at the correct sample positions, indicated with circles, as in the numerical example before. Comparing best estimates with known positions gives a vectorial localisation error. Figure 3.5c shows a map of localisation error versus position, where colours indicate the magnitude of errors and arrows indicate in which direction the error was made, if any. We see that almost all positions were identified correctly (94% of positions match). To explore position retrieval precision, we repeat calibration, measurement and analysis on an 8×8 grid with much smaller position steps of 10 nm. As seen in figure 3.5d, most positions (81%) are still identified correctly. The average position retrieval error is below 5 nm ($\lambda/100$). Where positions were not retrieved correctly, we see a clear correlation in error directions (southward). This is reminiscent of the behaviour seen in our theoretical demonstration when using a displaced sampling grid (figure 3.3e), suggesting that errors may be dominated by a small systematic drift in bullseye position between measurement of calibration and sample data. Localisation may thus be more accurate than our technical implementation can show.

So far, the full library has been used to estimate light source position. As discussed

previously, most spatial information is contained in those few basis elements with largest principal components. Disregarding the low-weight elements in the optimal basis allows us to compress the library: if N_{used} out of N_{tot} basis elements are used for position retrieval, we reach library compression of a factor $N_{\text{tot}}/N_{\text{used}}$. We explore how this compression affects localisation precision. For the set of measurements on the 10 nm grid, half the optimal basis may be discarded without any loss in localisation performance. Figure 3.5e shows how average error varies as a function of the number of basis elements used. Average error grows slowly as the library is compressed until just a few basis elements are left, as we expected from the large weight of the most important elements. In fact, using just four basis elements, for library compression by a factor 16, average localisation error stays below 10 nm. This means that the calibration data can be stored in a highly efficient way, but also shows how SVD has identified the most vital features of the radiation patterns, speaking for the robustness of the localisation technique.

To investigate the contribution of the nanophotonic structure to the success of the localisation experiment, we compare the previously discussed experimental results with measurements taken on plain gold. Radiation will be emitted even in the absence of surface structuring, with a radiation pattern that is of course expected to be entirely independent of where the electron beam excites the surface. Thus source localisation should be strictly impossible in absence of a nanophotonic scattering structure. In practice, in our setup, captured radiation patterns will vary slightly as the electron beam is scanned around the mirror focus, owing to off-axis aberrations of the parabolic collection mirror. In figure 3.6a, we show the SVD for a dataset for 5×5 electron beam positions in a grid with 200 nm steps on plain gold. In contrast with the data presented in figure 3.5a, there is fairly little spatial structure in either the basis elements or the principal components after the background. What little structure can still be seen in the third and fourth basis elements is likely due to mirror aberrations, due to which some position information can still be extracted. The drastic loss in basis element structure from removal of the antenna indicates that the plain gold radiation patterns do not encode electron beam position in any clear features.

The effect of the nanophotonic structure is seen most clearly in the singular values. In figure 3.6b we compare the plain gold dataset with a dataset taken with the same experimental parameters on a bullseye antenna. The first singular value, reflecting background signal, is identical for the two cases. Subsequent singular values, however, are lower and drop off much more quickly for plain gold than with bullseye antenna. Both sets of singular values eventually tend to the noise level, but the greater number of large singular values indicates the additional position information encoded in the radiation patterns by the nanophotonic structure. At this large step size, it is just barely possible to reconstruct electron beam position on plain gold, in contrast with very reliable reconstruction on the bullseye antenna. What little spatial information remains in the transducer-free experiment may be attributed to aberrations, which could be further reduced by experimental tweaks, but are already minute compared to the wealth of spatial information provided by the bullseye antenna. This shows that scattering by the nanophotonic structure is essential to our technique.

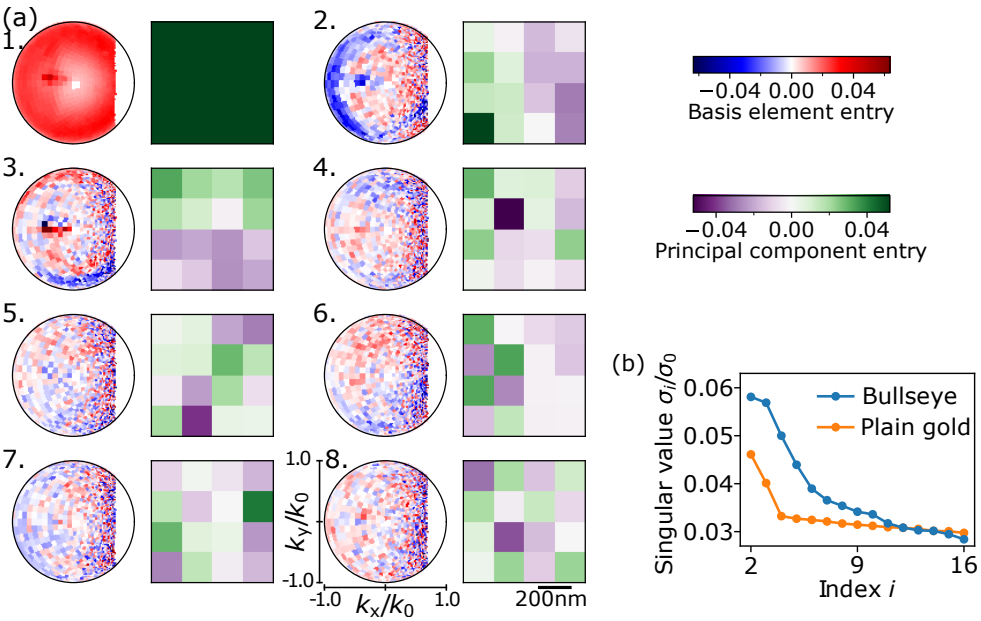

Figure 3.6: Experimental data without nanostructure. (a) SVD of radiation patterns for a grid of electron beam positions on plain gold, shown as in figure 3.2d. (b) Comparing singular values between reference datasets on a nanostructure and on plain gold.

3.4. CONCLUSIONS AND DISCUSSION

We have proposed a library-based approach to extract nanoscale spatial information about structures from far-field radiation patterns, i.e., without the use of a real-space imaging setup. We explored the proposed imaging-free localisation method theoretically, demonstrating that principal component analysis of radiation patterns can produce libraries that efficiently encode nanoscale parameters of scattering systems. In our experimental demonstration, we have shown that the proposed method is able to retrieve light source position relative to a nanophotonic system, in the form of a bullseye antenna, with few-nanometre, $\lambda/100$, precision, deeply below the diffraction limit. These results are achieved at signal-to-noise ratios that are not particularly demanding to reach, comparable with those commonly encountered in, for instance, single molecule microscopy and single nanoparticle darkfield scatterometry. We require a bare minimum of calibration images, one library entry per source position, in contrast with the vast quantities of calibration data used in machine learning-based methods. Localisation is shown to work well over ranges from hundreds to tens of nanometres, with precision possibly limited only by the accuracy and tolerances of the experimental setup. The PCA-based technique provides a number of handles that provide insight into the pattern recognition upon which it operates, particularly direct visualisation of the principal components of calibration data and of the projection match for different reference positions. Our numerical and experimental demonstrations both show smooth optimal basis elements and principal components, implying a degree of robustness of localisation success to experimental drifts and noise.

For our experimental demonstration, comparison between nanophotonically mediated reference data and those generated by a light source on plain gold reveals how localisation is facilitated by the complexity introduced to the radiation patterns by the nanophotonic structure.

Unlike common imaging techniques, our method does not rely on a sharp PSF, but rather uses partial information about the sample to directly invert measured data to a given parameter. This means we cannot define an intrinsic resolution for our method based on PSF width. Though we have shown deeply sub-diffractive localisation precision, this precision will ultimately depend on the interplay between signal-to-noise ratio and the length scale over which measured signals, like radiation patterns, change. It is interesting to consider how the underlying physics may be used to tune this length scale. We know that variations in the size of structures affect radiation patterns through their structure factor, which varies over length scales comparable with the wavelength of the light used. Hybridisation between nanophotonic scatterers, on the other hand, leads to strong changes in spectral response and radiation patterns when scattering sites move at separations of a small fraction of the wavelength. Careful engineering of the interplay between these effects, and so, of the optical modes of the overall structure, may allow future work to tailor transducers for improved localisation range and precision.

We have shown examples of retrieval of light source position from radiation patterns, but we believe the method itself can be applied much more generally. For instance, we expect the same approach to be able to retrieve arbitrary parameters that affect far-field information channels, including orientation and relative scattering strength between sites, spectral properties, and absence or presence of sample features. Initial theoretical results suggest that retrieval of the positions of multiple coherent light sources is feasible; further exploration may be able to quantify these results and extend them to incoherent sources and imaging-like problems. The method also does not necessarily depend on radiation patterns and we believe that parameter retrieval may be performed based on such information channels as scattered optical frequency spectrum or, indeed, based on real-space images, possibly with whatever sort of optical distortion, as in the problems studied in the field of imaging through complex media. Vastly reduced angular information may prove sufficient for parameter retrieval in low-dimensional problems, or conversely, inclusion of phase or polarisation information may allow more precise and more efficient parameter retrieval. For problems where calibration with experimental data is infeasible, the method can be adapted to use synthetic reference data generated by a physical model. The method is specifically intended to be applicable to architectures other than the cathodoluminescence setup used in our experimental demonstration. A carefully characterised collection of structures with randomly deposited luminescent particles may serve as the reference set for retrieval of particle position or orientation on new structures. Another approach is to exploit the analogy between the cathodoluminescence-induced light source, which is like a vertically oriented dipole source, and structures of interest well described by out-of-plane dipole moments. This would allow building a library using cathodoluminescence and using the observed radiation patterns to retrieve the precise position of other vertically oriented emitters. While transition radiation in CL provides information for vertically oriented dipoles only, one can also envision building libraries for in-plane or random dipole orientations using samples with deliberately included emitters at shallow depths (e.g.,

quantum wells, phosphor films). Given the generality of our method across parameters and architectures, we foresee a wide range of applications in nanoscale metrology.

3.5. METHODS

MODEL

Our scattering example system consists of a point source of light moving in a plane $\lambda/4$ below a linear array of four scattering sites spaced $\lambda/4$ apart. The array particles are strong scatterers with a $Q = 10$ resonance around the drive frequency, as might be found for silver nanoparticles around 100 nm in diameter and resonant at visible wavelengths [24]. We use a dipolar drive field oriented along the long axis of the array as a light source. Discrete dipole calculations were made using custom code implementing the Green's function of a dipole and coupling matrix inversion in Python. The SVD algorithm is deterministic and results should be identical between the many available implementations; we use the implementation in the Python NumPy library.

PLASMON ANTENNA

The bullseye antenna was fabricated by removing excess material in Czochralski-grown ⟨111⟩ single-crystalline gold. Focussed ion beam milling was performed in a FEI Helios NanoLab dual SEM/FIB system with a 9.7 pA beam of 30 keV Ga+ ions over 100 rounds with pixel dwell time 10 µs at pixel pitch 7.5 nm.

CATHODOLUMINESCENCE SETUP

Cathodoluminescence measurements were taken in a Thermo Fisher 650 Quanta SEM system and analysed in a Delmic SPARC system. Radiation patterns were generated with a 4 nA electron beam at an energy of 30 keV, collected with an aluminium mirror of acceptance angle 1.47 sr, filtered down to a 40 nm band around $\lambda = 500$ nm and integrated for 30 seconds on a back-illuminated CCD camera. A full set of 8×8 measurements thus took 32 minutes of integration. To limit the effects of sample stage drift, drift correction was performed every second during integration by taking an SEM image of a known region and automatically repositioning based on observed position error. Background correction was performed by subtracting radiation patterns collected with blanked electron beam.

REFERENCES

1. Abbe, E. "Beiträge zur Theorie des Mikroskops und der mikroskopischen Wahrnehmung". *Arch. Mikrosk. Anat.* **9,** 413–468 (1873).
2. Huszka, G. & Gijs, M. A. "Super-resolution optical imaging: A comparison". *Micro-Nano Eng.* **2,** 7–28 (2019).
3. Pujals, S., Feiner-Gracia, N., Delcanale, P., Voets, I. & Albertazzi, L. "Super-resolution microscopy as a powerful tool to study complex synthetic materials". *Nat. Rev. Chem.* **3,** 68–84 (2019).
4. Gåsvik, K. J. *Optical Metrology* (Wiley, 2002).
5. *Handbook of Optical Metrology* (ed Yoshizawa, T.) (CRC Press, 2017).

6. Klar, T. A. & Hell, S. W. “Subdiffraction resolution in far-field fluorescence microscopy”. *Opt. Lett.* **24,** 954 (1999).
7. Betzig, E., Patterson, G. H., Sougrat, R., Lindwasser, O. W., Olenych, S., Bonifacino, J. S., Davidson, M. W., Lippincott-Schwartz, J. & Hess, H. F. “Imaging intracellular fluorescent proteins at nanometer resolution”. *Science* **313,** 1642–1645 (2006).
8. Thorley, J. A., Pike, J. & Rappoport, J. Z. in *Fluorescence Microscopy* 199–212 (Elsevier, 2014).
9. Pohl, D. W., Denk, W. & Lanz, M. “Optical stethoscopy: Image recording with resolution $\lambda/20$”. *Appl. Phys. Lett.* **44,** 651–653 (1984).
10. Taubner, T., Keilmann, F. & Hillenbrand, R. “Nanoscale-resolved subsurface imaging by scattering-type near-field optical microscopy”. *Opt. Express* **13,** 8893 (2005).
11. Lereu, A., Passian, A. & Dumas, P. “Near field optical microscopy: a brief review”. *Int. J. Nanotechnol.* **9,** 488 (2012).
12. Kolenov, D. & Pereira, S. F. “Machine learning techniques applied for the detection of nanoparticles on surfaces using coherent Fourier scatterometry”. *Opt. Express* **28,** 19163 (2020).
13. Bouchet, D., Carminati, R. & Mosk, A. P. “Influence of the local scattering environment on the localization precision of single particles”. *Phys. Rev. Lett.* **124,** 133903 (2020).
14. Neugebauer, M., Woźniak, P., Bag, A., Leuchs, G. & Banzer, P. “Polarization-controlled directional scattering for nanoscopic position sensing”. *Nature Commun.* **7,** 11286 (2016).
15. Shang, W., Xiao, F., Zhu, W., Han, L., Premaratne, M., Mei, T. & Zhao, J. “Unidirectional scattering exploited transverse displacement sensor with tunable measuring range”. *Opt. Express* **27,** 4944 (2019).
16. Bag, A., Neugebauer, M., Mick, U., Christiansen, S., Schulz, S. A. & Banzer, P. “Towards fully integrated photonic displacement sensors”. *Nat. Commun.* **11,** 2915 (2020).
17. Rochon, P. & Bissonnette, D. “Lensless imaging due to back-scattering”. *Nature* **348,** 708–710 (1990).
18. Zhang, T., Godavarthi, C., Chaumet, P. C., Maire, G., Giovannini, H., Talneau, A., Allain, M., Belkebir, K. & Sentenac, A. “Far-field diffraction microscopy at $\lambda/10$ resolution”. *Optica* **3,** 609 (2016).
19. Unger, K. D., Chaumet, P. C., Maire, G., Sentenac, A. & Belkebir, K. “Versatile inversion tool for phaseless optical diffraction tomography”. *J. Opt. Soc. Am. A* **36,** C1 (2019).
20. Vellekoop, I. M. & Mosk, A. P. “Focusing coherent light through opaque strongly scattering media”. *Opt. Lett.* **32,** 2309 (2007).
21. Harm, W., Roider, C., Jesacher, A., Bernet, S. & Ritsch-Marte, M. “Lensless imaging through thin diffusive media”. *Opt. Express* **22,** 22146 (2014).
22. Horisaki, R., Okamoto, Y. & Tanida, J. “Single-shot noninvasive three-dimensional imaging through scattering media”. *Opt. Lett.* **44,** 4032 (2019).

23. Kim, D. & Englund, D. R. "Quantum reference beacon–guided superresolution optical focusing in complex media". *Science* **363,** 528–531 (2019).

24. Link, S. & El-Sayed, M. A. "Size and temperature dependence of the plasmon absorption of colloidal gold nanoparticles". *J. Phys. Chem. B* **103,** 4212–4217 (1999).

25. Zhao, L., Kelly, K. L. & Schatz, G. C. "The extinction spectra of silver nanoparticle arrays: influence of array structure on plasmon resonance wavelength and width". *J. Phys. Chem. B* **107,** 7343–7350 (2003).

26. Weber, W. H. & Ford, G. W. "Propagation of optical excitations by dipolar interactions in metal nanoparticle chains". *Phys. Rev. B* **70,** 125429 (2004).

27. Yurkin, M. & Hoekstra, A. "The discrete dipole approximation: An overview and recent developments". *J. Quant. Spectrosc. Radiat. Transfer* **106,** 558–589 (2007).

28. Chaumet, P. C., Zhang, T. & Sentenac, A. "Fast far-field calculation in the discrete dipole approximation". *J. Quant. Spectrosc. Radiat. Transfer* **165,** 88–92 (2015).

29. Novotny, L. & Hecht, B. *Principles of Nano-Optics* (Cambridge University Press, 2006).

30. García de Abajo, F. J. "Colloquium: Light scattering by particle and hole arrays". *Rev. Mod. Phys.* **79,** 1267–1290 (2007).

31. Lieb, M. A., Zavislan, J. M. & Novotny, L. "Single-molecule orientations determined by direct emission pattern imaging". *J. Opt. Soc. Am. B* **21,** 1210 (2004).

32. Patra, D., Gregor, I., Enderlein, J. & Sauer, M. "Defocused imaging of quantum-dot angular distribution of radiation". *Appl. Phys. Lett.* **87,** 101103 (2005).

33. Osorio, C. I., Mohtashami, A. & Koenderink, A. F. "K-space polarimetry of bullseye plasmon antennas". *Sci. Rep.* **5,** 9966 (2015).

34. Jolliffe, I. T. & Cadima, J. "Principal component analysis: a review and recent developments". *Philos. Trans. R. Soc., A* **374,** 20150202 (2016).

35. Jesse, S. & Kalinin, S. V. "Principal component and spatial correlation analysis of spectroscopic-imaging data in scanning probe microscopy". *Nanotechnology* **20,** 085714 (2009).

36. Melati, D., Grinberg, Y., Dezfouli, M. K., Janz, S., Cheben, P., Schmid, J. H., Sánchez-Postigo, A. & Xu, D.-X. "Mapping the global design space of nanophotonic components using machine learning pattern recognition". *Nature Commun.* **10,** 4775 (2019).

37. Jolliffe, I. T. *Principal Component Analysis* (Springer-Verlag, 2002).

38. Koenderink, A. F. "Plasmon nanoparticle array waveguides for single photon and single plasmon sources". *Nano Lett.* **9,** 4228–4233 (2009).

39. Li, J., Salandrino, A. & Engheta, N. "Shaping light beams in the nanometer scale: A Yagi-Uda nanoantenna in the optical domain". *Phys. Rev. B* **76,** 245403 (2007).

40. Coenen, T., Vesseur, E. J. R., Polman, A. & Koenderink, A. F. "Directional emission from plasmonic Yagi–Uda antennas probed by angle-resolved cathodoluminescence spectroscopy". *Nano Lett.* **11,** 3779–3784 (2011).

41. Pu, T., Ou, J. Y., Papasimakis, N. & Zheludev, N. I. "Label-free deeply subwavelength optical microscopy". *Appl. Phys. Lett.* **116,** 131105 (2020).

42. Ghosh, A., Roth, D. J., Nicholls, L. H., Wardley, W. P., Zayats, A. & Podolskiy, V. A. "Machine learning-based diffractive imaging with subwavelength resolution". in *Conference on Lasers and Electro-Optics* (OSA, 2020).

43. Baum, E. B. & Haussler, D. "What size net gives valid generalization?" *Neural Computation* **1,** 151–160 (1989).

44. Goodfellow, I., Bengio, Y. & Courville, A. *Deep Learning* `http://www.deeplearningbook.org` (MIT Press, 2016).

45. Yamamoto, N., Araya, K., Toda, A. & Sugiyama, H. "Light emission from surfaces, thin films and particles induced by high-energy electron beam". *Surf. Interface Anal.* **31,** 79–86 (2001).

46. Van Wijngaarden, J. T., Verhagen, E., Polman, A., Ross, C. E., Lezec, H. J. & Atwater, H. A. "Direct imaging of propagation and damping of near-resonance surface plasmon polaritons using cathodoluminescence spectroscopy". *Appl. Phys. Lett.* **88,** 221111 (2006).

47. García de Abajo, F. J. "Optical excitations in electron microscopy". *Rev. Mod. Phys.* **82,** 209–275 (2010).

48. Kuttge, M., Vesseur, E. J. R., Koenderink, A. F., Lezec, H. J., Atwater, H. A., de Abajo, F. J. G. & Polman, A. "Local density of states, spectrum, and far-field interference of surface plasmon polaritons probed by cathodoluminescence". *Physical Review B* **79,** 113405 (2009).

49. Coenen, T., Vesseur, E. J. R. & Polman, A. "Angle-resolved cathodoluminescence spectroscopy". *Appl. Phys. Lett.* **99,** 143103 (2011).

50. Osorio, C. I., Coenen, T., Brenny, B. J. M., Polman, A. & Koenderink, A. F. "Angle-resolved cathodoluminescence imaging polarimetry". *ACS Photonics* **3,** 147–154 (2015).

51. Martín-Moreno, L., García-Vidal, F. J., Lezec, H. J., Degiron, A. & Ebbesen, T. W. "Theory of highly directional emission from a single subwavelength aperture surrounded by surface corrugations". *Phys. Rev. Lett.* **90,** 167401 (2003).

52. Lezec, H. J. "Beaming light from a subwavelength aperture". *Science* **297,** 820–822 (2002).

53. Aouani, H., Mahboub, O., Bonod, N., Devaux, E., Popov, E., Rigneault, H., Ebbesen, T. W. & Wenger, J. "Bright unidirectional fluorescence emission of molecules in a nanoaperture with plasmonic corrugations". *Nano Lett.* **11,** 637–644 (2011).

54. Gorodetski, Y., Lombard, E., Drezet, A., Genet, C. & Ebbesen, T. W. "A perfect plasmonic quarter-wave plate". *Appl. Phys. Lett.* **101,** 201103 (2012).

55. Crick, C. R., Albella, P., Ng, B., Ivanov, A. P., Roschuk, T., Cecchini, M. P., Bresme, F., Maier, S. A. & Edel, J. B. "Precise attoliter temperature control of nanopore sensors using a nanoplasmonic bullseye". *Nano Lett.* **15,** 553–559 (2014).

56. Coenen, T. & Polman, A. “Energy-momentum cathodoluminescence imaging of anisotropic directionality in elliptical aluminum plasmonic bullseye antennas”. *ACS Photonics* **6,** 573–580 (2018).

4

LOCALISING NANOSCALE OBJECTS USING NANOPHOTONIC NEAR-FIELD TRANSDUCERS

We study how nanophotonic structures can be used for determining the position of a nearby nanoscale object with subwavelength accuracy. Through perturbing the near-field environment of a metasurface transducer consisting of nano-apertures in a metallic film, the location of the nanoscale object is transduced into the transducer far-field optical response. By monitoring the scattering pattern of the nanophotonic near-field transducer and comparing it to measured reference data, we demonstrate two-dimensional localisation of the object accurate to $24\,\mathrm{nm}$ *across an area of* $2 \times 2\mu\mathrm{m}^2$*. We find that adding complexity to the nanophotonic transducer allows localisation over a larger area while maintaining resolution, as it enables encoding more information on the position of the object in the transducer far-field response.*

The work described in this chapter has been published separately as *Nanophotonics* **10**, 1723-1732 (2021)

4.1. INTRODUCTION

Nanoscale metrology is imperative for advances in nanoscience, biology, and semiconductor technology. As many structural features of interest are smaller than the optical diffraction limit, they are not resolved through direct imaging with a conventional microscope. In fluorescence imaging, multiple super-resolution techniques have been developed, such as photo-activated localisation microscopy and stimulated emission depletion microscopy, that allow imaging of smaller features by relying on careful fitting or engineering of a point spread function [1, 2]. An alternative approach to construct images with subwavelength resolution is by detecting the evanescent optical fields close to the sample that contain high-frequency spatial information. In near-field scanning optical microscopy, a nanoscale probe is brought into close proximity of the sample surface, enabling coupling to the optical near field and access to high-resolution information [3, 4]. A drawback of such scanning microscopy techniques are the relatively long acquisition times that are needed for physical translation of the probe to perform raster scanning. Therefore, development of near-field techniques that do not rely on physical scanning, enabling rapid nanoscale-resolution sensing and imaging, would be of great benefit to nanoscale metrology.

Scattering-type near-field scanning optical microscopy (s-NSOM) [5, 6] maps the optical near field of a sample by moving a nanoscale scatterer through it and collecting scattered light. The intensity of the scattered signal as a function of position, usually measured on a bucket detector with a single degree of freedom, gives information on the permittivity distribution of the sample [7] or on the optical near field supported by the sample. In this chapter, conversely, we aim to construct an optical near-field transducer in the form of a nanophotonic target structure that determines the position of a nanoscale perturbation located near the structure on basis of collected scattered light. The 'sample' in s-NSOM terms becomes in our work a transducer that encodes the location of a scatterer — the known tip in s-NSOM, but here the unknown variable under study — into a far-field optical response. Our approach to retrieving the scatterer position purely from optical fields is to not use a bucket detector for total scatterered intensity, but instead to exploit the many degrees of freedom, including wavevector, polarisation, and wavelength, that can be detected in the scattered signal [8, 9]. Those many degrees of freedom in the scattered far-field potentially encode detailed subwavelength information on the location of the scatterer near the transducer [10]. So unlike s-NSOM, where spatial information is obtained from consecutive measurements while raster-scanning a detecting element, here we exploit the complexity and connection of near and far fields to obtain spatial information from a single measurement. Indeed, methods based on far-field scattering signals have been developed to localise a single scatterer in a carefully tailored illumination beam with subwavelength resolution [11–15]. In such a framework, one would expect the sensitivity, resolution and field of view to be controllable by design of the complex nanophotonic scattering structures in terms of geometry and mode structure, as shown in figure 4.1. While in this chapter we focus on sensing the location of a single scatterer, one could ultimately imagine a combination of multiplexed readouts of multiple degrees of freedom in the scattered field with optimised metasurface near-field transducers to obtain rapid nanoscale sensing and potentially even imaging without physical movement of the transducer.

In this chapter, we demonstrate a nanophotonic near-field transducer for detecting the

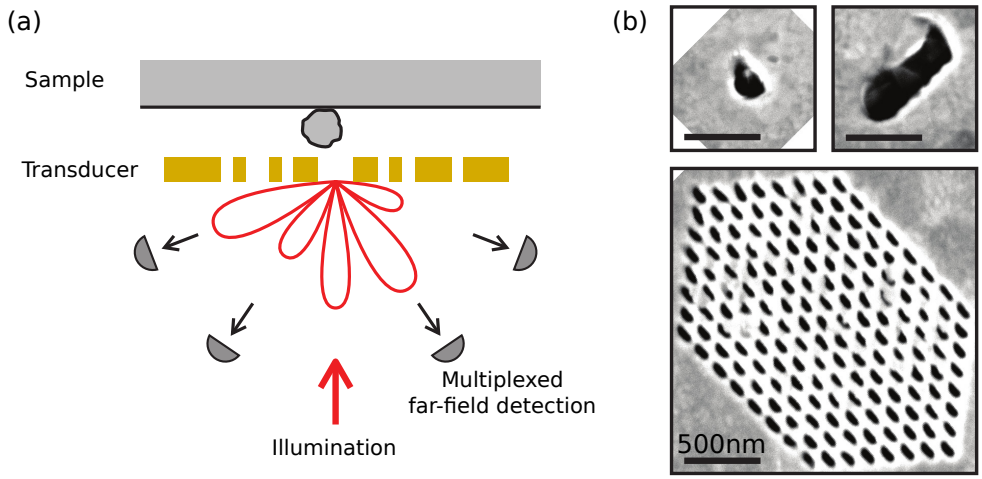

Figure 4.1: (a) A complex nanophotonic structure scatters incident light into many degrees of freedom in the far field. These contain rich subwavelength information on a sample positioned in the near field of the structure, which functions as a near-field transducer. A multiplexed readout of these degrees of freedom may enable rapid nanoscale sensing without translation of the transducer. (b) SEM images of the near-field transducers used in this chapter, which consist of one or more apertures in a gold film.

position of a subwavelength object based on angle-resolved far-field scattering patterns, as a first step towards rapid nanoscale sensing. To this end, we experimentally investigate the dependence of the angle-resolved optical signal scattered from the transducer and containing many degrees of freedom, on the position of a nanoscale object in its near field. The near-field transducer consists of one or more apertures in a gold film (see figure 4.1b), which upon excitation provides high optical near fields in the direct vicinity of the apertures. The transducer is illuminated from the far field, while reflected light is collected to image its far-field scattering pattern. Introduction of a nanoscale object will influence the near-field environment of the transducer as it alters the permittivity distribution, resulting in changes in the radiation pattern. The way in which the radiation pattern is modified depends on the position of the object. Therefore, monitoring the far-field radiation pattern of the transducer enables retrieval of the position of the object, provided that the patterns are uniquely different for each position. To experimentally verify this technique, we first build a library of radiation patterns, placing a nanoscale object at a grid of positions near a near-field transducer and recording the radiation pattern for each object position. Next, we reconstruct the object position with subwavelength resolution solely from a measured far-field radiation pattern using a library-based approach exploiting singular value decomposition (chapter 3). We show that our technique greatly benefits from employing more complex nanostructures as near-field transducers, which enables accurate retrieval of the object position across the entire transducer area.

4.2. EXPERIMENTAL METHOD

We consider the experimental system sketched in figure 4.2a. We measure the far-field radiation pattern of a near-field transducer, consisting of one or more nanoapertures in a metal film on a glass coverslip, and monitor how it changes when a nanoscale object is moved through its near field. The experimental setup is shown in figure 4.2b. Light from a supercontinuum white light laser (Fianium WhiteLase Micro), spectrally filtered to cover a wavelength range of 500 – 750 nm, is transmitted through a linear polariser and focussed to a diffraction-limited spot on the transducer using a microscope objective (60×, NA = 0.95, Nikon CFI Plan Apochromat Lambda). Reflected light is collected through the same objective, transmitted through a second linear polariser, and detected on a camera (Basler acA1920-um), which images the back focal plane of the objective. To suppress spurious signals from the substrate, the polarisation component orthogonal to the incident polarisation is detected. Light scattered by the transducer can experience polarisation conversion, while direct reflections of the substrate are expected to maintain the incident polarisation. To test our near-field transducer, a small perturbation is required that we can place at a controlled position in the near field of the transducer. This role is played by a tapered optical fibre (tip radius 50 nm) [16]. The fibre is positioned at a height of approximately 10 nm above the transducer using shear-force feedback [17] and can be scanned transversally using closed-loop piezo actuators with strain gauges for position read out. We emphasise that the setup is in terms of components identical to a near-field scanning probe mounted on an inverted microscope, but with the unconventional addition of Fourier imaging. However, where the sharp fibre tip is usually viewed as the sensor that detects optical information, here the viewpoint is reversed. The fibre tip is the object to be detected and localised, while the nanoaperture pattern is the transducer.

The near-field transducers consist of one or more apertures milled in gold. They are fabricated by first depositing a 150 nm gold film on a glass substrate using thermal evaporation. Subsequently, focussed ion beam milling using 30 keV Ga ions (1.5 pA, dwell time 2 µs, pixel pitch 5 nm) is used to mill the apertures. The use of apertures in an opaque layer eliminates direct scattering of the illumination beam from the object; any observed interaction between the object and the light is mediated by the transducer. Figure 4.2c shows a schematic of a transducer containing a single slot aperture of $110 \times 50\,\mathrm{nm}^2$. The incident light is vertically polarised, while the aperture is oriented at 45°, allowing for excitation of modes polarised along either axis of the aperture, to obtain polarisation conversion required for cross-polarised detection. A typical measured cross-polarised radiation pattern of a single aperture is shown in figure 4.2d. As is common in back-focal-plane microscopy, the raw camera image reports radiation patterns as function of normalised parallel momentum $(k_x, k_y)/k_0$ of the radiated light where k_0 is the wave number in vacuum. Due to the cross-polarised detection, a four-lobe pattern appears at large angle (NAs from circa 0.85 to 0.95). In the experiments, the object is raster scanned across the transducer while its radiation pattern is captured at each position.

4.3. LOCALISATION STRATEGY

To demonstrate high-resolution localisation of the object we develop a strategy with two main ingredients. The first is that we determine object locations by comparing measured

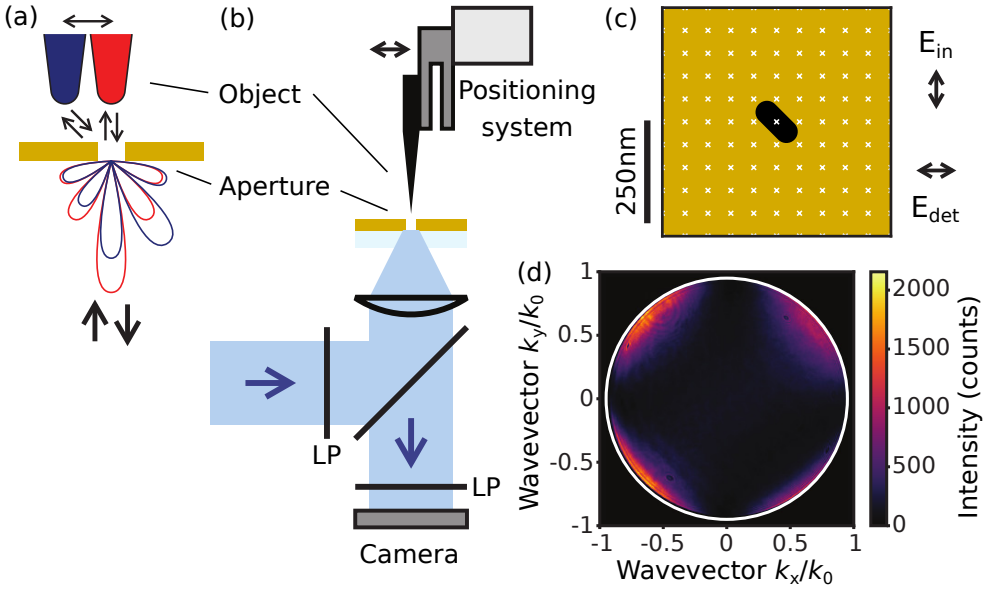

Figure 4.2: Experimental setup. (a) Minute changes in the near-field environment of an aperture influence its far-field radiation pattern. Monitoring the aperture's radiation pattern enables retrieval of the position of a nanoscale object. (b) Linearly polarised light is focussed on the aperture using a microscope objective. Reflected light is collected through the same objective, filtered using a linear polariser (LP), and the cross-polarised signal is detected on a camera, which is imaging the back focal plane of the objective. A tapered optical fibre, positioned in the near field of the aperture using shear-force feedback, acts as the object. (c) Schematic of a near-field transducer containing a single aperture of $110 \times 50\,\mathrm{nm}^2$. The incident light is vertically polarised. The object is scanned across the aperture following a raster grid (white marks). (d) Measured cross-polarised radiation pattern of the aperture.

radiation patterns against a prerecorded library. Data collection thus has two stages: first to record the library, and subsequently to take the test data. The second main ingredient is that we use a highly efficient representation of the library of radiation patterns to facilitate the comparison between test and library data. This representation of the measured radiation patterns uses singular value decomposition, as previously used to localise a point source of light (chapter 3). We note that, alternatively, the comparison between test and library data could be a task suitable to address with machine learning, provided that the library data set is sufficiently large — typically orders of magnitude larger than the number of parameter values to be distinguished.

We collect the library data in a matrix M that contains each of the normalised radiation patterns, one per object position, as a single row. Through a singular value decomposition, we decompose this matrix into $M = U\Sigma V^\dagger$, with U, V unitary matrices and Σ a diagonal matrix. Here, U forms a basis for object position and V for the radiation pattern. The entries of Σ, the singular values σ_i, reflect the importance of each component in describing the data set M and are sorted in order of decreasing magnitude. In our experiment, each column of V, called the principal component direction, represents a vector (basis element) of the orthogonal basis for the representation of the radiation patterns generated by the

structure, for different positions of the object. In other terms, all possible radiation patterns can be represented as a superposition of these elements. Each column of U provides the projection of the corresponding basis element on the total scattering pattern per object position. In other words, it provides a coefficient that, multiplied with the corresponding singular value, expresses the contribution of the basis element in the total scattering pattern for each position, known as the principal component. To directly reflect the importance of a radiation pattern basis element at each position, we treat $U\Sigma$ as a single entity.

Once we have efficiently summarised the library of radiation patterns by singular value decomposition, we explore retrieval of object positions from radiation patterns taken in a second measurement run. We use the previously acquired library data set as a reference and project the new measurements onto the radiation pattern basis V of the reference data. Next, we calculate the match of newly acquired data A at positions i with the reference data at positions j, which we define as $1 - \left\| (U\Sigma)_j - A_i V \right\| / \sqrt{2}$. A high match indicates high similarity between radiation patterns (as discussed in chapter 3). To obtain an estimate for the object position based on the measured radiation patterns, we take the reference position that is associated with the highest match as the retrieved position. Comparing this with the actual position of the object, known from the calibrated reading of the position of the piezo actuators that control the probe, allows for defining a reconstruction error as the distance between the actual and retrieved positions.

4.4. RESULTS

First we investigate the dependence of the radiation pattern on the object position for a transducer consisting of a single aperture in figure 4.3. Figures 4.3b and 4.3c show the measurement results of 21×21 probe points covering an area of $1 \times 1\,\mu m^2$ in 50 nm steps, for a small aperture of $250 \times 110\,nm^2$, of which a SEM image and shear-force topography scan are shown in figure 4.3a. The measured dependence of the cross-polarised radiation pattern of the aperture on the object position is presented in figure 4.3b in the form of a singular value decomposition. Shown in the figure are the first eight principal component directions V, columns of the radiation pattern basis, and matching principal components $U\Sigma$, describing the importance of the radiation pattern basis element at each object position. To reconstruct the radiation pattern for a specific object position, one considers, for each component, the vector of the radiation pattern basis V (left), multiplies this pattern by the corresponding value of $U\Sigma$ (right), and finally sums over all components. The first, most important, component of the data set shows little position dependence, and its radiation pattern closely resembles figure 4.2d. This component corresponds to the common denominator shared by all measured radiation patterns. It consists of four lobes of high intensity at far off-normal angles, resulting from polarisation conversion in the direct reflection of the gold surface. Furthermore, a region of non-zero intensity is visible at near-normal angles in the centre, corresponding to light reflected from the aperture. A strong position dependence is visible for the next two components. The second and third components share two similar features in their position dependence: a high signal centred on the aperture and a gradient across the entire scan area. Let us first consider the feature centred on the aperture, for either of these two components. Comparing positions near the aperture to positions at larger distance shows that $U\Sigma$ negatively peaks at the aperture, which means that the corresponding radiation pattern element V is mainly of

importance for positions near the aperture, and with a negative sign. Taking the negative sign into account, this radiation pattern element shows a negative contribution to the intensity at near-normal angles in the centre and positive at high angles. As every measured radiation pattern has been normalised individually, these relative contributions actually correspond to a decrease in absolute intensity at low angles, while leaving the signal at high angles unaffected. Thus, the second and third components reveal that when the object is positioned near the aperture, less light is reflected back at low angles. This can be explained by interaction with the object introducing an extra loss channel. The gradients in $U\Sigma$ are the result of a slight drift in aperture position relative to the microscope during the experiment, which is also observed in measurements without any nearby object. To remove major continuous drifts of this kind, we fit a two-dimensional plane to $U\Sigma$ for each of the first three components and subtract their effect from the data before further analysis. We note that any instability in the aperture and object positions will also negatively influence the match of data between subsequent measurement runs. Further components also exhibit structure in position dependence across the scan area. However, their magnitude is much lower, indicating that they are of less importance in describing the measured radiation patterns.

We now turn to matching the newly acquired test data set A with the reference data (figure 4.3c). Each of the images in the 21×21 grid shows the match of the radiation pattern at this specific object position with all positions of the reference data set. Three positions are highlighted for which a zoom is provided. One can recognise that the measurement with the object centred on the aperture (left) matches best with the same position from the reference data, and poorly for all positions far away from the aperture. For an off-centre object position (middle), the measurement matches well with most measurements taken at similar distance from the aperture, visible as a bright circle in the image, but neither with the aperture (dark colour, strong mismatch), nor with radiation patterns further out. Finally, for object locations far from the aperture (right), the radiation pattern matching essentially reports that the object is surely not at the aperture, without further specific information on distance to the aperture centre. The observation that, in the vicinity of the aperture, the radiation pattern mainly depends on just the radial distance from the object to the aperture matches with the sharply peaked feature centred at the aperture that is visible in the most important components of figure 4.3b, and can be explained by considering the small, subwavelength, aperture acting as a single-mode filter. This subwavelength aperture has dimensions small enough such that its transmission is dominated by a single evanescent spatial mode [18], of which we measure the far-field radiation pattern. Information about near-field perturbations of the environment that is scattered to the far field on the other side of the aperture has to be mediated via this single mode, resulting in a single degree of freedom for detection. The far-field intensity radiated in this single mode reflects the strength of the perturbation, which due to the almost circular symmetry of the aperture translates to the distance from the object to the aperture.

Therefore, we investigate if an aperture of larger size, that can support multiple modes, shows more components with a stronger dependence on object position. Figures 4.3(e-f) show the principal components of the library data set for a large aperture of $690 \times 200\,\mathrm{nm}^2$. Its geometry is shown in figure 4.3d. The singular value decomposition of the measured object position dependence of the radiation pattern is depicted in figure 4.3e. Similar to the

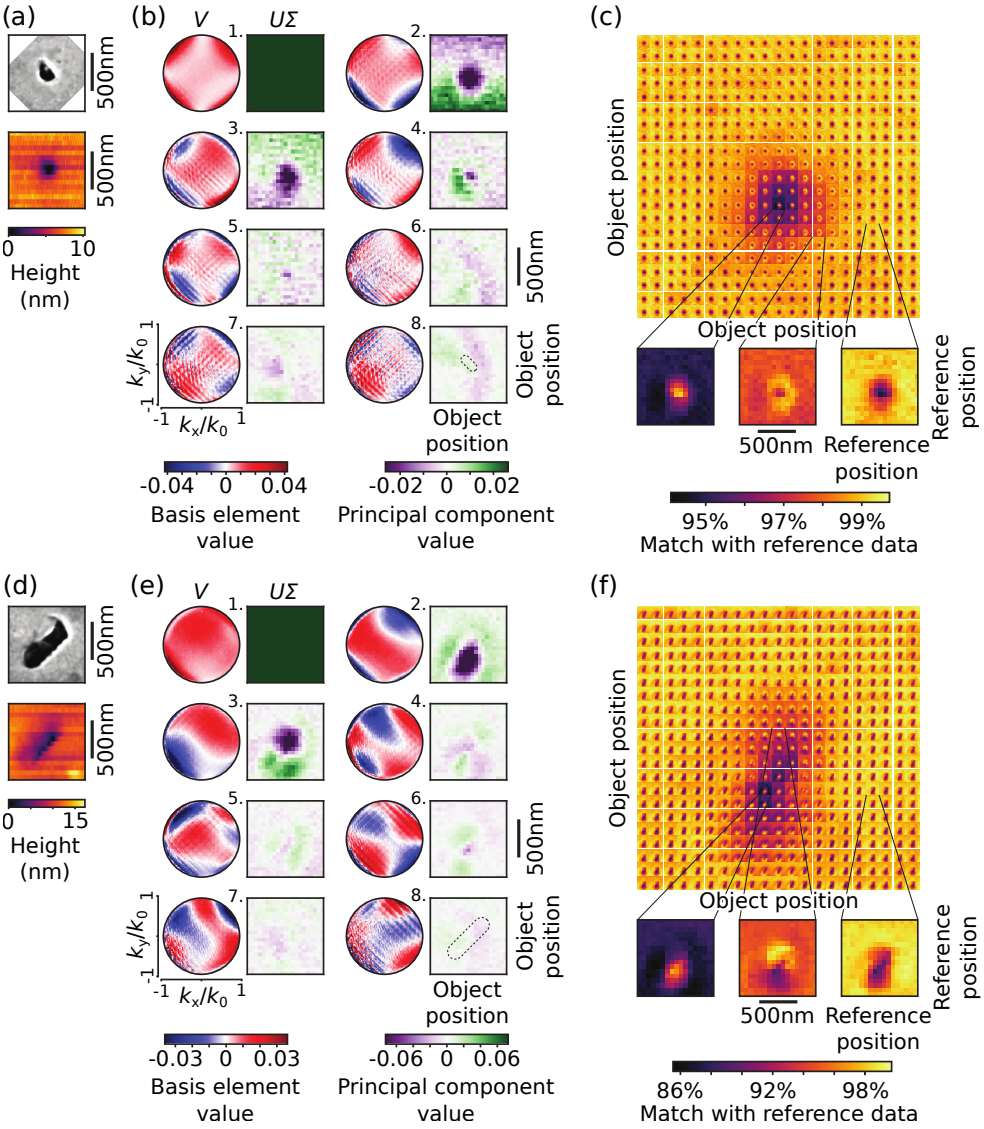

Figure 4.3: Measured dependence of the radiation pattern on the object position for a (a-c) small aperture and (d-f) large aperture. (a, d) SEM image (top) and shear-force topography scan (bottom) of the transducer. (b, e) Singular value decomposition of a set of reference data for 21×21 probe points covering an area of $1 \times 1\,\mu m^2$ in 50 nm steps. Shown are the first eight principal component directions V (blue-red), forming a radiation pattern basis, and matching principal components $U\Sigma$ (purple-green), representing the importance at each object position. (c, f) Match of signal data with reference data. Each of the images in the 21×21 grid shows the match of a newly acquired radiation pattern at this position with all positions of the reference data set. Three positions are highlighted below.

small aperture, there is a strong component that corresponds to the presence of the object near the aperture, leading to less reflected light at low angles, now visible in the second component. Here, its spatial extent is larger, and elongated, matching the larger size of the aperture. Additionally, the vertical position of the object is encoded in a strong third component, redistributing intensity diagonally in the radiation pattern. This agrees with a picture of the large aperture supporting multiple modes, interacting either resonantly or below cutoff, as expected for elongated apertures [18]. The position dependence of further components is reminiscent of higher-order modes at the aperture, but care must be taken in drawing conclusions about their exact shape as there is no guarantee for the singular value decomposition to reveal features directly matching the physical modes of the aperture.

Shown in figure 4.3f is the matching of subsequently recorded test data with the previously acquired reference data set for the large aperture. Similar to the small aperture, the general trend is that measurements match well with reference data taken with the object at the same distance from the aperture. The geometry of the aperture, elongated along the diagonal, is apparent in the centre of the scan area, for instance as the region over which data taken with the object at the aperture (left) matches well to the reference data has an elliptical shape. Interestingly, measurements with the object just above the aperture (middle) now match well with those positions, but worse with positions below the aperture. This is a result of the third principal component in figure 4.3e which encodes the vertical object position, and which was not as important in the principal components of the smaller aperture radiation patterns.

Comparing the reference position with the highest match to the actual object position gives the error in reconstructing the position, which is shown in figure 4.4. Figure 4.4a displays the reconstruction error versus actual object position for a measurement on the small aperture covering an area of $2 \times 2\,\mu m^2$ in 100 nm steps. Arrows indicate the direction in which the error is made. The figure shows that it is possible to accurately retrieve the object position from its radiation pattern for positions within an area of approximately 0.5 µm in diameter around the aperture. At positions further away from the aperture, the typical reconstruction error increases, since the measured radiation patterns depend less strongly on position. Nonetheless, the span over which retrieval is correct is not limited to a single point at the aperture position, nor to the aperture size, but to an area of size that is set by λ, over which the near field has intricate spatial features. Zooming in on this central area in a new set of measurements, Figure 4.4b shows the results of a set of measurements across an area of $0.25 \times 0.25\,\mu m^2$ in steps of 25 nm, centred on the aperture. Here, the average reconstruction error is 32 nm ($\approx \lambda/22$).

For the larger aperture, reconstruction errors are displayed in figures 4.4c and 4.4d. We find similar behaviour to the small aperture. However, the area around the aperture where the object position is correctly retrieved is increased in size and the average reconstruction error at the aperture has decreased. This is attributed to the multimode nature intrinsic to the increased aperture size and the resulting additional strong position-dependent components in the radiation patterns.

Finally, in an approach to increase the field of view, i.e., the area of successful retrieval of the object position, we consider a two-dimensional array of slot apertures as transducer, as shown in figure 4.5a. The apertures, each of size $110 \times 50\,nm^2$, are arranged in a centred

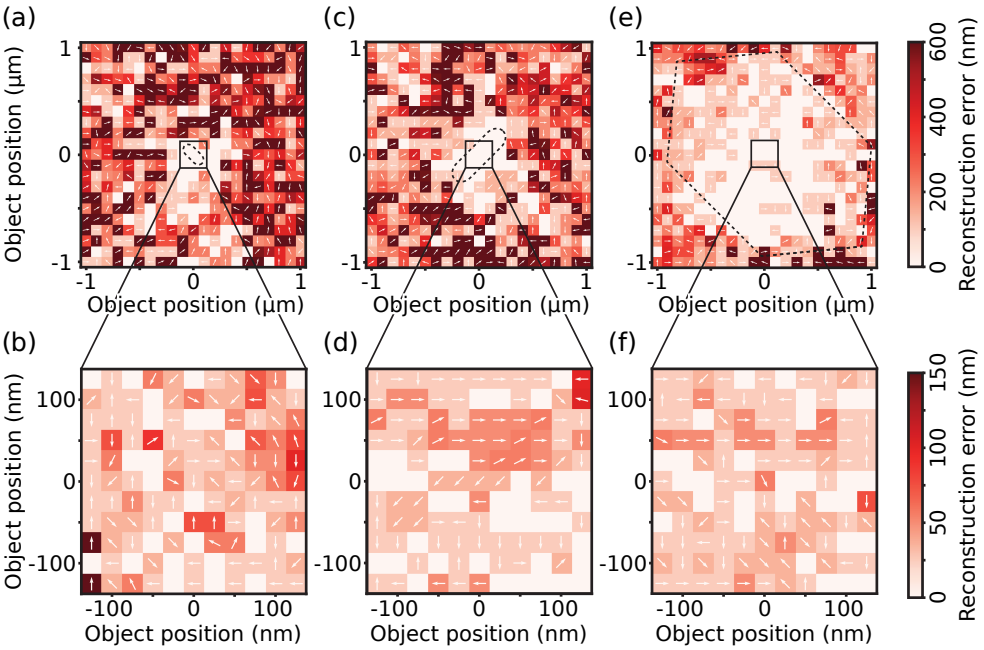

Figure 4.4: Position estimates for signal data retrieved by the localisation algorithm versus actual position for a (a, b) small aperture, (c, d) large aperture, (e, f) and two-dimensional aperture array. The colour scale shows the error between the reconstructed position and the known position. For incorrect estimates, arrows indicate the direction of the error. The reconstruction error is measured across an area of (a, c, e) $2 \times 2\,\mu m^2$ in 100 nm steps, and (b, d, f) $0.25 \times 0.25\,\mu m^2$ in 25 nm steps. In (a, c, e), the outline of the transducer is indicated (dashed).

rectangular lattice of pitch 160 nm by 200 nm. Such a structure naturally supports many more modes than a single aperture and could exhibit a highly intricate spatial near-field distribution through multiple scattering of plasmon waves mediating coupling between the apertures. The diffraction-limited illumination spot is centred on the array and has a width of approximately 900 nm that is smaller than the size of the array. Figure 4.5b displays the singular value distribution of the dependence of the radiation pattern on the object position for a measurement covering an area of $2 \times 2\,\mu m^2$ in 100 nm steps. Multiple components show strong position-dependent features, not only near the illumination spot but extending across the entire array. This intricate position dependence of the radiation pattern may enable successful reconstruction of the object position across a large area.

Figure 4.5c shows the match between radiation patterns in the subsequent test data acquisition run against the reference measurements. For positions around the centre of the scan area (magnified panels), it is clear that the point of best matching moves in step with object position across the array. This demonstrates that the position of the object with respect to the aperture array is encoded in the radiation pattern. Comparing the position of highest match with the actual object position gives the reconstruction error, which is shown in figure 4.4e. The object position is accurately retrieved across a large part of the aperture array, covering an area of approximately $2 \times 2\,\mu m^2$. At positions away from the array, the reconstruction error increases. Figure 4.4f shows the reconstruction

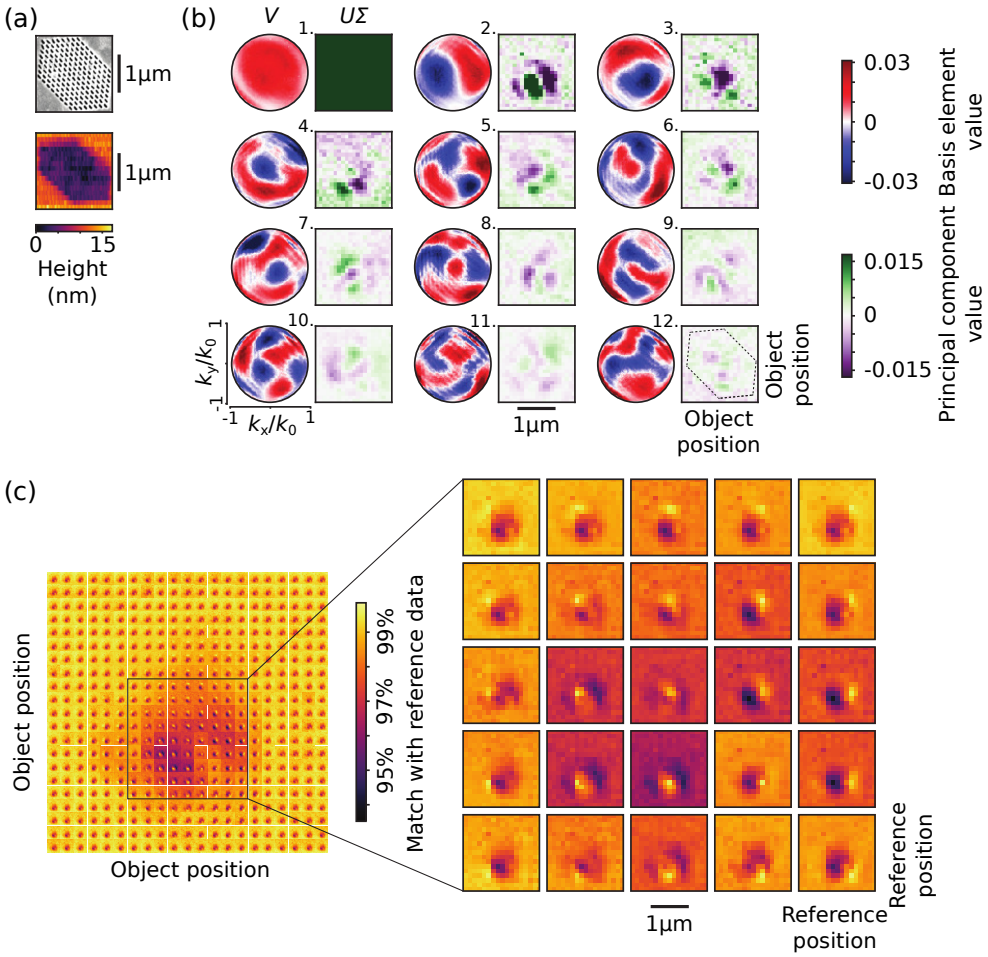

Figure 4.5: Measured dependence of the radiation pattern on the object position for a two-dimensional aperture array. (a) SEM image (top) and shear-force topography scan (bottom) of the transducer. (b) Singular value decomposition of a set of reference data for 21×21 probe points covering an area of $2 \times 2\,\mathrm{nm}^2$ in 100 nm steps. Shown are the first twelve principal component directions V (blue-red), forming a radiation pattern basis, and matching principal components $U\Sigma$ (purple-green), representing the importance at each object position. (c) Match of signal data with reference data. Each of the images in the 21×21 grid shows the match of a newly acquired radiation pattern at this position with all positions of the reference data set. Some positions are highlighted to the right.

error for a measurement area of $0.25 \times 0.25\,\mu\mathrm{m}^2$ in steps of 25 nm, centred on the array. Here, the average reconstruction error is 24 nm ($\approx \lambda/29$). Similar reconstruction errors are observed at off-centre object positions on the array. This shows that using extended complex nanostructures as a near-field transducer enables accurate retrieval of the object position across an area covering almost the entire transducer.

4.5. CONCLUSION

In summary, we have constructed a nanophotonic near-field transducer for detecting the position of a subwavelength object, which is encoded in the far-field radiation pattern of the transducer. By monitoring the radiation pattern and using a library-based technique, we demonstrated retrieval of the object position accurate to 24 nm across an area of $2 \times 2 \mu m^2$. We find that introducing more complexity to the nanophotonic transducer allows for encoding of more information about the object position in its rich far-field scattering signal.

An excellent question would be what limits the precision and the field of view of successful position retrieval, and how to enhance these. Ultimately, the localisation precision will rely on differences between radiation patterns, which contain a component that is modified due to the presence of the object. One may expect this to depend on the signal-to-noise ratio of the measured radiation patterns, but also on gradients in the optical near field. The field of view is related to the spatial extent of a transducer with a complex multimode structure. Therefore, it is essential to optimise the geometry of the transducer to construct maximally localised near-field distributions, for instance using insights into the spatial mode structure of such arrays of apertures, exploiting plasmon resonances of the apertures. It would be exciting to investigate what physics fundamentally limits the precision and field of view. In the current experiments, the library and test data have been obtained using the same transducer. Whether every realisation of the transducer requires separate calibration would be an interesting question, and robustness of the library could be taken into account in the design of the transducer. Making use of additional degrees of freedom, such as polarisation and wavelength, can enable encoding of even more information in radiation patterns. Although in this work, we focusfed on a multiplexed readout of multiple degrees of freedom in the signal scattered from a complex nanophotonic near-field transducer, an alternative route towards rapid nanoscale sensing without physical movement of the transducer would be to incorporate active reconfiguration of the illumination conditions, with the aim of shaping the transducer optical near field [19–21]. We will explore this approach in chapter 5. Extraction of nanoscale information with a combination of complex illumination, transducer, and detection opens up further avenues of improvement using compressive sensing methods [22, 23]. We note that, while in the current demonstration a microscope objective has been used for illumination and collection, our technique is compatible with multimode fibre-based imaging methods [24, 25]. This opens up the possibility of integrating nanostructured transducers at the end of high-numerical aperture fibres that could be advantageous in industrial applications. Promising prospects of nanophotonic near-field transducers could for instance be found in the detection of nanoscale defects and contaminants for large-area mask or wafer inspection in semiconductor industry. Our approach to encode subwavelength position information in radiation patterns using a near-field transducer may also extend to fluorescence microscopy, thereby impacting super-resolution imaging in biophysical contexts [26].

REFERENCES

1. Hell, S. W. & Wichmann, J. "Breaking the diffraction resolution limit by stimulated emission: stimulated-emission-depletion fluorescence microscopy". *Opt. Lett.* **19,** 780 (1994).
2. Betzig, E., Patterson, G. H., Sougrat, R., Lindwasser, O. W., Olenych, S., Bonifacino, J. S., Davidson, M. W., Lippincott-Schwartz, J. & Hess, H. F. "Imaging intracellular fluorescent proteins at nanometer resolution". *Science* **313,** 1642–1645 (2006).
3. Pohl, D. W., Denk, W. & Lanz, M. "Optical stethoscopy: Image recording with resolution $\lambda/20$". *Appl. Phys. Lett.* **44,** 651–653 (1984).
4. Lewis, A., Isaacson, M., Harootunian, A. & Muray, A. "Development of a 500 Å spatial resolution light microscope: I. light is efficiently transmitted through $\lambda/16$ diameter apertures". *Ultramicroscopy* **13,** 227 (1984).
5. Zenhausern, F., O'Boyle, M. P. & Wickramasinghe, H. K. "Apertureless near-field optical microscope". *Appl. Phys. Lett.* **65,** 1623 (1994).
6. Bachelot, R., Gleyzes, P. & Boccara, A. C. "Near-field optical microscope based on local perturbation of a diffraction spot". *Opt. Lett.* **20,** 1924 (1995).
7. Zenhausern, F., Martin, Y. & Wickramasinghe, H. K. "Scanning interferometric apertureless microscopy: optical imaging at 10 angstrom resolution". *Science* **269,** 1083–1085 (1995).
8. Sersic, I., Tuambilangana, C. & Koenderink, A. F. "Fourier microscopy of single plasmonic scatterers". *New. J. Phys.* **13,** 083019 (2011).
9. Kurvits, J. A., Jiang, M. & Zia, R. "Comparative analysis of imaging configurations and objectives for Fourier microscopy". *J. Opt. Soc. Am. A* **32,** 1081 (2015).
10. Bouchet, D., Carminati, R. & Mosk, A. P. "Influence of the local scattering environment on the localization precision of single particles". *Phys. Rev. Lett.* **124,** 133903 (2020).
11. Neugebauer, M., Woźniak, P., Bag, A., Leuchs, G. & Banzer, P. "Polarization-controlled directional scattering for nanoscopic position sensing". *Nature Commun.* **7,** 11286 (2016).
12. Bag, A., Neugebauer, M., Woźniak, P., Leuchs, G. & Banzer, P. "Transverse Kerker scattering for angstrom localization of nanoparticles". *Phys. Rev. Lett.* **121,** 193902 (2018).
13. Shang, W., Xiao, F., Zhu, W., Han, L., Premaratne, M., Mei, T. & Zhao, J. "Unidirectional scattering exploited transverse displacement sensor with tunable measuring range". *Opt. Express* **27,** 4944 (2019).
14. Bag, A., Neugebauer, M., Mick, U., Christiansen, S., Schulz, S. A. & Banzer, P. "Towards fully integrated photonic displacement sensors". *Nat. Commun.* **11,** 2915 (2020).
15. Nechayev, S., Eismann, J. S., Neugebauer, M. & Banzer, P. "Shaping field gradients for nanolocalization". *ACS Photonics* **7,** 581 (2020).

16. Veerman, J. A., Otter, A. M., Kuipers, L. & van Hulst, N. F. “High definition aperture probes for near-field optical microscopy fabricated by focused ion beam milling”. *Appl. Phys. Lett.* **72,** 3115 (1998).

17. Karrai, K. & Grober, R. D. “Piezoelectric tip-sample distance control for near field optical microscopes”. *Appl. Phys. Lett.* **66,** 1842 (1995).

18. Garcia-Vidal, F. J., Martin-Moreno, L., Ebbesen, T. W. & Kuipers, L. “Light passing through subwavelength apertures”. *Rev. Mod. Phys.* **82,** 729 (2010).

19. Sentenac, A. & Chaumet, P. C. “Subdiffraction light focusing on a grating substrate”. *Phys. Rev. Lett.* **101** (2008).

20. Kao, T. S., Jenkins, S. D., Ruostekoski, J. & Zheludev, N. I. “Coherent control of nanoscale light localization in metamaterial: creating and positioning isolated sub-wavelength energy hot spots”. *Phys. Rev. Lett.* **106,** 085501 (2011).

21. Roubaud, G., Bondareff, P., Volpe, G., Gigan, S., Bidault, S. & Grésillon, S. “Far-field wavefront control of nonlinear luminescence in disordered gold metasurfaces”. *Nano Lett.* **20,** 3291–3298 (2020).

22. Romberg, J. “Imaging via compressive sampling”. *IEEE Signal Process. Mag.* **25,** 14 (2008).

23. Candès, E. J. & Wakin, M. B. “An introduction to compressive sampling”. *IEEE Signal Process. Mag.* **25,** 21 (2008).

24. Čižmár, T. & Dholakia, K. “Shaping the light transmission through a multimode optical fibre: complex transformation analysis and applications in biophotonics”. *Opt. Express* **19,** 18871 (2011).

25. Amitonova, L. V. & de Boer, J. F. “Endo-microscopy beyond the Abbe and Nyquist limits”. *Light Sci. Appl.* **9,** 81 (2020).

26. Aouani, H., Mahboub, O., Bonod, N., Devaux, E., Popov, E., Rigneault, H., Ebbesen, T. W. & Wenger, J. “Bright unidirectional fluorescence emission of molecules in a nanoaperture with plasmonic corrugations”. *Nano Lett.* **11,** 637–644 (2011).

5

PROGRAMMING METASURFACE NEAR-FIELDS FOR NANO-OPTICAL SENSING

Control of optical fields at the nanoscale holds the promise of fast, efficient imaging methods, but is elusive due to the diffraction limit. In this chapter, we investigate how a single metasurface patch in the near field of a sample plane may be used to create a wide variety of intensity patterns by applying different illumination profiles from the far field. Numerical analysis shows that one metasurface patch may be used to generate complete bases of illumination patterns on a grid as fine as $\lambda/16$. *The limits of control are explored in terms of degrees of freedom on the illumination side and spatial resolution on the sample side. These illumination patterns are expected to enable sub-wavelength structured illumination microscopies, compressive imaging and sensing. Quantitative analysis of how the engineered fields may be used for detection of small scattering particles demonstrates the potential the approach holds for nanoscale optical sensing.*

The work described in this chapter has been published separately as *Adv. Opt. Mater.* 2100435 (2021)

5.1. INTRODUCTION

Optical fields are shaped by the interference of incident, scattered and re-emitted fields. Control of such optical fields, in particular of the distribution of field intensity in space, is key to both optical microscopy [1–4] and lithography [5, 6]. At sufficiently large scales, such control can be provided by far-field optics, for instance through the imaging of binary masks [6], or its dynamic equivalent of active wavefront shaping [7, 8]. At the nanoscale, diffraction precludes arbitrarily fine far-field control of field structure [9–11]. In industrial lithography, the state of the art in resolution is achieved either by accepting the diffraction limit and using the smallest possible wavelength [12] or by forgoing optics altogether by switching to electron beam writing [13]. Super-resolution techniques, like near-field scanning optical microscopy (NSOM) [14–16] and photo-activated localisation microscopy (PALM) [17–19], show a number of ways to work around the limitations of far-field optics, achieving deeply sub-diffractive resolution. However, fluorescence-based techniques are limited to sparsely distributed sources and scanning probes have very simple and small exposure or collection volumes that necessitate slow, point-by-point raster-scanning measurements. Modern inverse design approaches to computational imaging and parameter retrieval [20–22] (see also chapter 3) defeat these constraints by careful modelling. Yet, these methods take up either additional complexity to account for their limited knowledge of exposure field patterns or the requirement of detailed a priori knowledge on the family of structures under study. Improved control of nanoscale fields would drastically expand the range of applications where such computational imaging can compete with traditional super-resolution techniques.

Structuring light on the nanoscale for imaging purposes has been studied in a number of contexts and by a number of methods. Beams generated by far-field optics can generate nanoscale features through the phenomenon of superoscillation [23, 24], but superoscillatory features are inevitably many orders of magnitude weaker than the corresponding diffraction-limited spot and have large sidebands [25–28]. In order to control nanoscale fields without those drawbacks, one has to make use of structures in the near-field of the target plane. This notion leads to nanoscale equivalents of structured illumination microsopies, wherein imaging and sensing information can be retrieved from measurements in which an object has been illuminated by a sequence of diverse illuminations [3, 29–31]. One such approach is based on disordered media, where illumination naturally creates optical bright spots, with positions dependent on incident wavefront [32, 33]. Other approaches use periodic lattices, which permit the creation of hot-spots at positions linked to lattice sites [34, 35]. Finally, the hot-spots of small systems of plasmonic particles may be controlled by incident polarisation [36], by wavelength and incidence angle [37, 38], or by illumination with pulses that are suitably shaped in time [39]. For imaging and sensing it would be highly desirable to have a solution able to provide hot-spots that can be controlled independently over a large area, or at least able to provide near field illumination patterns that are sufficiently diverse and linearly independent to form a complete basis for imaging. No one of the solutions outlined above can provide independently controllable hot-spots over a large area. For very small areas of interest, a few-particle system can provide a good level of control. The degree to which this fine control can be extended to larger areas by adding more modes to the system remains an open question.

In this chapter, we explore how supplying specific far-field illumination patterns to a

metasurface patch can dynamically shape near-field energy distribution. We use numerical optimisation of wavefronts to optimise for desired near-field patterns and show that this approach can generate complete bases of near-field patterns below a fixed array of dipolar resonant scatterers. We study the illumination wavefronts required to generate these patterns. We investigate the conditions under which fields can be generated reliably and discuss the scattering physics underpinning the structure of the near-field patterns. Looking towards applications, we demonstrate that the engineered near-field distributions may be used to detect scattering particles.

5.2. METHOD

We consider a two-dimensional system of subdiffractively spaced scattering sites, referred to as a metasurface patch, close to a target (sample) plane, as sketched in figure 5.1. The question we wish to answer is: supposing one illuminates this metasurface patch from the far field through a high-NA microscope objective, with full control over the wavefront offered in the objective back focal plane, what field intensity distributions can one make in the target plane? As a first step to answering this question, we select a specific metasurface patch design: a 4×4 square grid with pitch $\lambda/4$, situated $\lambda/8$ to the left of the target plane, illuminated from the left. The scattering elements are taken to be identical isotropic strong scatterers, resonant at the drive frequency, with a polarisability of $|\alpha| = 5.56\times10^{-33}\,\mathrm{C\,m^2\,V^{-1}}$ and a quality factor of $Q = 10$, comparable with 100 nm silver plasmonic nanoparticles at optical frequencies. We treat this as an optimisation problem, optimising the illumination to create given near field patterns on the grid of positions in the target plane directly beyond the metasurface patch scatterers.

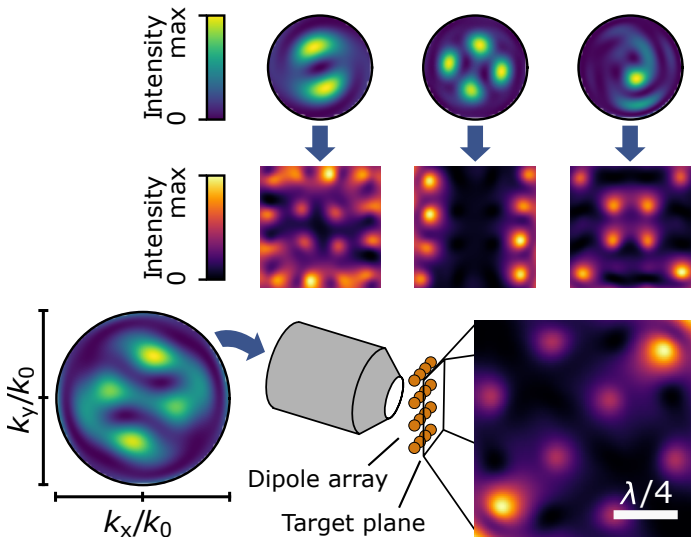

Figure 5.1: The problem setting explored in this chapter: an incident field is focussed onto a dipole array, where the scattered fields produce a specific intensity pattern just beyond the array. We aim to find incident fields that will produce arbitrary intensity patterns.

In order to calculate the near-field distribution that a given incident field will result in, we model the metasurface patch as a collection of discrete dipoles. The discrete dipole model, discussed in section 2.2, allows us to quickly work out the qualitative behaviour of sets of interacting particles [40–43] and natively includes multiple scattering, self-action and retardation [44, 45]. For the metasurface patch, three orthogonal induced electric dipole moments describe each of the sixteen scatterers. The final amplitude and phase distribution is found as the self-consistent sum of the incident field and the multiple scattering-induced fields of all dipoles. As we are primarily interested in the range of distinct patterns that can be created, rather than the precise parameters required, we take the environment of the particles to be homogeneous in refractive index, instead of accounting for, e.g., supporting substrates. This scenario could be obtained experimentally using index matching oil. Alternatively, our approach could be extended to account for arbitrary series of interfaces by appropriately modifying the dipoles' Green's functions [46].

We envision illumination to be offered as a programmable paraxial, cylindrical beam, incident on the back focal plane of an objective. The objective transforms the incident beam into a shaped spherical wave converging onto the metasurface patch. This transformation can be mathematically described by the well known microscope objective transformation rules for aplanatic lenses, which relate incident beams of finite circular aperture (equivalent to NA ≤ 1) to object-side spherical waves upon evaluation of a diffraction integral [47, 48]. We model the incident illumination as a paraxial beam with its waist at the aperture edge, expanded in the Laguerre-Gauss basis [49, 50], given by

$$E_{p,l}(r,\phi,z) = C_{\mathrm{lp}}^{\mathrm{LG}} \frac{1}{w(z)} \left(\frac{r\sqrt{2}}{w(z)} \right)^{|l|} L_p^{|l|} \left(\frac{2r^2}{w^2(z)} \right) \mathrm{e}^{-\frac{r^2}{w^2(z)} - ik\frac{r^2}{2R(z)} - il\phi + i\psi(z) - ikz}. \tag{5.1}$$

Here we use cylindrical coordinates r, ϕ and z, with waist at focus w_0 and $w(z) = w_0\sqrt{1+(z/z_R)^2}$ with Rayleigh range $z_R = \left(k\, w_0^2\right)/2$, radius of curvature $R(z) = z\left[1+\left(\frac{z_R}{z}\right)^2\right]$, Gouy phase $\psi = (2p+|l|+1)\arctan(z_R/z)$, a normalisation factor $C_{lp}^{\mathrm{LG}} = \sqrt{2/\pi}\sqrt{p!/(p+|l|)!}$, $L_p^{|l|}$ the generalised Laguerre polynomials, and integer p and l with $p \geq 0$. This basis consists of cylindrically symmetric amplitude patterns, with phase wrapping l times around the origin. Given this symmetry, the Laguerre-Gauss basis is a natural way to describe fields on a circular aperture. Since we are interested in the level of control over near fields that one can obtain with limited degrees of freedom in the incident beam, we truncate the basis to finite maximum p and l. Importantly, microscope objectives have a hard cut-off at finite beam radius r, which maps to the numerical aperture of the objective and thus the edge of its back focal plane. While the pure Laguerre-Gauss basis is orthonormal, truncating it to a finite aperture removes the normalisation, as well as orthogonality between basis elements with identical p. To restore orthonormality, we use a modified Laguerre-Gauss basis with indices p' and l. Each $E_{p'_i,l}$ is constructed from the elements $E_{p_j,l}$ with $j < i$ through the Gram-Schmidt process [51, 52], resulting in an orthonormal basis $E_{p'_j,l}$ for $j < i$.

For a given target near-field pattern we seek optimal illuminations through numerical optimisation of the coefficients for each (p', l) basis element. For an orthonormalised Laguerre-Gauss basis truncated at $p'_{\max}$ and $l_{\max}$, with two polarisation degrees of freedom, there are $N = 2\,(p'_{\max}+1)\,(2l_{\max}+1)$ input parameters. We denote these as the complex coefficients $c_{p',l}$, with the full vector having Euclidean norm $||c_{p',l}|| = 1$, corresponding

to unit power. We shall primarily use the first 30 modes, with $p' \leq 2$ and $|l| \leq 2$, but will also explore the effect of using more and fewer modes. Through the discretised diffraction integral [47, 48] we find the incident field driving the metasurface patch, which is input to the discrete dipole model that lets us calculate the resulting near-field intensity distribution in the target plane. The optimisation procedure is to find the complex coefficient $c_{p',l}$ values that results in a target plane field distribution most similar to a set target distribution. We will look for field patterns with spots in the target plane in the same grid as the scattering sites in the metasurface, as the near-field hot-spots of the scattering sites provide fine features to field structure through their localised field enhancement hot-spots. In this way, a 4×4 metasurface can address a 4×4 target pattern $\mathbf{t}$. Since the scatterer hot-spots at each target position are expected to be the only sharp features in the field distributions, we may also expect these positions to provide a representative picture of the overall field distribution. On the target points, we consider binary target patterns $\mathbf{t}$: each individual position is either required to be on, or off. We judge the match between the observed pattern $\mathbf{s}$ at the selected positions and the target pattern $\mathbf{t}$ by a fitness function based on cosine similarity. Cosine similarity $S(\mathbf{s},\mathbf{t})$ is the most commonly used metric to compare high-dimensional patterns [53, 54]. It finds the angle between two vectors:

$$S(\mathbf{s},\mathbf{t}) = \frac{\mathbf{s}\cdot\mathbf{t}}{||\mathbf{s}||\,||\mathbf{t}||}$$

For vectors $\mathbf{s}$ and $\mathbf{t}$ with only positive entries, $S(\mathbf{s},\mathbf{t})$ lies between 0 (orthogonal) and 1 (perfect match). Cosine similarity only describes the shape of a pattern and is not sensitive to its intensity. We separately include an intensity criterion in the fitness function, to reward solutions where an appreciable fraction of intensity ends up in the target pattern, rather than in side lobes. This leads to the following fitness function:

$$F(\mathbf{s},\mathbf{t},\Theta) = \frac{1}{2}S(\mathbf{s},\mathbf{t}) + \frac{1}{2}C(\mathbf{s},\mathbf{t},\Theta) \qquad \text{with} \qquad C(\mathbf{s},\mathbf{t},\Theta) = \min(1, \frac{\sum \mathbf{s}}{\Theta \sum \mathbf{t}})$$

With threshold $\Theta = 0$ this fitness function is pure cosine similarity. The threshold introduces a penalty for solutions that have less than a certain amount of energy per 'on' position. Using a threshold rather than a continuous scale, rewarding more intensity, means that the 'energy landscape' we are optimising over is not affected once the solver reaches sufficient intensity in the solution, thereby retaining the desirable features of cosine similarity. To obtain a gauge for sensible threshold values, we express it as a fraction of the maximum peak intensity $P_{\max}$ attainable at the focus of a beam with unit power at NA = 1. Dipole field enhancement may lead to peak intensities greater than this reference value. For now, we set a threshold of $\Theta = P_{\max}/100$; we will explore the effect of different threshold levels later on. For the optimisation itself, we use Powell's conjugate direction method as implemented in NumPy [55], starting from random starting amplitude and phase in each coefficient and normalising the coefficients at subsequent iterations to maintain unit power. In order to save computation time, we tabulated the fields in the target plane for the various orthonormalised Laguerre-Gauss elements and exploit linear superposition to find fields for arbitrary coefficients. optimisation with $p'_{\max} = 2$ and $|l|_{\max} = 2$ converges in seconds on a standard desktop computer. The best fitness results out of a few tens of runs are used in order to avoid suboptimal local minima. Per this procedure, we find

illumination patterns that produce a local optimum in fitness, as measured by two criteria: first, by having the right intensity pattern and second, by having a minimum intensity per 'on' position.

5.3. COMPLETE BASES OF EXPOSURE PATTERNS

We first test our method by setting as target the addressing of individual points in the 4×4 grid, optimising intensity at a specific point and keeping the others dark. Figure 5.2a-c shows the obtained solutions for the three points that are unique under symmetry: corner (5.2a), edge (5.2b) and bulk (5.2c). In each case, field intensity in the target plane shows a distinct single peak at the desired position, proving (by symmetry) that the method can specifically address any position on the grid. By the fitness metric used in optimisation, these solutions match 100% to the optimisation target. Before exploring the structure of these solutions, we show that the method can also reproduce multiple-spot patterns: figure 5.2d shows an optimised checkerboard pattern on the same grid, with the checkerboard clearly recognisable. The ability to address specific sets of points is notable, considering that the $\lambda/4$ separation between the target points is appreciably smaller than the diffraction limit.

In order to understand how the method achieves these target plane field structures, we examine the induced dipole moments in the scatterers. In the same subfigures 5.2a–d we show the magnitude of the dipole moments in the metasurface under the illumination conditions producing this solution, as well as the magnitude of their z-components. Looking at the induced scatterer dipole moments for each solution, we observe that the spots generally correspond to strong z dipole moments. The spots may thus be regarded as the hot-spots of individual dipoles, which accounts for their observed sub-diffractive width ($\approx \lambda/5$). Most of the other dipoles have negligible dipole moment or are oriented in-plane, directing their largest field enhancement out of the target plane. Some notable exceptions, like the corner sites on the checkerboard (figure 5.2d), are oriented mostly in-plane. In these cases the target position lies on the flank of a comparatively broad feature with its field in-plane. For each solution we also show the incident wavefronts found to produce these solutions. The incident wavefronts are shown as calculated at the microscope objective back focal plane, specifically as the required flux density on the Abbe sphere plotted as a function of parallel momentum (k_x, k_y) of the spherical wave offered to the metasurface targets. We see that solutions are fairly smooth, with a few large bright spots. This is promising with an eye to experimental implementation, as it suggests that limited spatial resolution in creating wavefronts will not hamper performance.

By way of illustration, we explore the bulk spot solution in some more detail. Figure 5.2e shows how the incident field is built up from the different orthonormalised Laguerre-Gauss elements in two polarisation channels. Incident field basis elements with $l \neq 0$ are required to produce a solution that is not circularly symmetric. Balancing elements with opposite l produces l-fold symmetric patterns, which can be rotated by the relative phases for the elements. Following this far-field design strategy, as one might when tasked to solve the problem by hand, would result in a set of weights symmetric around $l = 0$. Though we can certainly recognise a semblance of the expected symmetry in the corner and bulk solutions, this symmetry is imperfect. Another symmetry that could have been analytically expected and is shown to a limited degree by the numerical solutions is that

between the x and y polarisation channels, which is also seen by the symmetry across the diagonal in the drive fields for figures 5.2a and 5.2c. Such solutions, that respect the symmetries of the various problems, may form the global minimum in the fitness landscape of our optimisation. However, it may also be that several distinct solutions solve the optimisation problem, possibly not all respecting the underlying symmetry. In any case it is an interesting observation that the demonstrated level of convergence is evidently sufficient to obtain effective solutions.

Finally, we plot the intensity distribution produced by the bulk spot solution in the target plane in the absence of the dipole array (figure 5.2f) and the same in the dipole array plane (fig 5.2g). Field intensity still peaks at the target position, but much less sharply than is the case in presence of the scatterer array, with appreciable intensity at both neighbouring dipole positions and neighbouring target positions. The single fine spot observed in the actual solution before must thus be the result of multiple scattering within the array. This balances enhancing the field at the target spot with simultaneously cancelling out the drive field away from the target by destructive interference, resulting in a high-fitness solution.

Besides the single point basis, applications may benefit from the ability to generate other bases. Here we specifically think about compressive sensing techniques that may allow information retrieval with fewer measurements than a single-pixel measurement basis would require. We attempt to create one example, the Hadamard basis. This basis is given by the rows of a Hadamard matrix H_n of size $n \times n$, defined as a solution of $H_n H_n^T = nI_n$ [56–58]. Hadamard matrices form the optimal basis in a number of compressed sensing applications and are commonly used for that reason [59–61]. For n a positive integer power of two, Hadamard matrices may be constructed blockwise through [56]

$$H_1 = [1] \qquad H_{2^k} = \begin{bmatrix} H_{2^{k-1}} & H_{2^{k-1}} \\ H_{2^{k-1}} & -H_{2^{k-1}} \end{bmatrix} \tag{5.2}$$

Hadamard matrices have entries equal to 1 and -1. As we cannot produce negative intensity, we will use offset Hadamard matrices with low level zero. When we map each of the sixteen patterns in the basis H_{16} onto our 4×4 grid, we see that ten are unique by symmetry (for instance, $H_{16}(2)$ is equivalent to $H_{16}(5)$). We use our optimisation technique to attempt to reproduce these patterns, with a binary on/off mask as before. The resulting optimal field intensity distributions are seen in figure 5.3a. We immediately recognise the target patterns in the solutions, illustrating the flexibility of illumination control on the metasurface patch in generating field distributions. In order to demonstrate yet more intricate fields, we can apply the same procedure to an 8×8 metasurface patch and accordingly more target positions. With 64 distinct target spots, the 30 orthonormalised Laguerre-Gauss modes used so far are insufficient to produce a complete basis, so we use $p'_{\max} = 6$ and $|l|_{\max} = 6$ for this optimisation. Figure 5.3b shows the result for one of the more challenging target field distributions in the 8×8 patch. Again, the pattern is clearly recognisable. Using the power of reconfigurable illumination, our general-purpose, unoptimised metasurface is seen to be suitable for the generation of near field patterns that enumerate intricate, complete bases, exploiting the coupling between different elements and the interference between drive and scattered fields.

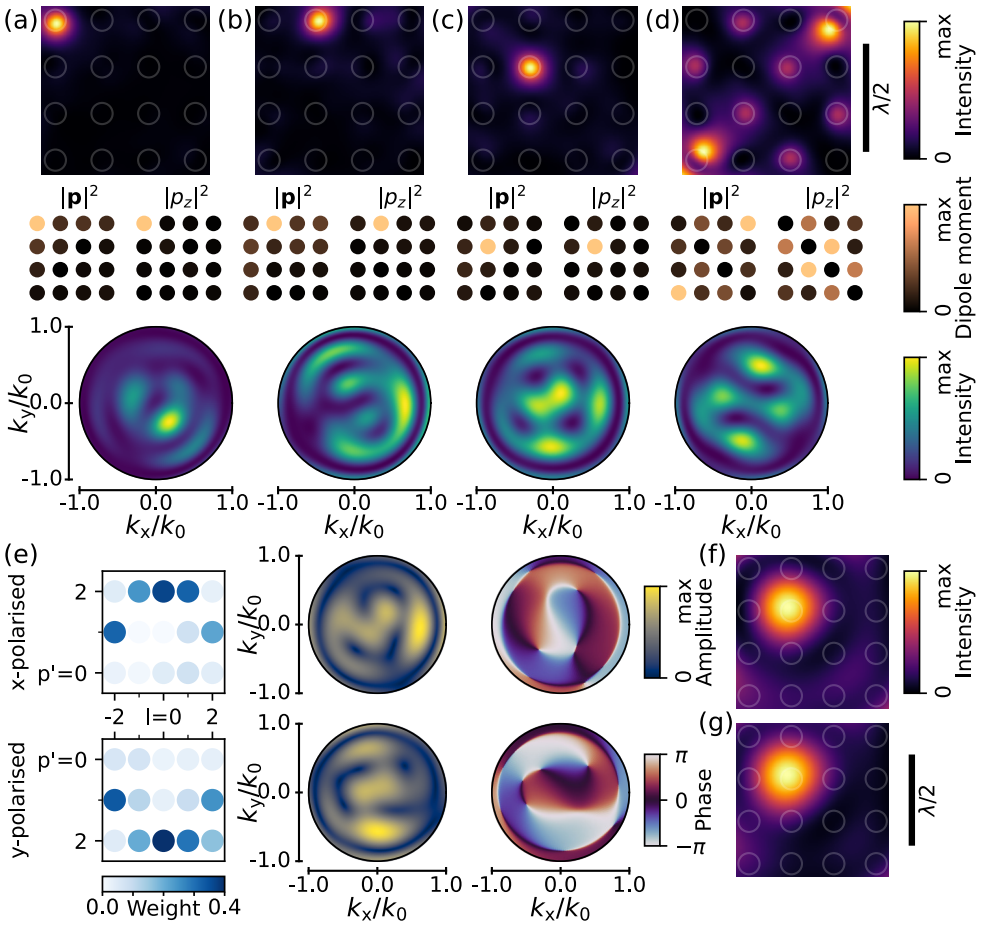

Figure 5.2: Structure of optimal solutions. (a) Solution for single spot at corner of 4×4 grid. Field map shows intensity, with white circles indicating target positions. Dipole moment magnitude and dipole moment z-component are plotted for each dipole in the array, both normalised to the strongest dipole moment magnitude in the array. Finally, the incident field pattern found by the optimiser to produce this result is shown. The incident field pattern is shown as energy flux on the Abbe sphere, plotted in wavevector space. (b-d) Like a, but for a target hot-spot at an edge position, a target hot-spot at a bulk position and a checkerboard target. (e-g) Detailed structure of the bulk position solution in (c). (e) Incident field pattern, with weights for each element in the orthonormalised Laguerre-Gauss basis for x- and y-polarisations and the resulting field pattern amplitude and phase for both polarisation channels. (f) Intensity profile produced by the optimised incident field in the dipole plane, without scatterers present. Positions corresponding to target positions are circled. (g) Like f, but intensity profile in the target plane.

5.4. RESOLUTION AND EFFICIENCY LIMITS

Looking towards nano-optical field control and sensing, it is interesting to see how far below the diffraction limit we can push the optimisation method. The metasurface patches considered so far were all taken to have a subdiffractive pitch of $\lambda/4$. We repeat the Hadamard pattern optimisation procedure for pitches from $\lambda/2$, close to the diffraction

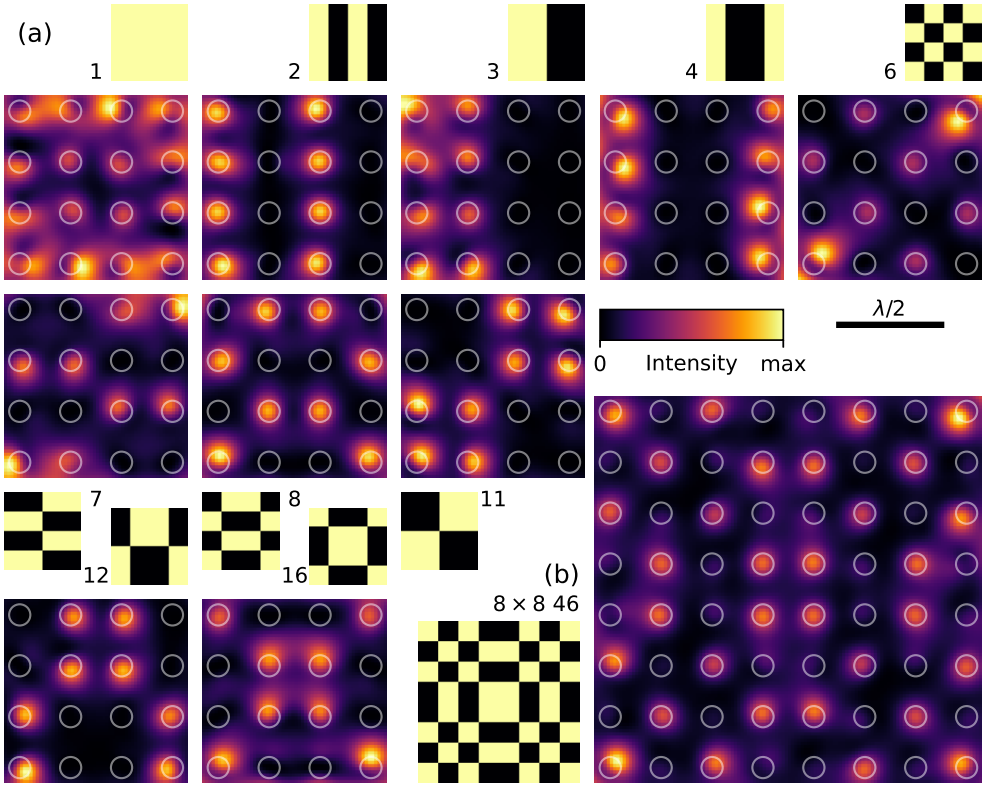

Figure 5.3: Complex patterns reproduced by tailored illumination of a dipole array. (a) The complete Hadamard basis reproduced on a 4×4 grid, with only those patterns unique under symmetry shown. Besides normalised field intensity maps, insets show the target pattern and labels indicate the pattern index. All intensity maps are normalised to their maximum value and shown at the same scale; target positions are circled. (b) One element of the Hadamard basis on an 8×8 grid, specifically number 46. Shown as in (a), using the same scale.

limit, through $\lambda/32$, more than an order of magnitude below it. In order to do so, we scale the entire system down proportionally, so that array-target distance is always one-half of the array pitch. As shown in figure 5.4a, obtained fitness is excellent for all patterns at large pitch, with a general trend of fitness decreasing with smaller pitch. When interpreting values of the fitness function, it should be noted that only very high values are sure to faithfully reproduce the pattern, because, for instance, for an all-on target, a solution where one position has no intensity at all may still have 97% fitness. To get a better understanding of which solutions worked, we use a digital criterion: a solution is successful if all 'on' spots are over 2/3 of the maximum intensity and simultaneously all 'off' spots are under 1/3 of the maximum intensity. This criterion is useful for characterising solutions returned by the optimisation, even though it is not suitable as a direct optimisation metric itself because its landscape is not smooth [62]. Solutions for which the criterion is not met are marked with a black dot in figure 5.4a. We see that solutions with fitness over 98% are generally successful. With this criterion, we see that all solutions successfully reproduce

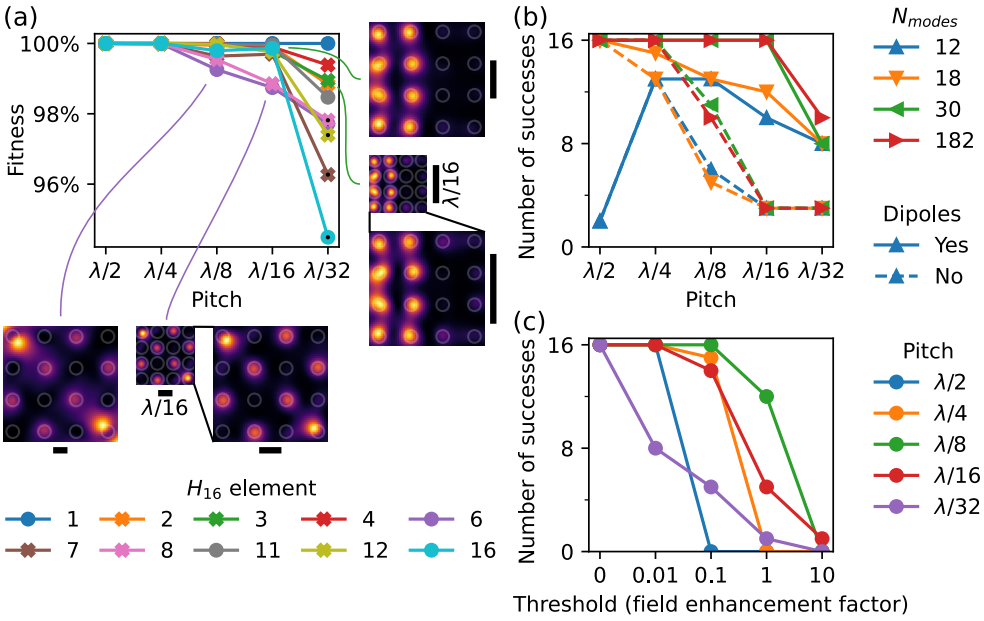

Figure 5.4: Limits to optimisation. (a) Fitness of solutions for H_{16} elements at different scales. Field maps show specific solutions for Hadamard elements 6 (below) and 3 (right). All scale bars have length $\lambda/16$ and intensity maps are shown as in figure 5.3. (b) Number of H_{16} Hadamard elements successfully reproduced with different numbers of far-field modes. Solid lines show results with dipole array, dashed lines without. (c) Number of H_{16} Hadamard elements successfully reproduced with different intensity thresholds.

5

their target patterns down to pitch $\lambda/16$. Notably, the loss in performance is much stronger for some target patterns than for others. This is mostly explained by considering the spatial frequencies present in the various patterns, one extreme case being the uniform all-on pattern $H_{16}(1)$. This pattern barely loses performance from the largest to the smallest pitch and at any scale would be solved by an 'electrostatic' approach. In this case, the target pattern has an intrinsic symmetry that can be exploited directly, rather than requiring a tuning of the retarded multiple scattering interactions between metasurface elements. The checkerboard $H_{16}(6)$ on the contrary is a tricky problem, as evidenced by it achieving the lowest fitness at pitch $\lambda/8$ and failing at $\lambda/32$. The solutions for pitch $\lambda/8$ and $\lambda/16$, in the lower insets, show that at smaller pitch, the hot-spots in fact become *more* distinct, due to the smaller distance between the dipoles and the target plane. Nonetheless, fitness worsens slightly. The reason for this is that although the features around the 'on' dipoles become sharper at small distance, parasitic features appear at the 'off' dipoles as well. This effect is more pronounced in the right-hand insets, which show the solutions for $H_{16}(3)$, an easier, lower-frequency target, at pitch $\lambda/16$ and $\lambda/32$. Here we see the same trend: at extremely short distances, even out-of-plane dipole moments lead to appreciable intensity in the target plane. We thus see that although eventually low contrast in the drive field limits our ability to address sites independently, multiple scattering within the array can take us a full order of magnitude beyond the diffraction limit.

The incident field basis used in optimisation is truncated to a limited number of ele-

ments. Intuitively it stands to reason that each additional basis element adds a degree of control over the drive field features. It is interesting to see how this control over incident field features translates to control over target plane features. We test this relation by varying the number of modes in our optimisation routine and comparing performance, using 12 ($(p'_{\max}, l_{\max}) = (1,1)$), 18 ($(p'_{\max}, l_{\max}) = (2,1)$), 30 ($(p'_{\max}, l_{\max}) = (2,2)$)and 182 ($(p'_{\max}, l_{\max}) = (6,6)$) modes. With 16 individual target sites, assuming linearity, we would expect to need at least that many basis elements to reproduce any complete basis. Figure 5.4b (solid lines) shows how the number of available modes affects performance, counting the successfully reproduced patterns (out of 16) versus array pitch. As observed previously, with 30 modes, we successfully reproduce all elements for pitch as small as $\lambda/16$. Optimisation with 12 modes is insufficient to produce all 16 elements at any pitch, as expected, but already 18 is sufficient at large pitch. At 30 modes nearly all solutions are already successful. Adding more modes beyond this point makes relatively little difference: a six-fold increase in the number of modes, from 30 to 182, adds only a single successful solution, at pitch $\lambda/32$. That our problem is not linear — we optimise for intensity — appears to have only limited effect on the number of required basis functions, with close to the bare minimum of modes required in a linear system already providing nearly full control. Why 18 is not enough may be related to the intensity criterion used, or to large overlap between the drive fields corresponding to some of the elements after focussing. The minor improvement in performance offered by additional modes at very small pitch seems to confirm our earlier interpretation: performance there is limited by low contrast between different dipole and target positions in the drive fields.

The relative importance of drive field structure and dipole-dipole interaction may be disentangled by considering the same problem without the dipole array, and instead using wavefront shaping to directly create intensity patterns in the target plane. Results of this process are shown by dashed lines in figure 5.4b. At large pitch, performance without the dipole array is remarkably similar to that with the dipole array, with full control achieved from 18 modes onwards. However, only with the largest number of modes can all targets still be solved at pitch $\lambda/4$. Towards smaller pitch, the loss of control is drastic, with only the simplest patterns reproduced successfully. This shows that at fine resolutions, multiple scattering of the drive field by the dipole array is the mechanism that allows the full complexity of target patterns to be reached.

It is well known that arbitrarily fine sub-diffractive features in optical fields can be engineered by exploiting super-oscillation. Such control comes at the expense of intensity, with parasitic features typically over five orders of magnitude stronger than the desired sub-diffractive feature [25–28]. Though fundamentally different, we can compare the field strengths obtained in our method with such results. Dipole hot-spots can provide large field enhancement, but we may not be able to exploit this fully due to a combination of two aspects. The first reason is the finite distance between the dipole scatterers and the target plane, when accounting for realistically size optical antennas. Furthermore, interactions between dipoles spaced closely together limit the polarisability that one can pack in a single optical antenna. Our fitness criterion contains a threshold Θ: the minimum required peak intensity at the target positions relative to incident field maximum peak intensity. We can vary this threshold to see how easily we can realise solutions at the given intensity. Figure 5.4c shows the results of this analysis, ranging from no intensity criterion

at all to a required significant field enhancement. Without the intensity criterion, the full Hadamard basis is reproduced successfully, even at pitch $\lambda/32$. At $\Theta = P_{\max}/100$, all but the highest-resolution targets still work. Beyond this, performance falls off quickly. Interestingly, the best results at any given intensity criterion are found at a pitch of $\lambda/8$. This may represent a balance between small dipole-sample distance, which increases intensity, and antenna resonance hybridisation effects that would lead to a detuning of the system from the assumed optical drive frequency, which would thereby tend to reduce intensity enhancement. Overall, we see that $\Theta = P_{\max}/100$ leads to good solutions. Though not exploiting dipole field enhancement in the way a single scanning dipole can, we see that unlike the other extreme of superoscillation, our method is able to retain an appreciable fraction of incident intensity in the target plane.

5.5. NANOSTRUCTURES FOR SENSING AND LOCATING SMALL SCATTERERS

While freely programmable near-field patterns with deep subwavelength resolution should in principle be of large use for microscopy, it is not immediately obvious how to utilise them to obtain images. We envision that the easiest usage scenario would be in fluorescent imaging. There, one could use a bucket detector with no spatial resolution for detected fluorescence, yet still obtain spatial information by cycling through a full basis of near field pump intensity patterns. This notion is similar to structured illumination microscopy [3, 31], which uses programmable though not spatially resolvable fluorescence excitation patterns. Key in this application scenario is that fluororphores are mutually incoherent local reporters of pump field intensity that are not themselves a partner in the multiple scattering process at the pump wavelength. Much more challenging would be image formation where the metasurface patch would serve as a near-to-far-field transducer to sense passive, i.e., scattering objects in the target plane (see chapter 4). To establish to what degree our optimised fields are suitable for sensing purposes, we calculate the effect of introducing a scattering particle into the target plane beyond the metasurface on the overall far-field scattered signals. We consider a weakly scattering, off-resonant perturber, with a polarisability of $|\alpha| = 5.56 \times 10^{-35}\,\mathrm{C\,m^2\,V^{-1}}$. This value corresponds to a small dielectric particle, best described in the single-scattering regime. For any incident field, we can calculate (or, in experiment, measure) the radiation pattern $\Phi_A(\mathbf{k})$ of the array, without the perturber, as flux per solid angle. The sensing signal we use is the total change in this radiation pattern as the perturber is introduced (resulting in a radiation pattern $\Phi_{A,P}(\mathbf{k})$, figure 5.5a), relative to the total flux $\Phi_P(\mathbf{k})$ scattered by the perturber when illuminated by a focussed beam of unit power, without the array:

$$S = \int_{\mathrm{BFP}} \left[\Phi_{A,P}(\mathbf{k}) - \Phi_A(\mathbf{k})\right] \, d\mathbf{k} \quad / \quad \int_{\mathrm{BFP}} \Phi_P(\mathbf{k}) \, d\mathbf{k} \tag{5.3}$$

Without the array, this dimensionless quantity would be limited to a maximum value of 1. Higher values should thus be taken to mean an improvement in sensing performance over straightforward free-space scatterometry. The dipole array has a scattering cross-section some four orders of magnitude larger than the perturber, which sets an upper bound on S. We calculate sensing signal S as a function of perturber position with some of the optimal

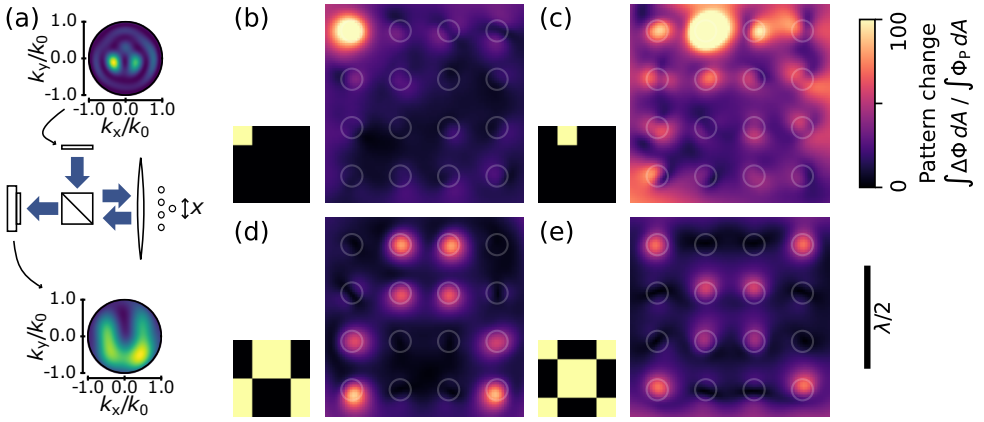

Figure 5.5: Sensing with the engineered fields. (a) The sensing method considered: an optimised wavefront is supplied to the perturbed dipole array. We detect changes in its scattering pattern. (b-e) Change in scattering signal versus position of a perturber, for different engineered incident fields. Insets show the pattern used.

drive fields found previously. Figures 5.5b-e show signal S versus perturber position for the target patterns corresponding to those in the insets. The scattered signal maps have peaks directly matching those in their target patterns, with the same sub-diffractive length scales. This means that a single measurement will reveal the presence or absence of the scatterer at its target sites, compatible both with simple searches and compressive sensing strategies [60]. Moreover, normalised signal level peaks at $S > 100$, meaning that the dipole array strongly enhances the signal compared with free-space measurement. We note that with no moving parts in the system, switching between different incident patterns can be done at video rates and faster, so that the technique could enable both efficient, rapid sensing, or sensing of objects moving in time. For instance, one can envision using metasurface patches with incident field control for sensing and tracking of freely diffusing analytes in solution [63].

5.6. DISCUSSION

We have explored how reconfiguration of far-field wavefronts may be used to control near-field intensity profiles mediated by a metasurface patch. With a small, rectangular metasurface grid, our numerical optimisation technique produces intensities under the metasurface elements that faithfully reproduce the target patterns. For both simple and complex bases, the technique is able to reproduce all basis elements faithfully at resolutions as small as $\lambda/16$. Studying the dipole moments in the array shows that the optimisation finds solutions that use the array dipole hot-spots to create the target patterns. We have investigated the structure of the required wavefronts and found they are fairly smooth, which makes experimental realisation feasible. Tweaking the optimisation conditions has allowed us to quantify the limits to this form of near-field control. With the thirty (orthonormalised) Laguerre-Gauss modes up to $p' = 2$ and $l = 2$, Hadamard patterns were reproduced faithfully for pitch as small as $\lambda/16$. An order of magnitude more modes proved insufficient to reproduce the complete basis at pitch $\lambda/32$. Looking into the intensity of

the hot-spots in the target patterns, we have found good solutions for intensities up to one order of magnitude below the maximum spot intensity of the incident beam. Finally, we have shown that the engineered fields can be used for programmable, position-selective particle sensing, with the metasurface patch providing significant enhancement in signal level compared to direct illumination.

All the results presented here are based on very simple metasurface patch designs: a square grid of either 4×4 or 8×8 identical and isotropic antennas right above the points of interest. The generated solutions that we find tend to have 'on' scatterers with large dipole moments along z, placing its plasmonic hot-spot in the target plane. This observation suggests that engineering of the metasurface patch, in terms of spatial arrangement and the per-building block polarisability tensor, should provide further control of near field programmability. For instance, one can envision engineering the scatterers to have hot-spots in certain locations by manipulating their electric and magnetic dipole and multipole response [64]. Another approach is to tailor the response of the scatterers to respond preferentially to certain polarisations or wavelengths, allowing different scatterers to contribute to different patterns [36, 38]. What sort of metasurface design is optimal for field control on a given set of target positions is an interesting question. For instance, it is unclear whether generally the scattering sites should be located directly over the points of interest, to maximally exploit their near-field enhancement, or at intermediate positions, to exploit collective behaviour like the Talbot effect [65] or other designed array features [66]. Another open question is how a finite patch from a periodic array, as used here, compares to layouts where every point has a distinct scattering environment, like in a plasmonic quasicrystal [67, 68]. The fact that even the simple metasurface patch design considered in our work already shows a fine level of control over near-field intensity distributions indicates that the combination of metasurface patches and programmable illumination will form a powerful new method for nano-optical sensing.

REFERENCES

1. Köhler, A. "Ein neues Beleuchtungsverfahren für mikrophotographische Zwecke". *Z. Wiss Mikrosk. Mikrosk. Tech.* **10,** 433–440 (1893).
2. Minsky, M. "Memoir on inventing the confocal scanning microscope". *Scanning* **10,** 128–138 (1988).
3. Heintzmann, R. & Huser, T. "Super-resolution structured illumination microscopy". *Chem. Rev.* **117,** 13890–13908 (2017).
4. Huszka, G. & Gijs, M. A. "Super-resolution optical imaging: A comparison". *Micro-Nano Eng.* **2,** 7–28 (2019).
5. *Introduction to Microlithography* (eds Thompson, L. F., Willson, C. G. & Bowden, M. J.) (ACS, 1983).
6. Bruning, J. H. "Optical lithography: 40 years and holding". in *Optical Microlithography XX* (ed Flagello, D. G.) (SPIE, 2007), 652004.
7. Tyson, R. *Principles of Adaptive Optics* (CRC Press, 2010).
8. Vellekoop, I. M. & Mosk, A. P. "Focusing coherent light through opaque strongly scattering media". *Opt. Lett.* **32,** 2309 (2007).

9. Abbe, E. “Beiträge zur Theorie des Mikroskops und der mikroskopischen Wahrnehmung”. *Arch. Mikrosk. Anat.* **9,** 413–468 (1873).
10. Strutt, J. W. “XXXI. Investigations in optics, with special reference to the spectroscope”. *Philos. Mag.* **8,** 261–274 (1879).
11. Lin, B. J. “Where Is The Lost Resolution?” in *Optical Microlithography V* (ed Stover, H. L.) **0633** (SPIE, 1986), 44–50.
12. Pirati, A. *et al.* “Performance overview and outlook of EUV lithography systems”. in *Extreme Ultraviolet (EUV) Lithography VI* (eds Wood, O. R. & Panning, E. M.) (SPIE, 2015).
13. Vieu, C., Carcenac, F., Pépin, A., Chen, Y., Mejias, M., Lebib, A., Manin-Ferlazzo, L., Couraud, L. & Launois, H. “Electron beam lithography: resolution limits and applications”. *Appl. Surf. Sci.* **164.** Surface Science in Micro & Nanotechnology, 111–117 (2000).
14. Pohl, D. W., Denk, W. & Lanz, M. “Optical stethoscopy: Image recording with resolution $\lambda/20$”. *Appl. Phys. Lett.* **44,** 651–653 (1984).
15. Taubner, T., Keilmann, F. & Hillenbrand, R. “Nanoscale-resolved subsurface imaging by scattering-type near-field optical microscopy”. *Opt. Express* **13,** 8893 (2005).
16. Lereu, A., Passian, A. & Dumas, P. “Near field optical microscopy: a brief review”. *Int. J. Nanotechnol.* **9,** 488 (2012).
17. Klar, T. A. & Hell, S. W. “Subdiffraction resolution in far-field fluorescence microscopy”. *Opt. Lett.* **24,** 954 (1999).
18. Betzig, E., Patterson, G. H., Sougrat, R., Lindwasser, O. W., Olenych, S., Bonifacino, J. S., Davidson, M. W., Lippincott-Schwartz, J. & Hess, H. F. “Imaging intracellular fluorescent proteins at nanometer resolution”. *Science* **313,** 1642–1645 (2006).
19. Thorley, J. A., Pike, J. & Rappoport, J. Z. in *Fluorescence Microscopy* 199–212 (Elsevier, 2014).
20. Haeberlé, O., Belkebir, K., Giovaninni, H. & Sentenac, A. “Tomographic diffractive microscopy: basics, techniques and perspectives”. *J. Mod. Opt.* **57,** 686–699 (2010).
21. Lin, Z., Roques-Carmes, C., Pestourie, R., Soljačić, M., Majumdar, A. & Johnson, S. G. “End-to-end nanophotonic inverse design for imaging and polarimetry”. *Nanophotonics* **10,** 1177–1187 (2020).
22. Bouchet, D., Seifert, J. & Mosk, A. P. “Optimizing illumination for precise multiparameter estimations in coherent diffractive imaging”. *Opt. Lett.* **46,** 254 (2021).
23. Francia, G. T. D. “Super-gain antennas and optical resolving power”. *Nuovo Cimento* **9,** 426–438 (1952).
24. Berry, M. “Faster than fourier”. in *Quantum Coherence and Reality* (World Scientific, London, 1994), 55–65.
25. Huang, F. M. & Zheludev, N. I. “Super-resolution without evanescent waves”. *Nano Lett.* **9,** 1249–1254 (2009).

26. Greenfield, E., Schley, R., Hurwitz, I., Nemirovsky, J., Makris, K. G. & Segev, M. "Experimental generation of arbitrarily shaped diffractionless superoscillatory optical beams". *Opt. Express* **21,** 13425 (2013).

27. Eliezer, Y. & Bahabad, A. "Super-Oscillating Airy pattern". *ACS Photonics* **3,** 1053–1059 (2016).

28. Rogers, K. S. & Rogers, E. T. F. "Realising superoscillations: A review of mathematical tools and their application". *JPhys Photonics* **2,** 042004 (2020).

29. Gustafsson, M. G. L. "Surpassing the lateral resolution limit by a factor of two using structured illumination microscopy". *J. Microsc.* **198,** 82–87 (2000).

30. Heintzmann, R. & Gustafsson, M. G. L. "Subdiffraction resolution in continuous samples". *Nat. Photonics* **3,** 362–364 (2009).

31. Mudry, E., Belkebir, K., Girard, J., Savatier, J., Moal, E. L., Nicoletti, C., Allain, M. & Sentenac, A. "Structured illumination microscopy using unknown speckle patterns". *Nat. Photonics* **6,** 312–315 (2012).

32. Bouchet, D., Carminati, R. & Mosk, A. P. "Influence of the local scattering environment on the localization precision of single particles". *Phys. Rev. Lett.* **124,** 133903 (2020).

33. Roubaud, G., Bondareff, P., Volpe, G., Gigan, S., Bidault, S. & Grésillon, S. "Far-field wavefront control of nonlinear luminescence in disordered gold metasurfaces". *Nano Lett.* **20,** 3291–3298 (2020).

34. Sentenac, A. & Chaumet, P. C. "Subdiffraction light focusing on a grating substrate". *Phys. Rev. Lett.* **101** (2008).

35. Kao, T. S., Jenkins, S. D., Ruostekoski, J. & Zheludev, N. I. "Coherent control of nanoscale light localization in metamaterial: creating and positioning isolated subwavelength energy hot spots". *Phys. Rev. Lett.* **106,** 085501 (2011).

36. Singh, A., Hugall, J. T., Calbris, G. & van Hulst, N. F. "Far-field control of nanoscale hotspots by near-field interference". *ACS Photonics* **7,** 2381–2389 (2020).

37. De Waele, R., Koenderink, A. F. & Polman, A. "Tunable nanoscale localization of energy on plasmon particle arrays". *Nano Lett.* **7,** 2004–2008 (2007).

38. De Hoogh, A., Hommersom, B. & Koenderink, A. F. "Wavelength-selective addressing of visible and near-infrared plasmon resonances for SU8 nanolithography". *Opt. Express* **19,** 11405 (2011).

39. Aeschlimann, M., Bauer, M., Bayer, D., Brixner, T., Cunovic, S., Dimler, F., Fischer, A., Pfeiffer, W., Rohmer, M., Schneider, C., Steeb, F., Struber, C. & Voronine, D. V. "Spatiotemporal control of nanooptical excitations". *Proc. Natl. Acad. Sci.* **107,** 5329–5333 (2010).

40. Zhao, L., Kelly, K. L. & Schatz, G. C. "The extinction spectra of silver nanoparticle arrays: influence of array structure on plasmon resonance wavelength and width". *J. Phys. Chem. B* **107,** 7343–7350 (2003).

41. Weber, W. H. & Ford, G. W. "Propagation of optical excitations by dipolar interactions in metal nanoparticle chains". *Phys. Rev. B* **70,** 125429 (2004).

42. Yurkin, M. & Hoekstra, A. "The discrete dipole approximation: An overview and recent developments". *J. Quant. Spectrosc. Radiat. Transfer* **106,** 558–589 (2007).

43. Chaumet, P. C., Zhang, T. & Sentenac, A. "Fast far-field calculation in the discrete dipole approximation". *J. Quant. Spectrosc. Radiat. Transfer* **165,** 88–92 (2015).

44. Novotny, L. & Hecht, B. *Principles of Nano-Optics* (Cambridge University Press, 2006).

45. García de Abajo, F. J. "Colloquium: Light scattering by particle and hole arrays". *Rev. Mod. Phys.* **79,** 1267–1290 (2007).

46. Chen, Y., Zhang, Y. & Koenderink, A. F. "General point dipole theory for periodic metasurfaces: magnetoelectric scattering lattices coupled to planar photonic structures". *Opt. Express* **25,** 21358 (2017).

47. Debye, P. "Das Verhalten von Lichtwellen in der Nähe eines Brennpunktes oder einer Brennlinie". *Ann. Phys.* **335,** 755–776 (1909).

48. Born, M., Wolf, E., Bhatia, A. B., Clemmow, P. C., Gabor, D., Stokes, A. R., Taylor, A. M., Wayman, P. A. & Wilcock, W. L. *Principles of Optics: Electromagnetic Theory of Propagation, Interference and Diffraction of Light* 7th ed. (Cambridge University Press, 1999).

49. Goubau, G. & Schwering, F. "On the guided propagation of electromagnetic wave beams". *IRE Trans. Antennas Propag.* **9,** 248–256 (1961).

50. Saleh, B. E. A. & Teich, M. C. *Fundamentals of Photonics* 2nd (John Wiley & Sons, Inc., 2007).

51. Schmidt, E. "Zur Theorie der linearen und nichtlinearen Integralgleichungen". *Math. Ann.* **63,** 433–476 (1907).

52. Cheney, W. & Kincaid, D. *Linear Algebra: Theory and Applications* (Jones and Barlett, 2009).

53. Salton, G. & Buckley, C. "Term-weighting approaches in automatic text retrieval". *Inf. Process. Manage.* **24,** 513–523 (1988).

54. Singhal, A. "Modern information retrieval: A brief overview". *Data Eng. Bull.* **24,** 35–43 (2001).

55. Harris, C. R. *et al.* "Array programming with NumPy". *Nature* **585,** 357–362 (2020).

56. Sylvester, J. "LX. Thoughts on inverse orthogonal matrices, simultaneous signsuccessions, and tessellated pavements in two or more colours, with applications to Newton's rule, ornamental tile-work, and the theory of numbers". *Philos. Mag.* **34,** 461–475 (1867).

57. Hadamard, J. "Résolution d'une question relative aux déterminants". *Bull. Sci. Math.* **17,** 240–246 (1893).

58. Brenner, J. & Cummings, L. "The Hadamard maximum determinant problem". *Amer. Math. Monthly* **79,** 626–630 (1972).

59. Pratt, W., Kane, J. & Andrews, H. "Hadamard transform image coding". *Proc. IEEE* **57,** 58–68 (1969).

60. Harwit, M. *Hadamard transform optics* (Academic Press, New York, 1979).

61. Cambareri, V., Rovatti, R. & Setti, G. "Maximum entropy hadamard sensing of sparse and localized signals". in *2014 IEEE International Conference on Acoustics, Speech and Signal Processing (ICASSP)* (2014), 2357–2361.

62. Nocedal, J. & Wright, S. J. *Numerical Optimization* (Springer New York, 2006).

63. Berglund, A. J. & Mabuchi, H. "Tracking-FCS: Fluorescence correlation spectroscopy of individual particles". *Opt. Express* **13,** 8069 (2005).

64. Bakker, R. M., Permyakov, D., Yu, Y. F., Markovich, D., Paniagua-Domínguez, R., Gonzaga, L., Samusev, A., Kivshar, Y., Luk'yanchuk, B. & Kuznetsov, A. I. "Magnetic and electric hotspots with silicon nanodimers". *Nano Lett.* **15,** 2137–2142 (2015).

65. Li, L., Fu, Y., Wu, H., Zheng, L., Zhang, H., Lu, Z., Sun, Q. & Yu, W. "The Talbot effect of plasmonic nanolenses". *Opt. Express* **19,** 19365 (2011).

66. Wang, W., Ramezani, M., Väkeväinen, A. I., Törmä, P., Rivas, J. G. & Odom, T. W. "The rich photonic world of plasmonic nanoparticle arrays". *Mater. Today* **21,** 303–314 (2018).

67. Achanta, V. G. "Plasmonic quasicrystals". *Prog. Quantum Electron.* **39,** 1–23 (2015).

68. Yang, Q., Zhang, X., Li, S., Xu, Q., Singh, R., Liu, Y., Li, Y., Kruk, S. S., Gu, J., Han, J. & Zhang, W. "Near-field surface plasmons on quasicrystal metasurfaces". *Sci. Rep.* **6** (2016).

6

CALIBRATION-BASED OVERLAY SENSING WITH MINIMAL-FOOTPRINT TARGETS

Overlay measurements are a critical part of modern semiconductor fabrication, but overlay targets have not scaled down in the way devices have. In this chapter, we produce overlay targets with very small footprint, consisting of just a few scattering nanoparticles in two separate device layers. Using moiré patterns to deterministically generate many overlay errors on a single chip, we demonstrate successful readout of the relative displacement between the two layers and show that calibration on one realisation of the targets can be used for overlay measurements on subsequent instances. Our results suggest using greater quantities of smaller overlay targets may benefit performance both directly and through finer sampling of deformation.

6.1. INTRODUCTION

Overlay error — the misalignment between different patterned layers on a chip — is a key quantity in wafer metrology [1, 2]. With feature sizes shrinking and the semiconductor industry increasingly focussed on few-nanometre nodes, minimising overlay error is crucial to manufacturing yield and device performance [3–5]. Typical overlay targets consist of a set of one-dimensional gratings [6]. Scatterometry on a full set of these gratings allows reconstruction of two-dimensional overlay error, based on understanding of the scattering properties versus position error [7, 8]. These overlay targets are sized based on their scattering physics and do not scale down with device feature size, leaving overlay targets $20-100\,\mu$m squared in the midst of devices fabricated with nanometre-scale precision. Moreover, the few-nanometre overlay error tolerance in advanced nodes means that non-uniform overlay across a complete wafer becomes highly relevant. Sampling overlay error at just a few positions leaves appreciable uncertainty in the wafer deformation model that predicts overlay at intermediate positions [4, 6]. It could thus be advantageous to implement smaller overlay sensors, which might be placed in more positions to better sample overlay error across the wafer.

In this chapter, we perform overlay error retrieval with targets of minimal footprint: just four nanoparticles, for a target around 400×400 nm^2 in size. Using principal component analysis on angle-resolved intensity patterns, we measure overlay retrieval performance. We investigate the effect of fabrication errors on the reliability of this method by reusing calibration data for overlay measurement on a different device and comparing overlay retrieval error.

6.2. RESULTS

The overlay targets we study consist of plasmonic nanoparticles. Such particles are known to couple strongly to light despite their small size [9, 10], with scattering cross-sections larger than their geometric cross-section. This helps to maximise scattered signal despite the small area. Such particles may be created during patterning steps using metal, but they may otherwise be replaced by resonant particles made out of dielectrics [11]. We use disc-shaped gold nanoparticles of diameter 110 nm and height 40 nm, distributed over two layers: three on corners of a 150 nm square in the bottom layer and another centred on the same square, but in the top layer. The layers are fabricated on a boro-silicate glass substrate. We use electron beam physical vapour deposition to deposit gold over a shadow mask patterned by electron beam lithography. The hard mask is lifted off as a sacrificial layer, leaving the bottom layer of nanoparticles. We apply a spacer layer of 89 nm of commercial spin-on glass (Microresist OrmoComp) and repeat the process to fabricate the top nanoparticle layer. The top layer is coated with an identical layer of spin-on glass to avoid reflections near the focal plane. This four-nanoparticle design can show significant chiral optical response and has been proposed as a plasmonic 'ruler' as the three-dimensional arrangement strongly modifies optical spectra [12]. Such spectral tuning through spatial configuration has been demonstrated in arrays of a larger-scale variant of these structures in the infrared [12]. The four-fold asymmetry in the design makes the design polarisation-sensitive, which we exploit in chapter 7. Two realisations of these overlay targets are shown in figure 6.1a and 6.1b, as imaged by scanning electron microscopy. As overlay error in

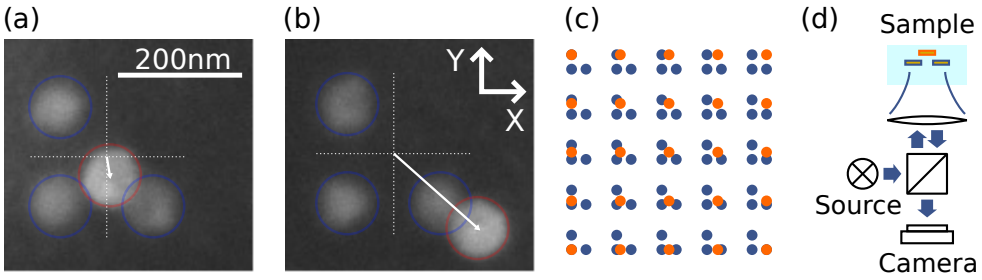

Figure 6.1: (a) Scanning electron image of a minimal-footprint overlay target with small overlay error. Particles circled in blue sit in the bottom (far) layer, the particle circled in red sits in the upper (near) layer. (b) Like (a), but with much larger overlay error. (c) Deterministically producing many different overlay values on a single chip using the moiré effect. Distances in this cartoon are not shown to scale: the distance between individual targets is 5 µm compared to the 400 nm width of the individual targets. (d) Basic set-up for measurement of overlay error using angle-resolved intensity data.

this target is the distance between the centre of the circumscribed square of the three bottom particles and the centre position of the top particle, we see that the target in figure 6.1a has moderate overlay error (30 nm) and the target in figure 6.1b has large overlay error (180 nm). We recognise the individual nanoparticles, imaged through the spin-on glass layer. Our goal is then to reliably and efficiently measure the overlay error in these structures.

In order to test these overlay targets over a range of overlay errors, we exploit moiré patterns. We use electron beam lithography to fabricate arrays of both bottom and top components of the target, but with slightly different pitch: 5.0000 µm for the bottom layer and 5.0375 µm for the top layer. This way, we realise individually addressable copies of our overlay target with steps in overlay error of 37.5 nm in both X and Y directions, as visualised schematically in figure 6.1c. Note that in the fabricated devices, the separation between individual overlay targets is more than ten times their width. We will refer to these synthetic overlay errors as overlay values, in order to avoid confusion with the error in measurement of these overlay values. One convenient property of this experimental architecture is that a small overlay error in our fabrication process will simply shift the origin of our overlay reference grid. In experiment, the overlay values in our overlay targets range from −187.5 nm to 187.5 nm in 11 steps along both X and Y, with uniform deviations of up to 15 nm for separate arrays. This fabrication process deterministically provides us with targets with different overlay values, on which we may test overlay retrieval techniques.

In order to determine overlay value, we collect angle-resolved intensity data. We illuminate the targets with supercontinuum laser light (NKT Whitelase Micro) filtered down to a 10 nm band around 620 nm. The effective numerical aperture of the illuminating beam is $NA_{in} = 0.37$, which produces a focal spot significantly wider than the overlay targets. This reduces the sensitivity of the experiment on the nanometre-scale positioning of the overlay target with respect to the laser spot. We collect the back-scattered light over a numerical aperture of $NA_{out} = 0.95$ through the same objective. The angle-resolved intensity distribution is projected onto a camera, as shown schematically in figure 6.1d. We use a standard CMOS camera (Basler acA1920-40um) at an integration time of 40 ms, which

is comparable with common practice in overlay metrology [6]. We disregard the central $NA_{in} = 0.37$ that corresponds to specular reflection, instead looking at the light scattered out of this cone by the overlay targets. Two of the scattering patterns thus collected are shown in figure 6.2a. The images correspond to overlay values of around −180 nm (top) and 190 nm (bottom) along the X axis. We see that the scattering patterns are clearly different and show beaming along the axis between different particles, in line with the literature on plasmonic phased array experiments [13, 14]. These scattering patterns are to be mapped to overlay value.

We retrieve overlay value from angle-resolved intensity data by the same calibration-based method developed and applied in chapters 3 and 4, where it was used to retrieve the position of light sources and scattering objects. By this method, we collect scattering patterns for all the overlay values available in the moiré pattern. We then use singular value decomposition, a tool from principal component analysis, to identify patterns in the relation between overlay value and scattering pattern. Singular value decomposition finds a linear basis for the set of intensity images, such that the total weight of each successive element in the basis is maximal [15]. For many problems, this permits compression of the reference dataset, where only the first few, largest-weight elements are preserved with minimal loss in information. In figure 6.2b, we show the first six angle-resolved linear basis elements (round patterns, red-blue) and the corresponding weight each element has at the different overlay values (square patterns, green-purple). The bottom-layer nanoparticles are drawn for scale. From this perspective, overlay value corresponds to the position of the fourth, top-layer nanoparticle. After the first element, which corresponds to a largely overlay-independent background, we see two basis elements that map almost directly to Y and X overlay value. The latter, the third element, also explains the patterns we saw in figure 6.2a. Further elements encode finer overlay value dependence of scattering patterns. The optimal basis also provides some insight into how these overlay targets work, i.e. to what degree their response is due to near-field interactions between the nanoparticles versus far-field interference by the individual scattering signals of each nanoparticle. Near-field interactions are strongest when particles are close together, with a sharp position dependence. If near-field interactions were the dominant mechanism, we would likewise expect to see a sharp overlay value dependence in the radiation patterns, probably around the points where the top-layer particle sits directly over any of the bottom-layer particles. Instead, the dominant basis elements are nearly linear over the full 350 nm overlay value range. This suggests that the overlay target produces its scattering patterns mostly by single scattering and far-field interference. Calculation of the optimal basis in figure 6.2b constitutes calibration of the overlay target: we now know the overlay value dependence of scattering patterns on this set of devices.

In the first test, we collect the new scattering patterns on the same structures as were used for calibration. Experimental imperfections due to detection noise and optical re-alignment are thus not shared between both data-sets, but fabrication imperfections are. The new patterns are projected onto the optimal basis and we compare the coefficients with the weights found for every overlay value in the reference set. Summing the square of residuals gives a match value at each overlay value. The overlay value corresponding to the largest match is taken as our best estimate of overlay value given the measurement data and the calibration. We perform this procedure at every overlay value and calculate

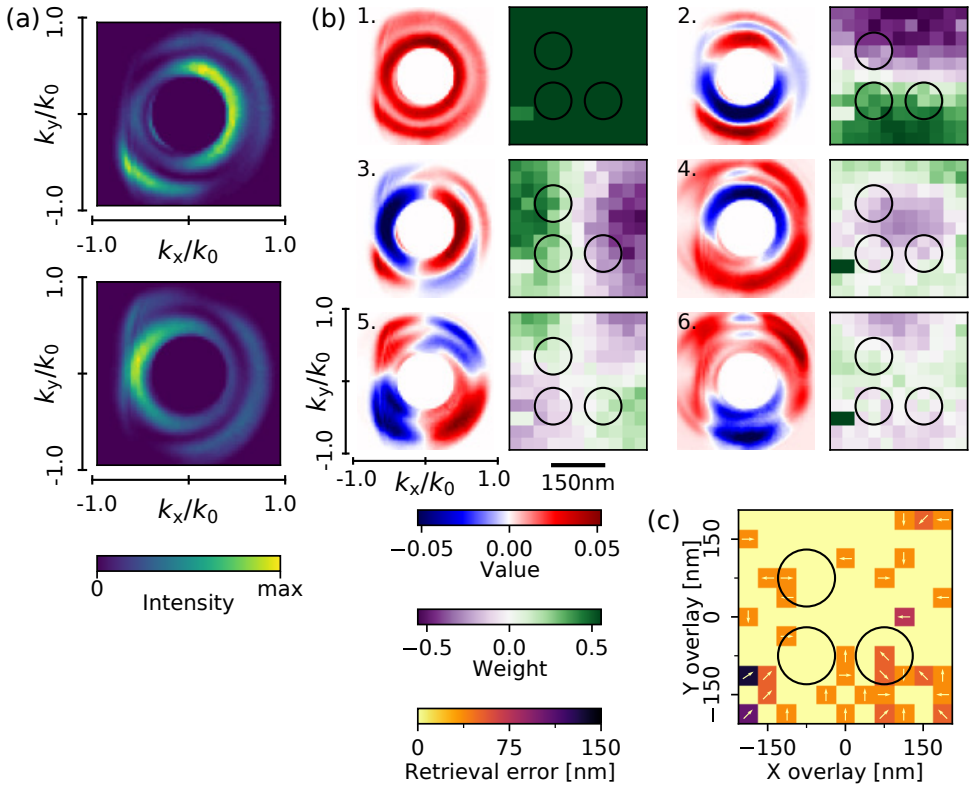

Figure 6.2: (a) Example scattering patterns for overlay targets with overlay values −180 nm (top) and 190 nm (bottom) along the X axis. The scattered light fills a cone of $NA_{out} = 0.95$. The dark region in the centre corresponds to the illumination cone of $NA_{in} = 0.37$. (b) The first six elements of the singular value decomposition of a set of calibration data. Round, red-blue panels show the elements of the linear basis for angle-resolved intensity data and square, green-purple panels show the weight this element holds at each overlay value. Scale bars around element 5 show the extent in momentum space of the basis elements as well as the overlay range covered by the calibration. Black circles mark the size of the overlay target with respect to the calibration area; if these are taken as static, overlay value corresponds to the position of the fourth particle. (c) Retrieving overlay with the calibration data. Overlay retrieval error is calculated for new measurement data, using earlier calibration data from the same device. Where overlay value is not retrieved correctly, arrows indicate in which direction the error is made. Black circles show the scale of the overlay target, as in (b).

the retrieval error: the overlay value difference between the best estimate and the actual known overlay value. The results of this analysis are shown in figure 6.2c. Arrows indicate in which direction the correct overlay value was missed for those cases where it was not retrieved correctly. We see that most overlay values are retrieved correctly, with the size of non-zero retrieval errors mostly a single 37.5 nm step. We can further define an ensemble error ΔOV_e, i.e. the average retrieval error across the entire calibrated domain:

$$\Delta OV_e = \frac{1}{n_x n_y} \sum_{(x,y)} |v_{xy}| \tag{6.1}$$

with v_{xy} the individual retrieval error vectors for all overlay values (x, y) on the $n_x \times n_y$

domain. For these measurements, ensemble error is around $\Delta OV_e = 20\,nm$. We note that these errors are larger than the few-nanometre requirements in advanced nodes. However, this should be considered in the light of the enormous reduction in size, from 100 µm to 400 nm to a side. Although here we show just one realisation, the errors in figure 6.2 do not appear to have a preferred direction, suggesting that combining multiple such sensors could improve performance. It is also conceivable that finer steps in the calibration set would reduce ensemble error. Further investigations might explore whether the source of the error lies in sensitivity to defects, positioning or something else and thus what the practical bounds on retrieval error are. From the available data, we conclude that overlay retrieval with the designed targets works reliably over the 375 nm range.

So far, we have used devices that we had taken calibration data on beforehand. Of course, in overlay metrology, the target is specifically unknown, having been shaped by process variations that it is the purpose of metrology to calibrate. To test this more realistic case, we now reuse the optical calibration data from one device to retrieve overlay value on a separate one with its own fabrication imperfections. Analysing these in the same way as before, we find the results in figure 6.3a. We see that retrieval errors are appreciably larger than with a calibrated device, with ensemble error now around $\Delta OV_e = 60\,nm$. This increase in error is likely due to variability in our fabrication process. Indeed, a main challenge for benchmarking metrology innovations for CMOS technology using prototypes fabricated by e-beam technology, is that e-beam lithography does not reach the reliable fabrication quality of CMOS processing. Due to the small size of the targets, which leaves them vulnerable to nanometre-scale defects, a highly optimised process would be required to ensure reproducibility. To get a better feel for the source of errors, we have repeated our previous measurements, both calibrated on the same device and independently calibrated, on both devices, with different polarisations. We can also treat sample data as calibration data and vice versa. We show all ensemble errors found in this way in figure 6.3b. We see that the calibrated structure consistently outperforms the independently calibrated one, but also that the independently calibrated device consistently obtains an ensemble error around $\Delta OV_e = 65\,nm$. This suggest that the differences between structures may cause a more or less fixed ensemble error level, rather than a wide spread. Of course, measurements on more devices of this type would be needed to further inform our interpretations and verify how non-ideal device fabrication affects overlay retrieval performance.

6.3. DISCUSSION

We have performed two-dimensional overlay retrieval with tiny overlay targets, consisting of just four nanoparticles. Using a moiré grid to deterministically produce a wide range of overlay errors on a single chip, we show overlay retrieval error with mean error around 20 nm on calibrated devices, using tens of millisecond integration times. This performance is obtained by principal component analysis of angle-resolved intensity data, which shows that the main variation in patterns maps nearly linearly to the two spatial axes. Reusing calibration data on separate structures shows overlay retrieval errors around 65 nm, which is clearly larger than on calibrated structures, but nonetheless shows that the unavoidable defects arising from nanoparticle fabrication may be tolerable in overlay metrology.

The overlay targets demonstrate here are much smaller than typical overlay targets. Of course, larger overlay targets do provide stronger scattering signal, besides the added

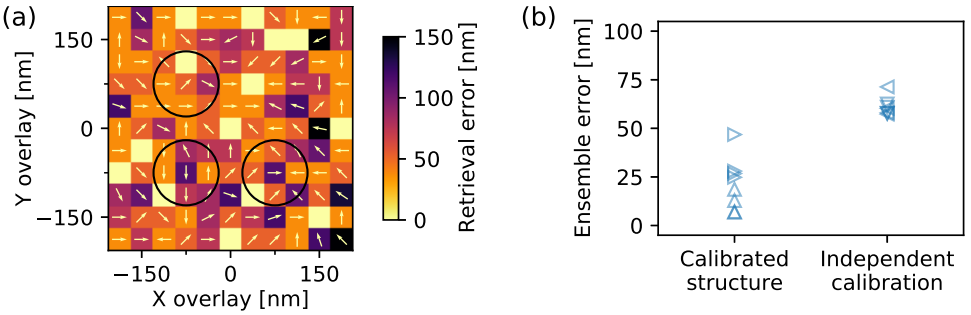

Figure 6.3: (a) Overlay retrieval with independent calibration data, shown like figure 6.2c. (b) Overlay retrieval performance across measurements, either using a fully calibrated device or retrieving overlay through independent calibration data. Differently oriented triangles correspond to different polarisations.

benefit of diffraction orders, which will affect the accuracy with which overlay error can be measured. This may be part of the reason why the current demonstration does not meet the commercial few-nanometre requirement. For the measurements with independent calibration, another reason may be sought in fabrication errors. The fabrication process employed is known to produce errors in particle size and shape that cause variance in scattering properties [16]. We fully expect that the carefully controlled fabrication processes used in the semiconductor industry will drastically reduce variability between devices, bringing the ensemble error level for structures with independent calibration much closer to the error level of the fully calibrated devices. If the errors for calibrated structures can be shown to be uncorrelated, as seems to be the case from the data presented here, multiple minimal-footprint targets could be used to bring effective ensemble error down to tolerable levels. With the five order-of-magnitude difference in footprint, this would still represent a major gain in area. Our algorithm exclusively used angle-resolved intensity data to retrieve overlay. It is worth asking how the performance of this readout scheme compares to use of spectral information, as performed elsewhere [12], or use of other far-field degrees of freedom like polarisation. Optimal far-field measurement schemes remain a fascinating target for further research.

Our minimal-footprint targets seem to encode overlay error in radiation patterns through far-field interference, rather than through more strongly position-dependent multiple scattering mechanisms. With this in mind, it is interesting to ask how more precise overlay sensors may be designed for a given measurement [17, 18]. One path could be to exploit phenomena with a stronger position dependence, such as plasmonic coupling between individual nanoparticles [19] or molecular ruler-like systems [20]. Overlay sensors are typically made, by necessity, out of the same material as the layers between which overlay error is to be measured. This means that metallic particles, as used here, can only be used in part of overlay applications. For others, dielectric (gap) resonators [11] may be a good alternative, especially seeing how our technique does not appear to require multiple scattering between overlay target elements. As device features continue to shrink and overlay metrology becomes increasingly vital to process yield, we expect that innovation in overlay targets will prove critical.

REFERENCES

1. Silver, R. M., Potzick, J. E. & Larrabee, R. D. "Overlay measurements and standards". in *Integrated Circuit Metrology, Inspection, and Process Control IX* (ed Bennett, M. H.) (SPIE, 1995).
2. Bunday, B. "HVM metrology challenges towards the 5nm node". in *Metrology, Inspection, and Process Control for Microlithography XXX* (eds Sanchez, M. I. & Ukraintsev, V. A.) (SPIE, 2016).
3. Felix, N. M., Gabor, A. H., Menon, V. C., Longo, P. P., Halle, S. D., Koay, C.-s. & Colburn, M. E. "Overlay improvement roadmap: strategies for scanner control and product disposition for 5-nm overlay". in *Metrology, Inspection, and Process Control for Microlithography XXV* (ed Raymond, C. J.) (SPIE, 2011).
4. Bunday, B. D., Bello, A., Solecky, E. & Vaid, A. "7/5nm logic manufacturing capabilities and requirements of metrology". in *Metrology, Inspection, and Process Control for Microlithography XXXII* (eds Adan, O. & Ukraintsev, V. A.) (SPIE, 2018).
5. Orji, N. G., Badaroglu, M., Barnes, B. M., Beitia, C., Bunday, B. D., Celano, U., Kline, R. J., Neisser, M., Obeng, Y. & Vladar, A. E. "Metrology for the next generation of semiconductor devices". *Nat. Electron.* **1,** 532–547 (2018).
6. Den Boef, A. J. "Optical wafer metrology sensors for process-robust CD and overlay control in semiconductor device manufacturing". *Surf. Topogr.: Metrol. Prop.* **4,** 023001 (2016).
7. Bishop, K. P., Gaspar, S. M., Milner, L.-M., Naqvi, S. S. H. & McNeil, J. R. "Grating line shape characterization using scatterometry". in *International Conference on the Application and Theory of Periodic Structures* (eds Lerner, J. M. & McKinney, W. R.) (SPIE, 1991).
8. Bouwhuis, G. & Wittekoek, S. "Automatic alignment system for optical projection printing". *IEEE Trans. Electron Devices* **26,** 723–728 (1979).
9. Van Dijk, M. A., Tchebotareva, A. L., Orrit, M., Lippitz, M., Berciaud, S., Lasne, D., Cognet, L. & Lounis, B. "Absorption and scattering microscopy of single metal nanoparticles". *Phys. Chem. Chem. Phys.* **8,** 3486 (2006).
10. Weber, W. H. & Ford, G. W. "Propagation of optical excitations by dipolar interactions in metal nanoparticle chains". *Phys. Rev. B* **70,** 125429 (2004).
11. Kivshar, Y. "All-dielectric meta-optics and non-linear nanophotonics". *Natl. Sci. Rev.* **5,** 144–158 (2018).
12. Hentschel, M., Schäferling, M., Weiss, T., Liu, N. & Giessen, H. "Three-dimensional chiral plasmonic oligomers". *Nano Lett.* **12,** 2542–2547 (2012).
13. Li, J., Salandrino, A. & Engheta, N. "Shaping light beams in the nanometer scale: A Yagi-Uda nanoantenna in the optical domain". *Phys. Rev. B* **76,** 245403 (2007).
14. Koenderink, A. F. "Plasmon nanoparticle array waveguides for single photon and single plasmon sources". *Nano Lett.* **9,** 4228–4233 (2009).
15. Jolliffe, I. T. *Principal Component Analysis* (Springer-Verlag, 2002).

16. Karst, J., Strohfeldt, N., Schäferling, M., Giessen, H. & Hentschel, M. “Single Plasmonic Oligomer Chiral Spectroscopy”. *Adv. Opt. Mater.* **6,** 1800087 (2018).

17. Adel, M., Ghinovker, M., Golovanevsky, B., Izikson, P., Kassel, E., Yaffe, D., Bruckstein, A., Goldenberg, R., Rubner, Y. & Rudzsky, M. “Optimized overlay metrology marks: theory and experiment”. *IEEE Trans. Semicond. Manuf.* **17,** 166–179 (2004).

18. Röhrich, R., Oliveri, G., Kovaios, S., Tenner, V. T., den Boef, A. J., Overvelde, J. T. B. & Koenderink, A. F. “Uncertainty estimation and design optimization of 2D diffraction-based overlay metrology targets”. *ACS Photonics* **7,** 2765–2777 (2020).

19. Sönnichsen, C., Reinhard, B. M., Liphardt, J. & Alivisatos, A. P. “A molecular ruler based on plasmon coupling of single gold and silver nanoparticles”. *Nat. Biotechnol.* **23,** 741–745 (2005).

20. Weiss, S. “Fluorescence spectroscopy of single biomolecules”. *Science* **283,** 1676–1683 (1999).

7

INFORMATION ADVANTAGE FROM POLARISATION-MULTIPLEXED READOUT OF NANOPHOTONIC SCATTERING SENSORS

Optical metrology is an important tool in industry and science, with the goal of retrieving parameters accurately at maximum speed and minimum photon budget. We explore how multiplexing readout across different polarisation channels can enhance such parameter retrieval in nanophotonic overlay sensors. We retrieve overlay error for nanoscale scattering structures and show that multiplexing either incident or analysed polarisation leads to improved parameter retrieval in the systems studied, with improvements equivalent to more than 7 dB *in signal level at fixed photon budget. These results demonstrate that significant advantages in measurement performance of nano-optical sensors can be gained by exploiting the vectorial nature of optical fields.*

7.1. INTRODUCTION

Advancements in overlay and critical dimension metrology are critical enablers of continued scaling in the modern semiconductor industry [1–3]. The strong desire for inspection to match the throughput of other process steps [4] has led to the dominance of optical methods, which generally work more quickly than scanning probes [5, 6] or electron beam based methods [7, 8]. As such, these is great pressure for non-contact optical inspection methods to evolve beyond the current state of the art [9–11]. With process requirements growing ever more stringent [12, 13], the various optical critical dimension measurement techniques, using polarimetry, ellipsometry, interferometric scatterometry and more [10, 14–17] need to grow faster and more precise.

Polarisation effects are known to affect signals in many ways and are frequently exploited in metrology, with Mueller polarimetry, which resolves the full 4×4 matrix that describes polarisation transfer through a sample [18, 19], an established technique in semiconductor metrology [13, 20]. The power of polarimetry is further enhanced when combined with other information channels, for instance as in angle-resolved polarimetry [21]. However, full polarimetry is a large investment in terms of experimental complexity. Full high-NA angle-resolved polarimetry and characterisation of the polarisation transfer function of a sample both require a complex series of measurements. In the case of sample metrology, it typically requires careful calibration of the optical set-up and a detailed theoretical model of the structure of interest. It is worth considering if polarisation information can be used in metrology in a more straightforward way, without recovering the full Mueller matrix, which requires at least 16 measurements, but simply by measuring more than one polarisation channel and combining the information thus collected.

In this chapter, we show that for a given photon budget, more precise overlay information can be extracted from a scattering target by polarisation multiplexing than from unpolarised measurements. We measure overlay error on few-nanoparticle scattering overlay sensors and aim to optimise measurement precision. We consider several strategies for multiplexing light polarisation in input and output channels. Applying a calibration-based method to retrieve overlay from devices with a wide range of overlay errors, we compare the performance of the different strategies to quantify the information gained by combining polarisation channels. We explore the dependence of performance improvement on photon budget through a discrete dipole model and analyse both theoretically and in experiment how overlay performance for different strategies relates to wavevector resolution. Finally, we discuss how combining information from different polarisation channels may benefit nano-optical sensing more broadly.

7.2. METHOD

We study polarisation multiplexing by applying it to overlay measurement. In overlay measurement, we consider two layers of a sample that have a small but unknown in-plane displacement with respect to the design, as a result of fabrication tolerances. The challenge is to measure this displacement, known as the overlay error. We use the same overlay targets employed in chapter 6. These overlay targets have an exceptionally small footprint of only 400 nm to a side, consisting of four nominally identical gold discs of thickness 40 nm and diameter 110 nm. Such particles have a plasmonic resonance at a wavelength around

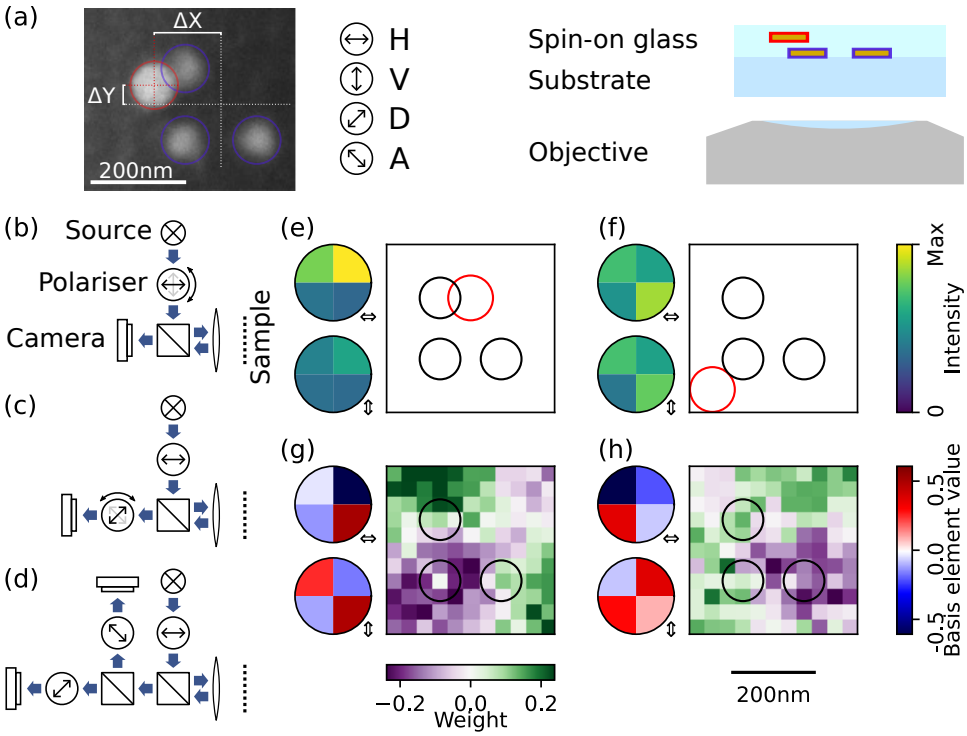

Figure 7.1: (a) Device structure. Left: electron image showing overlay error on an overlay target: zero overlay occurs when the red cross, centred on the red-circled particle, overlaps with the white cross, centred between the blue-circled particles. Circled arrows define the polarisation axes in the same XY frame as the electron image. Right: schematic cross-section of device, showing arrangement of layers and objective. (b)-(d) Three strategies for polarisation multiplexed measurement, either (b) changing an input polariser between measurements, (c) changing an analysis polariser between measurements or (d) reading out two polarisation channels in parallel. (e)-(f) Example measurements using quadrant detectors in two input polarisation channels. Circular panels show detector pixel intensities, square panels show the relative arrangement of particles that produced this reading. (g)-(h) Two entries from the singular value decomposition of a full reference set for 11×11 overlay values. Circular panels show pixel intensity components corresponding to this basis element, square panels show the weight this basis element has for each position of the fourth particle.

700 nm, around which frequency they strongly scatter incident light. We use a layout with three particle in the bottom layer, arranged in an L-shape, and a solitary particle in the top layer, all embedded in commercial spin-on glass (MicroResist Ormocomp) with the layers separated by 89 nm (more details in chapter 6). This system is studied optically from below, as sketched in figure 7.1a. The overlay error in this target is the distance between the midpoint between opposite particles in the bottom layer and the midpoint of the particle in the top layer. The relevant displacements and axes are indicated on a scanning electron image of one such structure in figure 7.1a. This design breaks the symmetry between some of the axes, such as D and A, without breaking that between H and V unless the top-layer particle does so. This may lead to some polarisations, or combinations thereof, providing more sensitive overlay measurements than others. We fabricate such targets with

a wide range of relative displacements. Devices lie on a grid where both X and Y overlay nominally range from −187.5 nm to 187.5 nm in 37.5 nm steps (see chapter 6). Fabrication produced a constant offset of around 15 nm and nanometre-scale fabrication errors on top of that. The calibration-based measurement method we will use is not affected by these non-idealities. We will refer to these engineered overlay errors as overlay values. The grid allows us to verify our overlay measurement performance over this entire parameter range and compare the different readout strategies.

There are several feasible strategies for measuring complementary polarisation channels for a static sample structure. In the first we consider polarising a beam of light before directing it to a sample. The reflected (or transmitted) light is captured on a detector, possibly but not necessarily after focussing. By rotating the input polariser, the sample response to light of complementary polarisations may be measured separately, as sketched in figure 7.1b. Both independent measurements can then be used together to address the overlay problem. We refer to this approach as input polarisation multiplexing. Alternatively, the sample may be illuminated with light of a fixed polarisation, or with unpolarised light, which is analysed along different polarisation axes. This analysis may be performed in series by rotating an analyser, in analogy with the input polarisation multiplexing scenario, as sketched in figure 7.1c. Alternatively, both channels may be measured at once by employing a beam splitter and two analysers or a polarising beam splitter, as sketched in figure 7.1d. The latter two strategies, which we refer to as output polarisation multiplexing, are equivalent in the case of static samples, but either may have practical advantages over the other. We wish to explore how input and output polarisation multiplexing compare to standard approaches that use a single fixed polarisation or unpolarised light, as well as to each other.

In our measurements, we collect radiation patterns in the form of Fourier images representing radiant flux versus parallel wavevector (k_x, k_y) up to the numerical aperture of our objective $NA_{out} = 0.95$. The sample is illuminated with $NA_{in} = 0.37$ and the part of the Fourier images corresponding to specular reflection of the illuminating light is blocked. We will mostly consider measurements made with an effective quadrant (four-pixel) detector, with the radiation pattern centred on the detector, so that all pixels show equal intensity in the case of a symmetric radiation pattern. We implement such a detector experimentally by projecting Fourier images onto a higher-resolution camera (Basler ACA1920-40UM) and integrating the counts in each quadrant of the observed back focal plane image. This produces four pixel values per measurement in the case of traditional single-polarisation measurements and eight in polarisation-multiplexed cases. Experimental details are otherwise as in chapter 6. We collect far-field data for the full grid of overlay values available on the sample. Two example measurements for different overlay values are shown in figure 7.1e and 7.1f. Circular panels show intensity on each segment of the quadrant detectors for horizontal (top) and vertical (bottom) polarisation.

The measured intensities are the result of an interplay of scattering events within the device that, for ideal devices, we might be able to predict by any number of theoretical methods. Though we will use a discrete dipole approximation to qualitatively study some of the behaviours of the devices, for actual overlay retrieval we opt for a calibration-based method. Unlike forward theoretical modelling, such calibration-based methods handle realistic fabrication artefacts and parasitic reflections without complication. The

calibration-based method we use to extract overlay value from far-field data was previously used to localise point-like light sources (chapter 3) and scattering objects (chapter 4). It requires one reference measurements per resolvable value in the calibrated domain. In this case, this means one measurement for each overlay value in the sample grid. Each such measurement is used as a row in a signals matrix A. Singular value decomposition finds the optimal basis for a set of measurements, as discussed in chapter 3 and specifically for this type of data in chapter 6.

Two elements of such an optimal basis, from the singular value decomposition of the data collected on the full grid before, are shown in figures 7.1g and 7.1h. Circular panels show the value of the basis elements at each pixel for either polarisation. Square panels show the weight these basis elements have at each position in the reference set. There are as many basis elements as pixels, but only a few have appreciable weight anywhere. The examples shown are interesting because they have large weight, but also a smooth dependence of weight on position, with broad, contiguous regions of positive or negative weight. Importantly, each of the basis elements has different pixel values for the two polarisation channels. This means that being able to resolve the polarisation channels may provide additional information: there is a difference that would have washed out in a single-polarisation or unpolarised light measurement.

7.3. RESULTS

We use this calibration-based method to reconstruct overlay from new data. In order to illustrate the qualitative behaviour of the method, we first turn to a theoretical model. We use a discrete dipole approximation, where the overlay target is modelled as four point scatterers of polarisability $|\alpha| = 5.56 \times 10^{-33}\,\mathrm{C\,m^2\,V^{-1}}$ and a quality factor $Q = 10$ in a homogeneous medium. As discussed in section 2.2, discrete dipole models let us quickly estimate the qualitative behaviour of sets of interacting particles [22–25], taking into account multiple scattering, self-action and retardation [26, 27]. We can calculate far-field data on quadrant detectors and analyse them in much the same way as for the experimental data. We specifically include synthetic shot noise for the appropriate photon budget, around $N = 10^6$, which corresponds to the integrated intensity over all pixels in all measured polarisation channels. We can calculate far-field data for a large grid of overlay values, 2λ in 31 steps to a side, and take their singular value decomposition. For newly calculated data, with independent noise, we project these new data onto the optimal basis and compare the coefficients with those for the reference positions through the least square of residuals. The reference position corresponding to the best match is taken as the overlay value estimate. In figure 7.2a we show the error in such estimates for one full set of newly generated test data using input polarisation multiplexing, projected onto the optimal basis. Some patterns can be seen in these noisy data, with retrieval errors largest in the corners and along the symmetry axes of the quadrant diode. We can average many (n_i) instances to find an average error $\Delta\mathrm{OV_a}$ at some overlay value (x, y):

$$\Delta\mathrm{OV}_{\mathrm{a},xy} = \frac{1}{n_i}\sum_i |v_i| \tag{7.1}$$

where v_i are the individual error vectors between the estimated and correct overlay value, for each instance i. Averaging 300 instances of the error map from figure 7.2a, with different

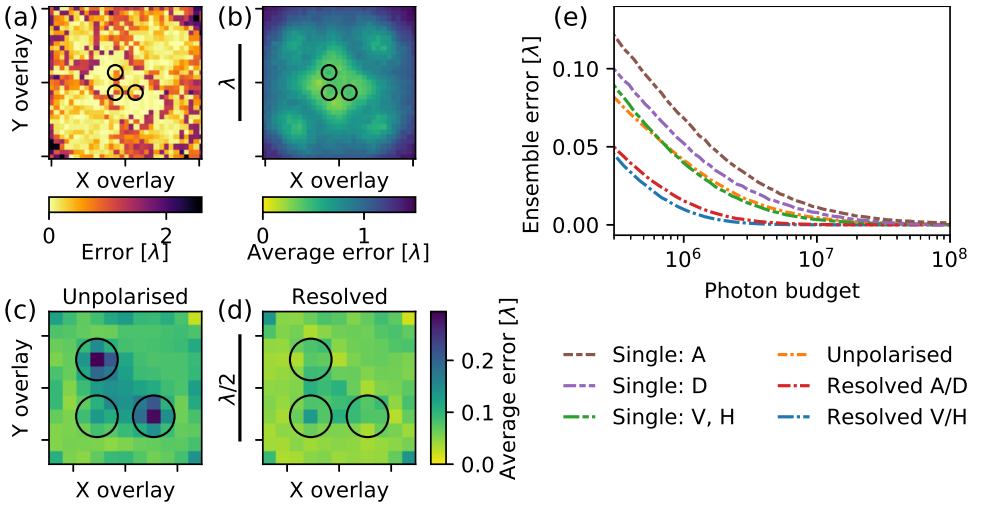

Figure 7.2: Overlay retrieval in theoretical input polarisation multiplexing. (a) Overlay retrieval error versus overlay value for one set of noisy synthetic data. (b) Average error versus overlay value for the scenario used in (a). (c-d) Average error versus position for experimentally relevant library dimensions, for (c) unpolarised detection and (d) H-V polarisation resolved detection. (e) Ensemble error versus photon budget for a range of polarisation strategies, with library dimensions as in (c).

noise realisations, produces the average error map in 7.2b. We see some fine structure in average error versus overlay, but mainly that overlay performance is best for small overlay value. We can now rephrase our original challenge: we intend to find out if and how such average error maps improve with the introduction of polarisation multiplexing at constant total photon budget.

We first test input polarisation multiplexing in theory. We consider the same overlay values available in experiment and calculate average error for two polarisation strategies: unpolarised light and input polarisation multiplexing between H and V polarisation (as defined in figure 7.1) for the same total photon budget (integration time). The consideration of constant photon budget means that any advantage of multiplexing would imply that the incorporation of another polarisation channel is more valuable to overlay retrieval than averaging twice as long in a single polarisation channel. We calculate average error versus overlay and, as can be seen in figures 7.2c and 7.2d, average error is appreciably lower with polarisation resolution than without. In some cases, polarisation resolution appears to allow distinguishing between some non-unique solutions, like directly below the outer particles in the bottom layer. Nearly all positions show an improvement in average error and it is conceivable that all would with more averaging. We can further analyse these data by averaging the error maps across all overlay values to produce an ensemble error $\Delta\mathrm{OV_e}$:

$$\Delta\mathrm{OV_e} = \frac{1}{n_x n_y} \sum_{(x,y)} \Delta\mathrm{OV_{a},}_{xy} \tag{7.2}$$

for all $n_x \times n_y$ pairs of overlay value (x, y) in the library. This ensemble error depends on the size and density of the library, but may be compared with ensemble errors for

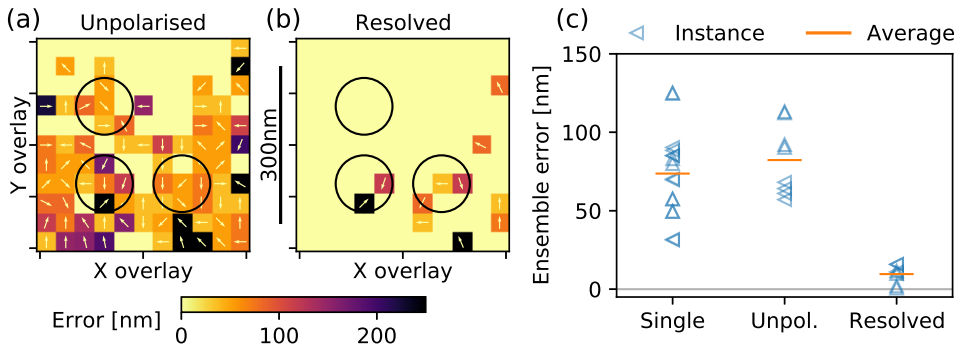

Figure 7.3: Overlay retrieval in experimental input polarisation multiplexing. (a-b) Overlay retrieval error for (a) unpolarised detection and (b) H-V polarisation resolved detection. Dimensions are the same as in figure 7.2(c). (c) Ensemble error for experimental data versus polarisation strategy: a single fixed polarisation, unpolarised illumination and detection and resolved orthogonal polarisation channels. Differently oriented triangles correspond to different devices under test, averages are calculated across all data for a given polarisation strategy.

libraries with the same dimensions. The ensemble error for given library dimensions will be a function not only on the polarisation multiplexing strategy used, but also of the available photon budget. We calculate this ensemble error over a range of photon budgets and for the polarisations used before, as well as multiplexing between D and A polarisations and all corresponding single polarisations. The results of these ensemble average calculations, plotted in figure 7.2e, show the two multiplexed strategies drastically outperforming both unpolarised and single-polarisation measurements. As a rule, the V-H polarisation channels and their combinations perform a bit better than the A-D ones, but the difference is small compared to the large advantage from polarisation multiplexing, which corresponds to an effective improvement in photon budget of around 7 dB for photon budgets around 3×10^5: the performance obtained with multiplexed data would otherwise require four times the averaging time.

Due to the nature of the calibration-based method used, average and ensemble errors depend on the size and density of the library. The largest possible average error corresponds to $\sqrt{2}(N-1)$ steps for a square library of $N \times N$ positions. Moreover, even without any signal, we can achieve an ensemble error of only around half the library width by guessing all data were taken at the library centre. This is likely to limit observed ensemble error at very small photon budgets. Our method thus is only valid in the regime of small ensemble errors. Since the results of figure 7.2e are found at ensemble errors that are a small fraction of the width of the library, we expect to be able to observe any differences between polarisation strategies — as indeed we do. This improved performance of the polarisation resolved data in the discrete dipole model indicates that polarisation multiplexed measurement results in a significant improvement in overlay retrieval performance.

By the same approach, we compare the overlay retrieval performance of different polarisation strategies on experimental data. We calculate overlay retrieval error for a new set of measurements on the same structures, using the reference library from figures 7.1g and 7.1h. In figure 7.3a and 7.3b, we show such error maps for unpolarised and V-H resolved measurements, on the same scale as the discrete dipole results in figure 7.2c.

Unlike in the theoretical case, we do not directly recognise the shape or orientation of the overlay target in the data. It is likely that fabrication errors or experimental details dominate the pattern of errors, as both are expected to be large with few-nanoparticle overlay targets. Nonetheless, we see a drastic improvement in overlay retrieval performance from including polarisation information when comparing the unpolarised case to the polarisation-resolved one. We repeat this experiment on different realisations of the same set of structures. When we calculate ensemble error for each set of such measurements, as well as for single-polarisation measurements (the same combinations of polarisations as in theory), we find the results shown in figure 7.3c. These results confirm the improvement in performance: single-polarisation and unpolarised measurements perform similarly, but polarisation-resolved measurements perform much better, with average ensemble error across a series of measurements going from around 70 nm (two library steps) to around 10 nm (a fraction of one library step). This improvement is greater than the improvement found at similar ensemble error in the theoretical results (figure 7.2e). This may be because experimental performance is limited by other sources of error than shot noise, the only noise source included in the theory. The experimental data confirm that input polarisation multiplexing can drastically improve overlay retrieval performance.

We similarly study output polarisation multiplexing. Discrete dipole analysis, using the same library dimensions as in experiment, shows very similar trends as for input polarisation multiplexing. Figure 7.4 shows ensemble error calculated versus photon budget for unpolarised input and readout, single-polarisation input (H or V) and readout along the same polarisation and for unpolarised input with H-V polarisation resolved readout. Like for input polarisation multiplexing, we see that single-polarisation and unpolarised analysis perform similarly, but are outperformed by polarisation-resolved readout. The effective improvement in photon budget is over 7 dB at a photon budget of 10^6. Repeating our earlier experiments with (temporal) output polarisation multiplexing instead of input polarisation multiplexing, we again see a significant improvement going from unpolarised measurements to H-V polarisation resolved ones, as in figures 7.5a and 7.5b. A series of such measurements across different devices (7.5c) show the same trend as the theory: polarisation-resolved analysis significantly outperforms the other strategies, confirming that, like input polarisation multiplexing, output polarisation multiplexing leads to more precise overlay retrieval.

At this point we ask how polarisation channels relate to other possible information channels in causing the observed improvement in performance. We have so far considered quadrant detectors.Instead, we can analyse the calculated or measured radiation patterns at higher resolution in momentum space, keeping the detector pixel grid centred on the centre of Fourier space and covering the same numerical aperture with more pixels. We can calculate the photon budget, i.e. measurement time, required to obtain a certain maximum ensemble error. Several observations may be made about the results of these calculations for output polarisation multiplexing, shown in 7.6a. First, detectors with more pixels allow a given performance to be obtained at lower photon budget than those with fewer pixels. The largest advantage is seen going from just a few pixels to some tens, beyond which the improvements become smaller. This may be related to the number of effective degrees of freedom of the radiation patterns considered: the small size of our overlay targets means that their radiation patterns will be fairly smooth and may be reconstructed from fewer

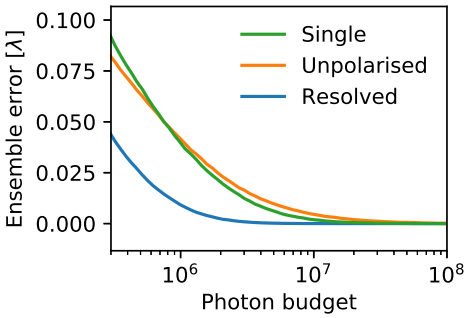

Figure 7.4: Overlay retrieval in theoretical output polarisation multiplexing. Ensemble error calculated as a function of photon budget for a range of polarisation strategies, using a library of the same dimensions as in experiment.

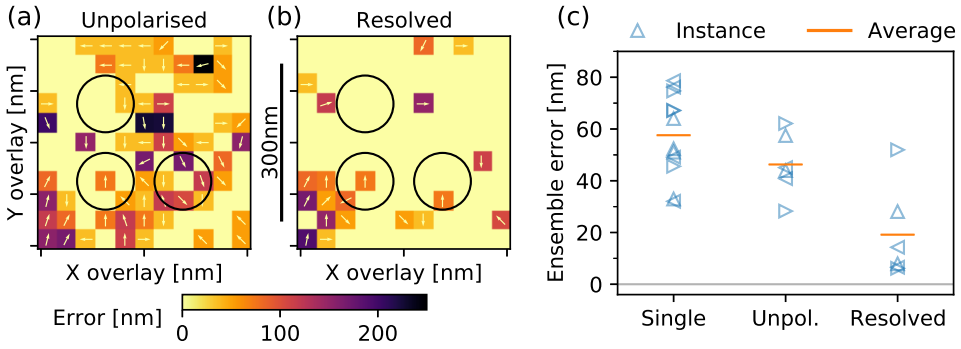

Figure 7.5: Overlay retrieval in experimental output polarisation multiplexing. (a-b) Overlay retrieval error for (a) polarisation-insensitive and (b) polarisation-resolved analysis. (c) Ensemble error for experimental data versus polarisation strategy, shown as in figure 7.3c.

samples than would be needed to reconstruct the radiation patterns of extended structures. Another observation is that the polarisation-resolved photon budget requirements are consistently lower than those for unpolarised measurement. This demonstrates that polarisation multiplexing is advantageous over a wide range of photon budgets and detector resolutions (in pixels).

One way to quantify this advantage is as effective noise reduction: the reduction in measurement time to obtain equal overlay retrieval performance when using (output) polarisation multiplexed analysis instead of unpolarised analysis. We calculate effective noise reduction as a function of initial (unpolarised) photon budget, which is related to ensemble error as per the data in 7.4. This analysis is shown in figure 7.6b. We see that effective noise reduction generally increases with photon budget. Few-pixel detectors are much more helped by polarisation resolution than the high-resolution detectors that permit good overlay retrieval even without polarisation resolution, as we saw from figure 7.6a. Effective noise reduction at 10^6 photons appears to plateau at slightly more than 3 dB for anywhere between tens and thousands of pixels. With lower photon budgets, effective

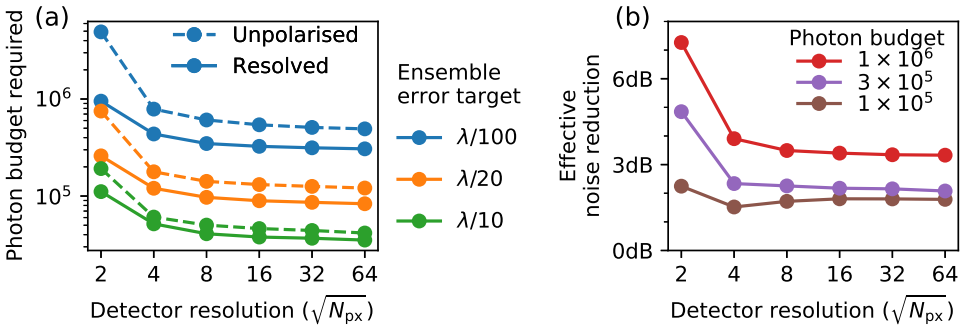

Figure 7.6: Theoretical overlay retrieval performance versus detector resolution. (a) Required photon budget for given maximum ensemble error calculated for different detector resolutions. Solid lines indicate performance with polarisation multiplexing, dashed lines without. (b) Effective noise reduction, the reduction in integration time to achieve a certain maximum ensemble error, calculated at different photon budget as a function of detector resolution. The detector resolution axis represents the number of pixels along one side of a square detector.

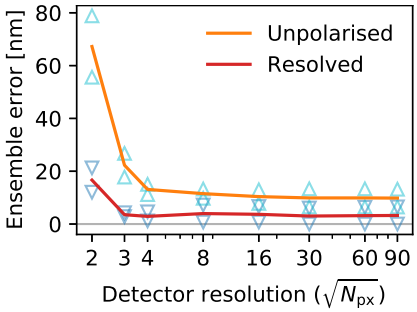

Figure 7.7: Experimental overlay retrieval performance versus detector resolution. Ensemble error as measured with different strategies, plotted versus detector resolution. Triangles show the experimental data averaged to obtain the lines.

noise reduction decreases for all detector resolutions, but more strongly so for few-pixel detectors. These few-pixel detectors are much more error-prone with or without polarisation resolution at these photon budgets, such that noise reduction at a photon budget of 10^5 is nearly independent of detector resolution. The 2 dB effective noise reduction in this regime still corresponds to an appreciable speed-up in measurement time for a given precision.

We can also analyse how greater detector resolution affects experimental overlay retrieval performance. This is implemented experimentally by taking the original high-resolution camera images and dividing the region of interest into smaller superpixels than the quadrants considered before, thus retaining more of the wavevector information in the camera images. In figure 7.7 we show the dependence of ensemble error on detector resolution for unpolarised measurement and output polarisation multiplexed measurement. We see that performance improves rapidly with the number of pixels for small numbers of pixels but then plateaus, matching our expectation that the small scales involved would

lead to broad features in Fourier images. Polarisation resolution with a quadrant detector, for 8 degrees of freedom in total, provides performance between those of non-resolved detection with 9 and 16 degrees of freedom. We thus see that, one-for-one, the additional polarisation-resolved degrees of freedom are more valuable in overlay retrieval than the additional wavevector degrees of freedom. We also see that a polarisation-resolved 3×3 pixel detector outperforms non-resolved detection at many thousands of pixels. The precise numbers and degree of improvement are likely to depend on the details of the scattering problem under study. However, these data show that not all degrees of freedom are equally informative, polarisation proving to be a particularly informative one on scattering systems such as those considered here.

7.4. CONCLUSION AND DISCUSSION

We have explored how combining different polarisation channels may assist parameter retrieval in optical metrology. Our results indicate that combining information from multiple polarisation channels leads to significantly better overlay retrieval performance than standard approaches for few-nanoparticle overlay targets. Pairing different incident light polarisations and pairing different analysis polarisations both provide an improvement in effective photon budget of 7 dB or more, as compared with either unpolarised or single-polarisation illumination and detection. These results are expected from discrete dipole theory, which predicts the advantage will persist over a wide range of photon budgets, and verified using experiments. Comparing polarisation-multiplexed readout with additional degrees of freedom from higher wavevector resolution, we see that polarisation resolution is particularly valuable, with a 3×3 detector with polarisation multiplexing outperforming a non-polarisation-resolved detector with many thousands of pixels.

It seems likely that polarisation multiplexing can help in parameter retrieval not just for our few-particle overlay targets, but for any metrology problem where sample interactions are polarisation-dependent, particularly in such applications as alignment and shape measurement. The technique may be particularly valuable for nanoscale scattering systems, which due to their size cannot encode information in fine features in scattering patterns. It would be interesting to explore which combinations of polarisation channels would provide most information for a given target. Conversely, overlay targets may be designed for maximum sensitivity for given measurement conditions [28, 29]. One may consider a similar multiplexing approach working based not on the polarisation degree of freedom, but for instance on distinct incident wavevectors or wavelengths, all of which may interact differently with samples. Further studies may investigate how these different degrees of freedom interact and complement one another in terms of sample information encoded. Multiplexing strategies like those tested here are particularly attractive because of their simplicity. Output polarisation multiplexing in particular can be performed very easily and at minimal expense, requiring only a polarising beam splitter and twice the camera pixels to introduce. As such, polarisation multiplexing has the potential to enable more precise measurements in a myriad of applications.

REFERENCES

1. Felix, N. M., Gabor, A. H., Menon, V. C., Longo, P. P., Halle, S. D., Koay, C.-s. & Colburn, M. E. "Overlay improvement roadmap: strategies for scanner control and product disposition for 5-nm overlay". in *Metrology, Inspection, and Process Control for Microlithography XXV* (ed Raymond, C. J.) (SPIE, 2011).
2. Yoo, G., Kim, J., Park, C., Lee, T., Ji, S., Jo, G., Yang, H., Yim, D., Yamamoto, M., Maruyama, K. & Park, B. "Real cell overlay measurement through design based metrology". in *Metrology, Inspection, and Process Control for Microlithography XXVIII* (eds Cain, J. P. & Sanchez, M. I.) (SPIE, 2014).
3. Kuiper, S., Fritz, E., Crowcombe, W., Liebig, T., Kramer, G., Witvoet, G., Duivenvoorde, T., Overtoom, T., Rijnbeek, R., van Zwet, E., van Dijsseldonk, A., den Boef, A., Beems, M. & Levasier, L. "Large dynamic range Atomic Force Microscope for overlay improvements". in *Metrology, Inspection, and Process Control for Microlithography XXX* (eds Sanchez, M. I. & Ukraintsev, V. A.) (SPIE, 2016).
4. Crimmins, T. F. "Defect metrology challenges at the 11-nm node and beyond". in *Metrology, Inspection, and Process Control for Microlithography XXIV* (ed Raymond, C. J.) (SPIE, 2010).
5. Yao, T.-F., Connolly, L. G. & Cullinan, M. "Expanded area metrology for tip-based wafer inspection in the nanomanufacturing of electronic devices". *J. Micro/Nanolithogr., MEMS, MOEMS* **18,** 1 (2019).
6. Bunday, B. "HVM metrology challenges towards the 5nm node". in *Metrology, Inspection, and Process Control for Microlithography XXX* (eds Sanchez, M. I. & Ukraintsev, V. A.) (SPIE, 2016).
7. Vladár, A. E., Villarrubia, J. S., Chawla, J., Ming, B., Kline, J. R., List, S. & Postek, M. T. "10nm three-dimensional CD-SEM metrology". in *Metrology, Inspection, and Process Control for Microlithography XXVIII* (eds Cain, J. P. & Sanchez, M. I.) (SPIE, 2014).
8. Levi, S., Schwarzban, I., Karvtsov, A., Tobayas, M., Stock, H.-J., Muelders, T., Hand, S. & Osborne, J. "3D optical proximity model optimization using inline 3DSEM metrology". in *Metrology, Inspection, and Process Control for Microlithography XXXIII* (eds Adan, O. & Ukraintsev, V. A.) (SPIE, 2019).
9. Vanoppen, P., Theeuwes, T., Megens, H., Cramer, H., Fliervoet, T., Ebert, M. & Satriasaputra, D. "Lithographic scanner stability improvements through advanced metrology and control". in *Optical Microlithography XXIII* (eds Dusa, M. V. & Conley, W.) (SPIE, 2010).
10. Bhattacharyya, K. "New approaches for scatterometry-based metrology for critical distance and overlay measurement and process control". *J. Micro/Nanolithogr., MEMS, MOEMS* **10,** 013013 (2011).
11. Benschop, J., Engelen, A., Cramer, H., Kubis, M., Hinnen, P., van der Laan, H., Bhattacharyya, K. & Mulkens, J. "Integrated scatterometry for tight overlay and CD control to enable 20-nm node wafer manufacturing." in *Optical Microlithography XXVI* (ed Conley, W.) (SPIE, 2013).

12. Bunday, B., Solecky, E., Vaid, A., Bello, A. F. & Dai, X. “Metrology capabilities and needs for 7nm and 5nm logic nodes”. in *Metrology, Inspection, and Process Control for Microlithography XXXI* (eds Sanchez, M. I. & Ukraintsev, V. A.) (SPIE, 2017).

13. Bunday, B. D., Bello, A., Solecky, E. & Vaid, A. “7/5nm logic manufacturing capabilities and requirements of metrology”. in *Metrology, Inspection, and Process Control for Microlithography XXXII* (eds Adan, O. & Ukraintsev, V. A.) (SPIE, 2018).

14. Kumar, N., Petrik, P., Ramanandan, G. K. P., Gawhary, O. E., Roy, S., Pereira, S. F., Coene, W. M. J. & Urbach, H. P. “Reconstruction of sub-wavelength features and nano-positioning of gratings using coherent Fourier scatterometry”. *Opt. Express* **22,** 24678 (2014).

15. Chen, X., Liu, S., Zhang, C. & Jiang, H. “Measurement configuration optimization for grating reconstruction by Mueller matrix polarimetry”. in *Metrology, Inspection, and Process Control for Microlithography XXVII* (eds Starikov, A. & Cain, J. P.) (SPIE, 2013).

16. Holden, J. M., Gubiotti, T., McGahan, W. A., Dusa, M. V. & Kiers, T. “Normal-incidence spectroscopic ellipsometry and polarized reflectometry for measurement and control of photoresist critical dimension”. in *Metrology, Inspection, and Process Control for Microlithography XVI* (ed Herr, D. J. C.) (SPIE, 2002).

17. Madsen, M. H. & Hansen, P.-E. “Scatterometry—fast and robust measurements of nano-textured surfaces”. *Surf. Topogr.: Metrol. Prop.* **4,** 023003 (2016).

18. Roy-Brehonnet, F. L. & Jeune, B. L. “Utilization of Mueller matrix formalism to obtain optical targets depolarization and polarization properties”. *Prog. Quantum Electron.* **21,** 109–151 (1997).

19. Aiello, A., Puentes, G., Voigt, D. & Woerdman, J. P. “Maximum-likelihood estimation of Mueller matrices”. *Opt. Lett.* **31,** 817 (2006).

20. Fallet, C. “Overlay measurements by Mueller polarimetry in back focal plane”. *J. Micro/Nanolithogr., MEMS, MOEMS* **10,** 033017 (2011).

21. Mohtashami, A., Osorio, C. I. & Koenderink, A. F. “Angle-resolved polarimetry of antenna-mediated fluorescence”. *Phys. Rev. Appl.* **4** (2015).

22. Zhao, L., Kelly, K. L. & Schatz, G. C. “The extinction spectra of silver nanoparticle arrays: influence of array structure on plasmon resonance wavelength and width”. *J. Phys. Chem. B* **107,** 7343–7350 (2003).

23. Weber, W. H. & Ford, G. W. “Propagation of optical excitations by dipolar interactions in metal nanoparticle chains”. *Phys. Rev. B* **70,** 125429 (2004).

24. Yurkin, M. & Hoekstra, A. “The discrete dipole approximation: An overview and recent developments”. *J. Quant. Spectrosc. Radiat. Transfer* **106,** 558–589 (2007).

25. Chaumet, P. C., Zhang, T. & Sentenac, A. “Fast far-field calculation in the discrete dipole approximation”. *J. Quant. Spectrosc. Radiat. Transfer* **165,** 88–92 (2015).

26. Novotny, L. & Hecht, B. *Principles of Nano-Optics* (Cambridge University Press, 2006).

27. García de Abajo, F. J. "Colloquium: Light scattering by particle and hole arrays". *Rev. Mod. Phys.* **79,** 1267–1290 (2007).

28. Adel, M., Ghinovker, M., Golovanevsky, B., Izikson, P., Kassel, E., Yaffe, D., Bruckstein, A., Goldenberg, R., Rubner, Y. & Rudzsky, M. "Optimized overlay metrology marks: theory and experiment". *IEEE Trans. Semicond. Manuf.* **17,** 166–179 (2004).

29. Röhrich, R., Oliveri, G., Kovaios, S., Tenner, V. T., den Boef, A. J., Overvelde, J. T. B. & Koenderink, A. F. "Uncertainty estimation and design optimization of 2D diffraction-based overlay metrology targets". *ACS Photonics* **7,** 2765–2777 (2020).

8

CONCLUSION

Over the course of this thesis, we have seen that Fourier images encode nanoscopic near-field information. The library-based method developed in chapter 3 retrieves such nanoscopic information reliably, successfully localising light sources and both microscopic and macroscopic scatterers (chapters 4, 6 and 7). It is also robust to perturbations and noise, with potential for compression of the calibration dataset. It is, however, limited to discretised libraries and a correspondingly finite set of possible parameter values. This contrasts with analytical models, which describe far-field scattering patterns as a continuous function of scattering parameters like relative position. Such models lend themselves to a different type of analysis: exploiting a quantitative model of information in each degree of freedom. Calculating the interdependence of far-field observables on scattering parameters lets us quantify the (Fisher) information a given observable carries about each such certain parameter [1, 2]. It would be highly interesting to investigate how different far-field channels compare in terms of their information content with regard to nanoscopic parameters of the optical system. Such an approach might be used to engineer optimised variants of measurement schemes, for instance of the polarisation-multiplexed readout we have discussed. For instance, it might find that certain polarisation combinations are more informative than others, or that certain combinations of wavevectors directly measure some particular parameter.

One way to still apply continuous information theory whilst avoiding setting up a full analytic model of a scattering system, would be to interpolate (and possibly extrapolate) calibration data. We have seen that in many cases, our principal component analyses find simple dependence of radiation patterns on the parameters of interest, with the dominant components often linear relations. We can invert this process by considering a few (orthogonal) simple functional forms and calculating which have appreciable overlap with the parameter dependence in the calibration data. For suitable problems and functional forms, the radiation pattern corresponding to this functional form will then represent this continuous degree of freedom. Further investigation could resolve how well such interpolation would work for a range of problems, but also how few calibration points are necessary for a given structure. We expect this would relate to the number of degrees of

freedom in the scattering problem, in much the same way we saw a limited number of singular values play a significant role in our principal component analysis. One challenge would then be to cleverly sample the parameter space to calibrate well with the minimum number of data points.

We have seen that in the parameter retrieval problem of chapter 7, polarisation information is more valuable than longer integration of wavevector information, showing better performance at equal total photon budget. It is hard to imagine that this result would be an artefact of our parameter retrieval technique and so we expect that it will generalise to a wide range of problem settings. The advantage of polarisation multiplexing is extra encouraging for the fact that it is so simple to implement: projecting the two output ports of a polarising beam splitter onto two camera sensors (or different regions of one) produces higher-precision parameter retrieval. A four-fold speed-up in integration time is highly significant in applications and it is worth investigating to what degree this insight generalises to other metrology techniques that do not normally use polarisation information.

The polarisation multiplexing strategy is a specific realisation of a more general idea. Different far-field channels encode information differently and combining different degrees of freedom may may make parameter retrieval more efficient. We have mentioned the information theoretical perspective on this, where variability in some observable encodes variability in some underlying parameter. A more directly physics-based question is which physical degrees of freedom are most likely to complement one another in terms of information encoded. Apart from polarisation and wavevector, we may for instance consider real-space and (frequency) spectral information. Wavevector and real-space information are closely related, specifically through the phase profile of the observed wavefront. Whether this helps or harms the synergy between their information flows remains to be seen. Interferometry could directly provide the additional information from insight into the phase profile. Wavelength multiplexing is another possibility. With the relatively broad resonances of plasmonic particles, varying wavelength over a narrow range is approximately equivalent to scaling up or down the scattering structure. Over larger wavelength ranges (many tens of nanometres), distinct resonances may be exploited. This looks like a promising avenue of exploration, especially where resonances are particularly sensitive to some quantity of interest.

This brings us back to a question from chapter 1: what is a good transducer? In chapter 5, we showed that a fairly simple transducer, a regular 4×4 array of dipole scatterers, can nonetheless be used to produce intricate near-field patterns by tailoring its far-field illumination channels. We saw that these field patterns might then be used for efficient, spatially resolved scatterometry. This is an encouraging result, but does not mean the transducer is optimal. For practical applications, we not only want efficiency to be as high as possible, but we are also interested in robustness to imperfections in fabrication and experimental alignment. There is no obvious rational design strategy for engineering the optimal transducer to measure a given parameter. One might start from a few (intuitive or random) designs and considering the dependence of parameter retrieval performance on the transducer design parameters. This approach would permit use of all the same techniques we have mentioned in the context of optimising readout of a given far-field radiation pattern. Ideally we would, in fact, design the transducer in conjunction with the measurement strategy, optimising far-field sensitivity to the parameters of interest.

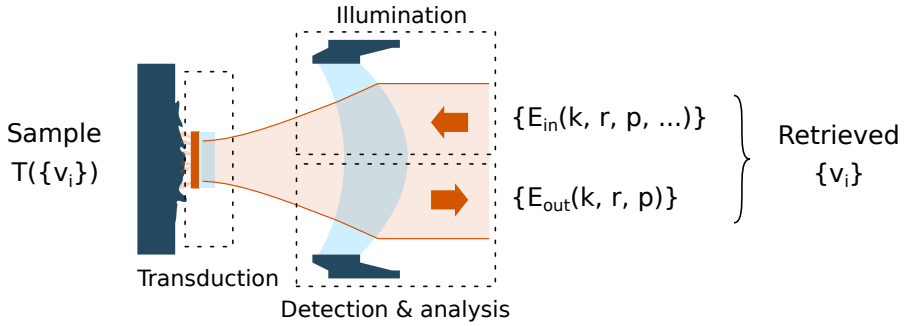

Figure 8.1: The inverse problem of parameter retrieval from far-field data. Three parts of the measurement apparatus can be optimised together: illumination, transduction, and detection.

In this way, we can define a challenging inverse design problem, with three separate components, as sketched in figure 8.1: the illumination parameters, the transducer, and the analysis scheme. For a given many-dimensional sample input-output relation, depending on various parameters of interest, we wish to retrieve these parameter values. Feasible approaches to this design challenge include any of the analytical techniques of inverse problem solving [3–5] as well as machine learning techniques [6, 7].

One extreme case of parameter retrieval is imaging: retrieving the full refractive index distribution of the top layer of a sample, in our case at nanoscale resolution. This is a major step ahead from the experimental demonstrations in this thesis, which have focussed on retrieval of typically two parameters (X and Y displacement). Though the problem can be expressed in the same terms, the large difference in complexity means our calibration-based technique cannot be applied in its current form. As currently defined, calibration data are taken for every possible combination of parameter values, which is evidently infeasible for a problem with many independent refractive index values at different positions. We may still be able to perform calibration by assuming that different sites are independently transduced to the far-field. In effect, this assumes that multiple scattering within the sample plays a minor role in radiation patterns and disregards far-field interference between the fields of coherently driven sites. To what degree these approximations are valid will depend on sample structures and material properties. The sensing study in chapter 5 shows that if we are able to switch hot-spots at specific positions on and off, we can selectively sense scatterers at the corresponding position. Using exposure patterns with a combination of spots also provides a basis for compressed sensing of complex patterns [8–10]. In such techniques, prior information about the sample, like a known distribution or number of scattering sites, is exploited to retrieve full-resolution sample data with fewer samples than would ordinarily be required (in imaging, less than one measurement per pixel). As such, compressed sensing could serve as a way to permit high-resolution parameter retrieval or even imaging at reasonable measurement time.

We started this thesis with a very applied perspective, envisioning a microscopy technique suitable for nanoscopic sensing and metrology. For that reason, it makes sense to evaluate the results in the context of technology readiness [11]. Likely the most directly applicable result in this thesis is the insight that polarisation-multiplexed readout may

improve parameter retrieval at negligible experimental cost. This idea may be implemented in demonstrations of existing (non-polarising) metrology tools to test whether it also provides a benefit in those contexts. The broader idea of microscopy through transduction of near- to far-field information by a metasurface is a step further from applications. As discussed, we have so far only tested retrieval of a few parameters at the same time. Going beyond this would require an exploration of the calibration scheme and whether sample sites can be treated as independent scatterers, as well as possible experimental improvements to permit variation of more parameters in real time. Experimental demonstration of near-field programming by far-field optimisation requires some way to verify the generated patterns. This may be done through established near-field microscopy techniques (chapter 1) or perhaps through clever use of fluorescent markers. The envisioned implementation of a metasurface scanning head, in the near-field of a sample, is also a significant technical challenge. Positioning a spatially extended structure with respect to a flat substrate is an active topic of research [12]. Rapid scanning and careful distance control, because transduction is bound to be distance dependent, are the next challenges in the mechatronics puzzle posed by our technique. Integration of all these elements will work towards the development of metasurface-assisted near- to far-field transduction into a fast, efficient technique for near-field sample inspection.

REFERENCES

1. Monier, E. & Chardon, G. “Cramér-Rao bounds for the localization of anisotropic sources”. in *ICASSP 2017* (2017), 3281–3285.
2. Colburn, S. & Majumdar, A. “Metasurface generation of paired accelerating and rotating optical beams for passive ranging and scene reconstruction”. *ACS Photonics* **7,** 1529–1536 (2020).
3. Haeberlé, O., Belkebir, K., Giovaninni, H. & Sentenac, A. “Tomographic diffractive microscopy: basics, techniques and perspectives”. *J. Mod. Opt.* **57,** 686–699 (2010).
4. Lin, Z., Roques-Carmes, C., Pestourie, R., Soljačić, M., Majumdar, A. & Johnson, S. G. “End-to-end nanophotonic inverse design for imaging and polarimetry”. *Nanophotonics* **10,** 1177–1187 (2020).
5. Bouchet, D., Seifert, J. & Mosk, A. P. “Optimizing illumination for precise multiparameter estimations in coherent diffractive imaging”. *Opt. Lett.* **46,** 254 (2021).
6. McCann, M. T., Jin, K. H. & Unser, M. “Convolutional neural networks for inverse problems in imaging: A review”. *IEEE Signal Process. Mag.* **34,** 85–95 (2017).
7. Lucas, A., Iliadis, M., Molina, R. & Katsaggelos, A. K. “Using deep neural networks for inverse problems in imaging: Beyond analytical methods”. *IEEE Signal Process. Mag.* **35,** 20–36 (2018).
8. Candès, E. J., Romberg, J. K. & Tao, T. “Stable signal recovery from incomplete and inaccurate measurements”. *Commun. Pure Appl. Math.* **59,** 1207–1223 (2006).
9. Cambareri, V., Rovatti, R. & Setti, G. “Maximum entropy hadamard sensing of sparse and localized signals”. in *2014 IEEE International Conference on Acoustics, Speech and Signal Processing (ICASSP)* (2014), 2357–2361.

10. Massa, A., Rocca, P. & Oliveri, G. “Compressive sensing in electromagnetics - a review”. *IEEE Antennas Propag. Mag.* **57,** 224–238 (2015).

11. Héder, M. “From NASA to EU: the evolution of the TRL scale in Public Sector Innovation”. *Innovation J.* **22,** 3 (2017).

12. Ernst, S., Irber, D. M., Waeber, A. M., Braunbeck, G. & Reinhard, F. “A planar scanning probe microscope”. *ACS Photonics* **6,** 327–331 (2019).

NANO-OPTICAL SENSING AND METROLOGY THROUGH NEAR- TO FAR-FIELD TRANSDUCTION

SUMMARY

Imaging of nanoscale structures with visible light is hindered by the diffraction limit, which prevents free-space focussing of light into dimensions smaller than a large fraction of its wavelength. Various superresolution techniques exist to circumvent these problems, each with their own drawbacks. In particular, high-resolution imaging of unlabelled samples is a tricky and slow process. In this thesis, we envision a sensing technique exploiting a metasurface patch introduced into the near-field of a sample. Near-field interactions then transduce nanoscopic spatial information into the far-field. We explore the capabilities and limitations of such a technique in terms of sensing and metrology performance.

Super-resolution imaging is often viewed in terms of engineering narrow point spread functions, but nanoscale optical metrology can be performed without real-space imaging altogether. We investigate how partial knowledge of scattering nanostructures enables extraction of nanoscale spatial information from far-field radiation patterns. We use principal component analysis to find patterns in calibration data and use these patterns to retrieve the position of a point source of light. In an experimental realisation using angle-resolved cathodoluminescence, we retrieve the light source position with an average error below $\lambda/200$. The patterns found by principal component analysis reflect the underlying scattering physics and reveal the role the scattering nanostructure plays in localisation success. The technique described here is highly general and can be applied to gain insight into and perform subdiffractive parameter retrieval in various applications.

Extending these results from light sources to scattering objects, we study how nano-photonic structures can be used to determine the position of a nearby nanoscale object with subwavelength accuracy. By perturbing the near-field environment of a metasurface transducer consisting of nano-apertures in a metallic film, the location of the nanoscale object is encoded into a far-field optical response. Monitoring this scattering pattern and comparing it to measured reference data, we demonstrate localisation of the object accurate to 24 nm across an area of $2 \times 2\ \mu m^2$. We find that adding complexity to the nano-photonic transducer allows localisation over a larger area while maintaining resolution,

as it enables encoding more information on the position of the object in the transducer far-field response.

More complex transducers enable another strategy: to use incident degrees of freedom to control near-field structure. We study how a single near-field metasurface patch may be used to create a wide variety of sample plane intensity patterns by applying different illumination profiles. Numerical analysis shows that one metasurface patch may be used to generate complete bases of intensity patterns on a grid as fine as $\lambda/16$. We explore the limits of control in terms of the number of modes on the illumination side and spatial resolution on the sample side. We then show how the engineered fields may be used for particle detection, showing the potential the approach holds for nanoscale optical sensing.

Nanophotonic scattering systems encoding nanoscopic information in their radiation patterns may be used for metrology. We demonstrate this with overlay targets consisting of just four nanoparticles, of which we fabricate many copies with a range of synthetic overlay errors. We successfully measure these overlay errors by the calibration-based technique used before. Additionally, using calibration on separate targets, we show that an independent model is effective, despite the small size of the targets.

Finally, we study how combining measurement under different polarisation conditions may be used to improve parameter retrieval performance. Specifically, we consider how precisely we can measure overlay with a given photon budget, distributed across different illumination or detection channels. Our results show that polarisation multiplexing retrieves overlay much more accurately than single-polarisation or unpolarised measurement. Confirming our theoretical analysis, we observe that multiplexing either incident or analysed polarisation produces an improvement in precision equivalent to 7 dB in signal level.

The results in this thesis suggest several interesting directions for information retrieval research and for sensors development. Sensors may be able to benefit from polarisation multiplexing or near-field programming. Quantitative analysis of the information content of different degrees of freedom may enable optimal sensing strategies. Pending technical implementation, metasurface-assisted near- to far-field transduction may prove a powerful technique for nano-optical sample inspection.

NANO-OPTISCHE DETECTIE EN METROLOGIE MIDDELS TRANSDUCTIE VAN HET NABIJE NAAR HET VERRE VELD

SAMENVATTING

Structuren op de nanoschaal laten zich niet zonder meer afbeelden met zichtbaar licht. Dat komt door de diffractielimiet, die zorgt dat licht niet fijner gefocusseerd kan worden dan tot een volume met een diameter bijna zo groot als de golflengte van het licht. Er zijn superresolutie-technieken die om de diffractielimiet heen werken, maar al die technieken hebben ook nadelen. In het bijzonder gaat het fijn afbeelden van pigment-vrije structuren alleen moeizaam en traag. In dit proefschrift beschouwen wij een meetmethode gebaseerd op een meta-oppervlak, een oppervlak met verstrooiende structuren fijner dan de schaal van de golflengte van licht, dat dicht bij een monster wordt gebracht. Interacties in het nabije veld verstrooien nanoscopische ruimtelijke informatie over het monster dan naar het verre veld. We zoeken uit wat de sterktes en zwaktes van zo een techniek zijn, in termen van meetnauwkeurigheid.

Superresolutie-technieken worden soms gezien als een kwestie van fijne punt-overdrachtsfuncties, maar het is mogelijk om superresolutie-informatie te verkrijgen geheel zonder reële afbeeldingen. Wij onderzoeken hoe gedeeltelijke kennis van verstrooiende nanostructuren het mogelijk maakt nanoscopische informatie af te leiden uit stralingspatronen. We maken gebruik van hoofdcomponentenanalyse om patronen in kalibratiedata te vinden en we gebruiken die patronen om de positie van een lichtbron te achterhalen. In een experiment gebruikmakend van cathode-luminescentie vinden we de positie van een lichtbron met een gemiddelde fout kleiner dan $\lambda/200$. De gevonden patronen geven inzicht in de onderliggende verstrooiingsfysica en laten zien hoe de nanostructuur bijdraagt aan het succes van de methode. De beschreven methode is breed toepasbaar en kan in allerlei toepassingen helpen bij het uitlezen van sub-diffractieve parameterwaarden.

Na lichtbronnen passen we deze methode toe op verstrooiende objecten, door te onderzoeken hoe nanofotonische structuren kunnen worden gebruikt om de positie van

een dichtbij geplaatst object met sub-diffractieve precisie te achterhalen. Als het nabije veld van een meta-oppervlak, bestaand uit nanoscopische gaatjes in een metaallaag, wordt verstoord, wordt de positie van de verstoring gecodeerd in het optisch verre veld. Door dit stralingspatroon op te nemen en te vergelijken met kalibratiedata, achterhalen we de positie van de verstoring met een precisie van 24 nm in een domein van $2 \times 2\ \mu m^2$. Extra complexiteit in het meta-oppervlak blijkt het mogelijk te maken dezelfde precisie te halen over een groter oppervlak, door meer informatie in het verre veld van het meta-oppervlak te coderen.

Complexere meta-oppervlakken staan ons ook toe vrijheidsgraden in de inkomende bundel te gebruiken om de nabije veld-structuur te manipuleren. We bestuderen hoe een vast, eindig meta-oppervlak kan worden gebruikt om allerlei verschillende patronen in het nabije veld te produceren, door enkel de belichting uit het verre veld aan te passen. Berekeningen tonen aan dat één meta-oppervlak complete bases van intensiteitspatronen in het nabije veld kan genereren, op roosters zo fijn als $\lambda/16$. We verkennen de grenzen van deze controle als functie van het aantal beschikbare vrijheidsgraden in de belichting en de ruimtelijke resolutie op het monster. Ook laten we zien hoe de ontworpen velden kunnen worden gebruikt om deeltjes te detecteren. Dit onderschrijft de potentie de methode heeft voor nano-optische inspectie.

Nanoscopische informatie verwerkt in de stralingpatronen van nano-fotonische verstrooiende systemen kan ook worden gebruikt voor metrologie. We laten dit zien met uitlijningsverificatiestructuren bestaand uit slechts vier nanodeeltjes. We maken een groot aantal exemplaren van zulke structuren, met bewust gekozen uitlijnfouten. Deze uitlijnfouten lezen we uit met dezelfde methode op basis van kalibratie die we eerder hebben gebruikt. Met kalibratie op andere structuren laten we ook zien dat een onafhankelijk model de uitlijnfouten af kan lezen, ondanks de kleine schaal van de structuren.

Tot slot bestuderen we hoe parameters nauwkeuriger kunnen worden afgelezen door verschillende polarisatiekanalen te combineren. We kijken hoe nauwkeurig we uitlijnfout kunnen meten met een vast fotonbudget, al dan niet verdeeld over verschillende polarisatiekanalen in belichting of detectie. Onze resultaten laten zien dat polarisatiereconfiguratie veel preciezere metingen van uitlijnfout oplevert dan meten met één enkele polarisatie of met ongepolariseerd licht. De metingen bevestigen onze theoretische voorspellingen en laten een prestatieverbetering zien die overeenkomt met 7 dB in signaalsterkte.

De in dit proefschrift beschreven resultaten werpen verschillende interessante richtingen op voor onderzoek naar reconstructie van informatie uit metingen en ontwikkeling van sensoren. Sensoren kunnen baat hebben bij polarisatie-reconfiguratie en ontworpen nabije velden. Gekwantificeerde analyse van de informatie in verschillende vrijheidsgraden kan helpen detectie-strategieën te optimaliseren. Als de methode technisch is geïmplementeerd, verwachten wij dat transductie van het nabije naar het verre veld middels een meta-oppervlak een krachtige techniek voor nano-optische inspectie kan worden.

ACKNOWLEDGEMENTS

Science in the modern world is a highly collaborative affair. This is reflected in this thesis, which is the result of a fruitful collaboration between a range of organisations, research groups and people. On these pages, I hope to express my thanks for the many contributions, in many forms, made to this thesis over these four years.

Ewold, as my promotor and group leader, I thank you for mentoring me and for always being available for discussion and advice, in spite of your many other obligations. Your deep understanding of both the technical and process sides of research has been inspirational. I am also grateful for the freedom you gave me to plan and organise my own work, which made the more arduous parts of the project much more bearable. Femius, as my co-promotor, I thank you for your tremendous creativity in turning our ideas into experiments and papers. The ease with which you speak about advanced optical techniques shows an expertise I can only hope to emulate. At my interview with you, we never got around to the presentation I had prepared, and you have continued to surprise me ever since. Giampiero, as my second promotor, I thank you for providing your fresh perspective on our plans and papers. The interactions with your group in Delft enriched the project with an innovative, applications-oriented focus.

Tom, your arrival marked the transition from a largely solitary project to a much more rewarding team effort. Our collaboration has both been very smooth and quite productive, thanks to your many talents and your ability to combine a strong drive with a very kind and patient nature. It has been an absolute pleasure to work with you. Daniël, your taking up of the shear force experiments allowed us to give a very interesting research line the attention it deserved. To do so, you had to quickly master an extremely complex and opaque measurement set-up, which you have done admirably. With your creativity and curiosity, I think you will continue to make a tremendous difference to many projects at AMOLF.

From the start, a number of external partners have supported this project with their thoughts and ideas through our user committee. I thank Jason Osborne (Bruker), Wim Coene (ASML), Rogier Verberk (TNO), Arthur van de Nes (VSL) and Richard Koops (VSL) for their enthusiasm and encouragement. I thank another external partner, Thomas Bauer (TU Delft), for help fabricating shear force probes and advice on how to use them. During the visits to Delft, Pjotr Stoevelaar (TNO) and Arvind Nagarajan (TNO) contributed to valuable discussions on fabrication and modelling.

AMOLF has the exceptional benefit of an extensive and highly skilled network of tech-

nical support staff. This makes the institute a uniquely efficient and painless place to set up a complicated new experiment. For enabling both the initial realisation and the many upgrades implemented later, I am grateful to Henk-Jan Boluijt, Marco Seynen, Ronald Buijs, Idsart Attema, Pepijn Huider, Hinco Schoenmaker and the workshop team led by Jan van der Linden. Our nanolab team, Hans Zeijlemaker, Dimitry Lamers, Bob Drent, Andries Lof and Igor Hoogsteder, have been vital both to our scientific results and the excellent atmosphere at the institute. Thanks also to the various other support departments, allowing the science to run as smoothly as possible. We named the set-up Midas, hoping that some of what the shear-force probe touched would turn to gold. I like to believe that it did.

During my stay at AMOLF, I have had the pleasure to work with two generations of Ewold's Photonic Forces. The list has grown impressively long: Rick, Freek, Juha, John, Nikhil, Giada, Jan Bonne, Roel, Jesse, Jente, Javier, René, Johneph, Pascal, Cesare, Daniël, Amy, Hessel, Omar, Pierre, Alejandro and Laura. I have empathised with your struggles and now applaud your successes in optomechanics, topology and nanofabrication. Your input on my project has been invaluable and I can only hope my many questions were of some use to yours. Thanks also for your camaraderie in the laboratory, for the good discussions over lunch, and for the fun group activities. I have particularly enjoyed our contributions to the AMOLF Open Days, captivating audiences with everything from trapped laser beams to music captured in open flame.

The Magic of AMOLF is its people and I have had too many wonderful interactions to list. I have met some great people at the nanophotonics colloquia, staff association events or simply at the coffee table. Nasim, Susan, and Lucie, I credit our co-working days with the preservation of my sanity throughout the writing of this thesis. Kelly, I much enjoyed exchanging bird stories with you. Isabelle, your wit and humour never failed to brighten my day. Bela, Jorijn, Joleen, Ramon, and Jesse, the Python workshops were a fun way to put a shared hobby to good use. Agustín, Andrea, Annemarie, Giorgio, Hugo, Jenny, Julia, Kevin, Lukas, Magda, Mareike, Mark, Marko, Marco, Nick, Ruslan, Verena, and so many others: to all the kind, charming, incredibly talented people I have met at AMOLF, many thanks for the great times.

This thesis would not have been possible without the support of a great many people outside of work. Nikki and Roel, thanks for being my paranymphs. I am proud to have such people as yourselves behind me on the day of my defence. Lieke, thanks for being my closest friend despite the distance. I look forward to many more adventures with you, James, and Nell. Alex, thanks for letting me be part of some beautiful moments in your life with Dennis and Freya. Lucy, Milinda, Lieke, Anna, (& Nikki, Roel, Alex, Dennis), I am always delighted to see you all and I cannot wait until we can have our game nights and birthday parties in person again. Anouschka, your boundless enthusiasm always brings a smile to my face. Christa, Sven, Wiekie, I always love your stories, keep them coming. Stijn, Pim, Nicky, Jeroen, Walter, thank you for the distractions of a world's worth of bad puns.

Finally, I thank my family for all the warmth and love. To my parents: thank you for your kindness and support as I charted out my path. Construction on your new home nicely coincided with a time I was very happy to take up mindless labour. Jasper, Lennard, you too have taken big steps over these past years. I look forward to seeing where your journeys take you. I am also very happy to share the completion of this thesis with my dear grandparents. Thank you to all those who have been close to me for all this time.

About the author

Robin Buijs was born in 1991 in Nijmegen, The Netherlands. He studied Applied Physics at the University of Twente, obtaining his Bachelor of Science degree in 2012 with a thesis on non-linear optics, which was awarded the Bachelor Thesis prize of the Dutch Physics Association (NNV). He continued to study both Applied Physics and Electrical Engineering, obtaining Master of Science degrees in each from the University of Twente in 2015. During his Master's, he spent three months working on DNA origami at the University of Kyoto and a year developing a light field sensor based on structured surfaces at the MESA+ Institute for Nanotechnology. Besides, he was a very active member of the student community, organising a range of events and chairing the student delegation in the University Council for a year.

After graduation, Robin worked on information processing in superconducting circuits at ETH Zurich for fifteen months. Subsequently, he joined the Photonic Forces group at AMOLF for a project on nano-optical sensing, the results of which are described in this thesis. Robin was involved in the AMOLF Python team, organising three sessions of the annual Python course for the research community, and was also involved in a number of outreach activities.

Robin enjoys wildlife photography, hiking and board games.

LIST OF PUBLICATIONS

PUBLICATIONS RELATING TO THIS THESIS

1. Buijs, R. D., Schilder, N. J., Wolterink, T. A. W., Gerini, G., Verhagen, E. & Koenderink, A. F. "Super-resolution without imaging: Library-based approaches using near-to-far-field transduction by a nanophotonic structure". *ACS Photonics* **7,** 3246–3256 (2020).
2. Wolterink, T. A. W., Buijs, R. D., Gerini, G., Koenderink, A. F. & Verhagen, E. "Localizing nanoscale objects using nanophotonic near-field transducers". *Nanophotonics* **10,** 1723–1732 (2021).
3. Buijs, R. D., Wolterink, T. A., Gerini, G., Verhagen, E. & Koenderink, A. F. "Programming Metasurface Near-Fields for Nano-Optical Sensing". *Adv. Opt. Mater.* 2100435 (2021).
4. Wolterink, T. A., Buijs, R. D., Gerini, G., Verhagen, E. & Koenderink, A. F. "Calibration-based overlay sensing with minimal-footprint targets". *Submitted* (2021).
5. Buijs, R. D., Wolterink, T. A., Gerini, G., Koenderink, A. F. & Verhagen, E. "Information advantage from polarization-multiplexed readout of nanophotonic scattering sensors". *In preparation* (2021).

OTHER PUBLICATIONS

6. Yüce, E., Ctistis, G., Claudon, J., Dupuy, E., Buijs, R. D., de Ronde, B., Mosk, A. P., Gérard, J.-M. & Vos, W. L. "All-optical switching of a microcavity repeated at terahertz rates". *Opt. Lett.* **38,** 374 (2013).
7. Woldering, L. A., Buijs, R. D., Krijnen, G. J. M. & Vos, W. L. *Directionally Sensitive Pixel Array for Optical Cameras* U.S. Provisional Patent US62/093494 (2014).
8. Gasparinetti, S., Besse, J.-C., Pechal, M., Buijs, R. D., Eichler, C., Carmichael, H. J. & Wallraff, A. "Two-photon resonance fluorescence of a ladder-type atomic system". *Phys. Rev. A* **100,** 033802 (2019).
9. Wobben, M. D., Valenti, M., Bleiji, Y., Cordaro, A., Tabernig, S., Aarts, M., Buijs, R. D., Rodriguez, S. R.-K., Polman, A. & Alarcón Lladó, E. "Plasmonic indium lattices fabricated via electrochemical deposition". *in preparation* (2021).